



Kent Academic Repository

Cobourne, Glyn David (2017) *The Atomistic Structure of Amorphous Carbonate, Phosphate and Sulfate Biominerals*. Doctor of Philosophy (PhD) thesis, University of Kent,.

Downloaded from

<https://kar.kent.ac.uk/75161/> The University of Kent's Academic Repository KAR

The version of record is available from

This document version

UNSPECIFIED

DOI for this version

Licence for this version

UNSPECIFIED

Additional information

Versions of research works

Versions of Record

If this version is the version of record, it is the same as the published version available on the publisher's web site. Cite as the published version.

Author Accepted Manuscripts

If this document is identified as the Author Accepted Manuscript it is the version after peer review but before type setting, copy editing or publisher branding. Cite as Surname, Initial. (Year) 'Title of article'. To be published in *Title of Journal*, Volume and issue numbers [peer-reviewed accepted version]. Available at: DOI or URL (Accessed: date).

Enquiries

If you have questions about this document contact ResearchSupport@kent.ac.uk. Please include the URL of the record in KAR. If you believe that your, or a third party's rights have been compromised through this document please see our [Take Down policy](https://www.kent.ac.uk/guides/kar-the-kent-academic-repository#policies) (available from <https://www.kent.ac.uk/guides/kar-the-kent-academic-repository#policies>).

**The Atomistic Structure of
Amorphous Carbonate, Phosphate and Sulfate Biominerals**

Thesis prepared for the degree of
Doctor of Philosophy

by
Glyn David Cobourne

School of Physical Sciences
University of Kent
Canterbury
UK

Abstract

Biominerals are key to all life, whether they make up exoskeletons of marine organisms (amorphous calcium carbonate), human bones (amorphous calcium phosphate) or being signs of extra-terrestrial life (amorphous iron sulfate) but little is known of their atomistic structures. How they behave could be determined by this structure and knowledge of this could lead to favouring certain crystallisation pathways or indeed speeding up the process, ie. If someone breaks their arm, can we induce faster healing?

In the present study, amorphous biominerals including carbonates, phosphates and sulfates are synthesised (stabilised where necessary). The proton content is reduced either via heat-treatment or deuteration. The deuteration method is the first of its kind and enabled the materials of study to be examined at central facilities via x-ray and neutron diffraction.

For the first time, neutron diffraction experiments have been conducted on amorphous calcium and magnesium carbonates. Also, a first synthesis of deuterated amorphous biominerals including amorphous calcium carbonate (ACC), amorphous magnesium carbonate (AMC) and amorphous calcium phosphate (ACP).

Diffraction data from these materials are utilised by the empirical potential structure refinement (EPSR) algorithm to generate atomistic models using Reverse Monte Carlo (RMC). These models used well defined molecular units and yielded results showing the calcium distribution throughout ACC to be uniformed, contrary to former reports on the atomistic structure of ACC.

i. Contents

1.	Introduction	6
1.1	<i>Amorphous vs. Crystalline</i>	6
1.2	<i>Biominerals and Biomineralisation</i>	6
1.3.1	Amorphous Carbonates	7
1.3.1.1	Amorphous Calcium Carbonate	7
1.3.1.2	Magnesium Stabilised Amorphous Calcium Carbonate	10
1.3.1.3	Amorphous Magnesium Carbonate	11
1.3.2	Amorphous Phosphates	14
1.3.2.1	Amorphous Calcium Phosphate	14
1.3.2.2	Amorphous Iron Phosphate	17
1.3.3	Amorphous Sulfates	20
1.3.3.1	Amorphous Calcium Sulfate	20
1.3.3.2	Amorphous Iron Sulfate	22
1.4	Project Aims	23
2.	Theoretical Background	24
2.1	<i>Diffraction of non-crystalline solids</i>	24
2.1.1	Pair Correlation Function	24
2.1.1.1	Crystalline Materials	24
2.1.1.2	Non-crystalline Materials	24
2.1.1.3	Extraction of Structural Information	25
2.1.2	Theory of Diffraction	25
2.1.2.1	Concept of Wave-Particle Duality	25
2.1.2.2	General Scattering Theory in Crystals	25
2.1.2.3	General Scattering Theory in Amorphous Materials	26
2.1.2.4	Scattering from A Single Atom	27
2.1.2.5	Scattering from Multiple Atoms	27
2.1.2.6	Scattering Length for Neutron Scattering	30
2.1.2.7	Form Factor for X-ray Scattering	30
2.1.2.8	Total Scattering Cross Section	30
2.1.2.9	Differential Cross Section	31
2.1.2.10	Total Structure Factor	31
2.1.2.11	Weighting Factors	32
2.1.2.12	Structure Factor	33
2.1.3	Diffraction Experiments	33
2.1.3.1	Diffraction Measurement	33
2.1.3.2	Neutron Diffraction Experiment	34
2.1.3.3	Synchrotron X-ray Diffraction Experiment	34
2.1.3.4	Normalisation and Background Correction	35
2.1.3.5	Incoherent Compton Scattering	35
2.1.3.6	Attenuation Correction (Neutron)	35
2.1.3.7	Static Approximation of Differential Cross Sections (Placzek Correction)	35
2.2	<i>Computational Modelling</i>	36
2.2.1	Interatomic Potentials	36
2.2.2	Monte Carlo Modelling	36
2.2.3	Empirical Potential Structure Refinement (EPSR)	37
3.	Methods	39
3.1	<i>Experimental Methods</i>	39
3.1.1	Synthesis	39
3.1.2	Laboratory-based Characterisation	40
3.1.2.1	X-ray Diffraction (XRD)	40
3.1.2.2	TGA-DSC	42

2.1.2.3	Helium Micropycnometry	43
2.1.2.4	FTIR	44
2.1.2.5	X-ray Fluorescence (XRF)	46
2.1.3	Central Facilities Experiments	48
2.1.3.1	X-ray Diffraction (XRD)	48
2.1.3.2	EXAFS	49
2.1.3.3	Neutron Scattering	51
2.2	<i>Computational Methods</i>	54
2.2.1	GHEMICAL	54
2.2.2	GUDRUN	55
2.2.3	Empirical Potential Structure Refinement (EPSR) Modelling	56
3.	Results & Discussion	59
3.1	<i>Amorphous Calcium Carbonate</i>	59
3.1.1	Synthesis	59
3.1.2	Laboratory-based Characterisation	60
3.1.2.1	Laboratory XRD	60
3.1.2.2	Thermo-Gravimetric Analysis (TGA)	62
3.1.2.3	Helium Micropycnometry	62
3.1.2.4	FTIR	63
3.1.3	Central Facility Experiments	65
3.1.3.1	Synchrotron XRD	65
3.1.3.2	EXAFS	66
3.1.3.3	Neutron Scattering	67
3.1.4	Empirical Potential Structure Refinement (EPSR) Modelling	70
3.2	<i>Magnesium Stabilised Amorphous Calcium Carbonate</i>	75
3.2.1	Synthesis	75
3.2.2	Laboratory-based Characterisation	75
3.2.2.1	Laboratory XRD	75
3.2.2.2	Thermo-Gravimetric Analysis (TGA)	78
3.2.2.3	Helium Micropycnometry	80
3.2.2.4	X-ray Fluorescence (XRF)	81
3.2.3	Central Facility Experiments	81
3.2.3.1	Synchrotron XRD	81
3.2.3.2	EXAFS	82
3.2.3.3	Neutron Scattering	83
3.2.4	Empirical Potential Structure Refinement (EPSR) Modelling	84
3.3	<i>Amorphous Magnesium Carbonate</i>	90
3.3.1	Synthesis	90
3.3.2	Laboratory-based Characterisation	90
3.3.2.1	Laboratory XRD	90
3.3.2.2	Thermo-Gravimetric Analysis (TGA)	91
3.3.2.3	Helium Micropycnometry	93
3.3.3	Central Facility Experiments	94
3.3.3.1	Synchrotron XRD	94
3.3.3.2	Neutron Scattering	95
3.3.4	Empirical Potential Structure Refinement (EPSR) Modelling	96
3.4	<i>Amorphous Phosphates</i>	103
3.4.1	Amorphous Calcium Phosphate	103
3.4.1.1	Synthesis	103
3.4.1.2	Laboratory-based Characterisation	103
3.4.1.2.1	Laboratory XRD	103
3.4.1.2.2	Helium Micropycnometry	103
3.4.1.3	Central Facility Experiments	104

3.4.1.3.1	Neutron Scattering	104
3.4.1.4	Empirical Potential Structure Refinement (EPSR) Modelling	105
3.4.2	Amorphous Iron Phosphate	108
3.4.2.1	Building the EPSR Model	108
3.4.2.2	Empirical Potential Structure Refinement (EPSR) Modelling	108
3.5	<i>Amorphous Sulfates</i>	110
3.5.1	Amorphous Calcium Sulfate	110
3.5.1.1	Synthesis	110
3.5.1.2	Laboratory-based Characterisation	110
3.5.1.2.1	Laboratory XRD	110
3.5.2	Amorphous Iron Sulfate	113
3.5.2.1	Synthesis	113
3.5.2.2	Laboratory-based Characterisation	113
3.5.2.2.1	Laboratory XRD	113
3.5.2.2.2	Thermo-Gravimetric Analysis (TGA)	115
3.5.2.2.3	Helium Micropycnometry	116
3.5.2.3	Central Facility Experiments	117
3.5.2.4	Empirical Potential Structure Refinement (EPSR) Modelling	117
4.	Conclusions	118
4.1	<i>Amorphous Calcium Carbonate</i>	118
4.2	<i>Magnesium Stabilised Amorphous Calcium Carbonate</i>	118
4.3	<i>Amorphous Magnesium Carbonate</i>	118
4.4	<i>Amorphous Phosphates</i>	118
4.5	<i>Amorphous Sulfates</i>	118
5.	Bibliography	119

The most exciting phrase to hear in science, the one that heralds new discoveries, is not 'Eureka!' but
'That's funny...'

- *Isaac Asimov*

ii. Acknowledgements

The author would like to give a huge thank you to Dr Gavin Mountjoy for his constant support and patience, particularly through the writing process. Juan Diego Rodriguez-Blanco for his enormous knowledge on biominerals and his selfless assistance both with sample preparation and central facility experiments. The instrument scientists, Alex Hannon and Jasper Plaisier at ISIS and Elettra whom guided me through a whole new world of exciting scientific experimentation.

A special thank you to my loving wife, Kez, whom kept me going through all the difficult times with her love, kind words and driving energy. Thank you to Kaleb for always asking me the questions I should be answering. My thanks and gratitude to my parents, Mike and Sheila who enabled me to pursue my chosen path with all their love and support.

1. Introduction

1.1 Amorphous vs. Crystalline

Materials and their structures are of, but not limited to, great social, economic and technological importance throughout our world (and sometimes beyond it) and hence the study of materials is fundamental in driving our civilisation forward. When we speak of materials science, there are usually two distinct fundamental classes of materials being studied; crystalline and amorphous materials (see Figure 1.1 below).

A crystalline material is defined as one which possesses a high degree of structural order in a solid. Crystals exhibit structural order in the short-range (typically first or second nearest neighbours) and medium-range as well as long-range. The long-range order in crystalline materials gives rise to the lattice periodicity or the arrangement of atoms in a repeating unit cell.

Whilst amorphous materials show short-range order and sometimes order in the medium-range, there is a lack of order in the long-range and hence no periodicity is observed in amorphous materials. The absence of long-range order in amorphous materials is due to the disordered arrangement of the atoms within the solid.

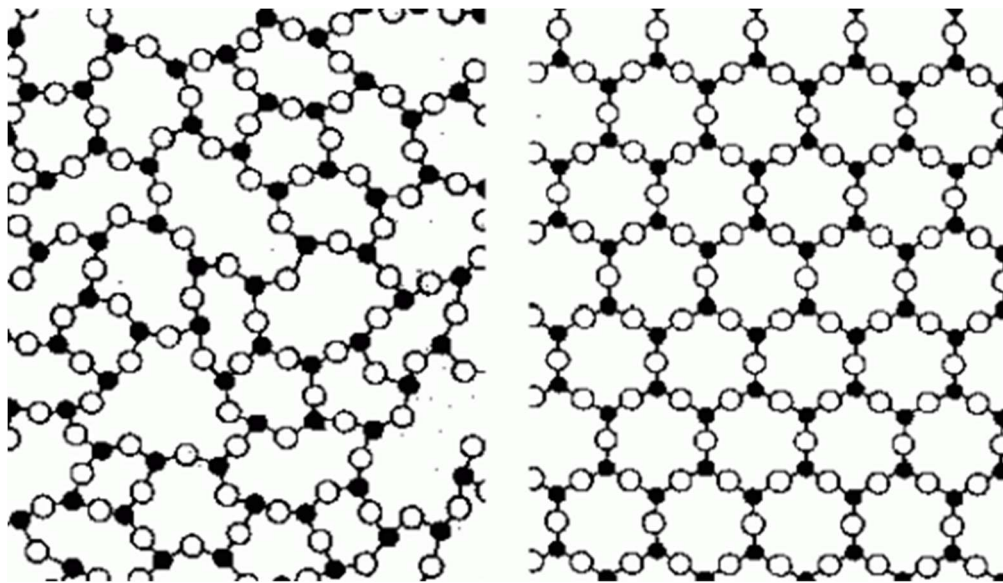


Figure 1.1^[1] – Amorphous material (left) displays short-range order by with black-white-black order of atoms but no definable medium-range or long-range order. The crystalline material (right), on the other hand, which exhibits medium-range and long-range order with the repeating, highly ordered system.

Many of us are familiar with many crystalline compounds such as calcite (chalk), hydroxyapatite (bone tissue) and gypsum (plaster of Paris), there exist less common, amorphous forms of such materials. The amorphous forms of these materials may exist as precursors to the more stable crystalline material, and biological organisms have utilised these amorphous materials for their own benefit.

1.2 Biominerals and Biomineralisation

As a necessity of life, organisms rely on minerals to provide structure (bone tissue), protection (exoskeletons) and nutrition (feeding). These minerals, referred to as biological minerals or simply biominerals undergo processes known as biomineralisation which involve mineral production within a

living organism. In general terms, raw materials are gathered by the organism from the environment and used to produce a mineral of benefit to the organism. Some organisms choose to produce biologically inactive forms of biominerals and then “activate” them when that material is needed. A classic example is tissue growth in the human body where we ingest nutrients and convert them to “inactive” bone or muscle storage tissue in the bone marrow and when we require more bone when we break an arm or need to build up muscle strength in our legs the human body “activates” the stored minerals and they are converted to bone or muscle. These processes despite being ubiquitous throughout the natural world are generally not well understood due to the transient nature of some biominerals or because the timescales on which the biomineralisation processes occur make observation difficult. Biominerals are most commonly iron and calcium carbonates^[2-4], phosphates^[3] with some silicates^[4] and sulfates^[5] being observed and studied.

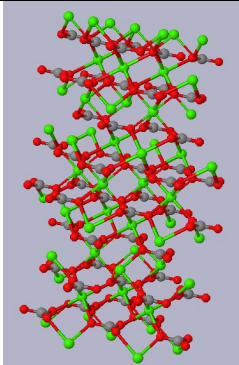
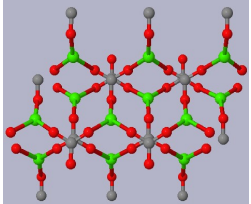
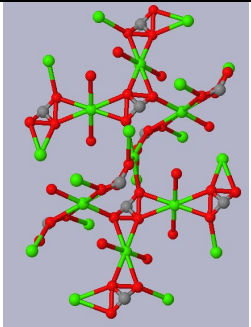
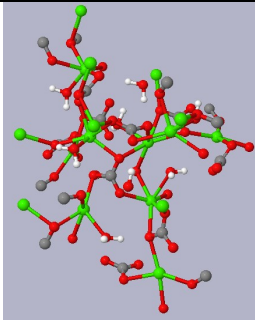
1.3.1 Amorphous Carbonates

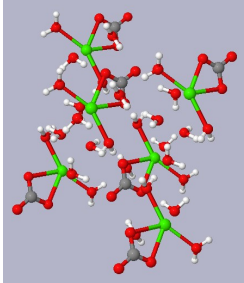
1.3.1.1 Amorphous Calcium Carbonate

Amorphous calcium carbonate (ACC) is believed to play a key role in biomineralisation processes within marine organisms, such as sea urchins, crustaceans and sea shells (bivalvia)^[6], which use the crystalline calcium carbonate(s) as structural building blocks. Most notably, ACC has been proposed to be a calcium storage medium which is then crystallised to form new structural elements of the organism^[6]. ACC may thus have an analogous role to the mammalian equivalent, amorphous calcium phosphate (ACP), which is involved in biomineralisation of crystalline calcium phosphates within human bones^[7].

Calcium carbonate exists in six different polymorphs found in nature, below is Table 1.1 detailing names, structures, composition, approximate density, space group and unit cell dimensions of the various polymorphs:

Table 1.1 – Polymorphs of calcium carbonate

Polymorph of Calcium carbonate	Crystal structure†	Composition	Density (g/cm ³)	Space Group	Unit Cell Dimensions (Å)
Calcite	 [8]	CaCO ₃ Calcium (green) Carbon (grey) Oxygen (red)	2.71 ^[9]	R3c ^[9] Trigonal - Hexagonal Scaleno-hedral	a=4.989 ^[9] c=17.062
Aragonite	 [10]	CaCO ₃ Calcium (grey) Carbon (green) Oxygen (red)	2.93 ^[11]	Pmcn ^[11] Orthorhombic - Dipyramidal	a=4.959 ^[11] b=7.968 c=5.741
Vaterite	 [12]	CaCO ₃ Calcium (green) Carbon (grey) Oxygen (red)	2.56 ^[11]	P6 ₃ /mmc ^[11] Dihexagonal Dipyramidal	a=4.130 ^[11] c=8.490
Monohydrocalcite	 [13]	CaCO ₃ .H ₂ O Calcium (green) Carbon (grey) Oxygen (red) Hydrogen (white)	2.38 ^[14]	P3 ₁ 2 ^[14] Trigonal - Trapezohedral	a=10.566 ^[14] c=7.573

Ikaite	 [15]	$\text{CaCO}_3 \cdot 6\text{H}_2\text{O}$ Calcium (green) Carbon (grey) Oxygen (red) Hydrogen (white)	1.77 ^[16]	$C 2/c^{[16]}$ Monoclinic	$a=8.87^{[16]}$ $b=8.23$ $c=11.02$
Anhydrous ACC	-	CaCO_3	-	?	?
Hydrated ACC	-	$\text{CaCO}_3 \cdot \text{H}_2\text{O}$	-	?	?

Greater understanding of biomineralisation processes should include detailed knowledge of the atomic structure of all calcium carbonate phases (which are currently well understood [8-16]), including ACC and the relation between ACC and the structures of crystalline calcium carbonate phases. The composition of ACC has been reported as being $\text{CaCO}_3 \cdot n\text{H}_2\text{O}$ where $n = 1-1.6$ ^[17-20]. The variation in water content n is related to the process by which ACC is obtained, two common reactants for carbonate ions being CO_2 gas and sodium carbonate solutions. The composition of ACC phases is thus similar to that of the crystalline monohydrocalcite $\text{CaCO}_3 \cdot \text{H}_2\text{O}$. ACC is less stable than any of the crystalline polymorphs of calcium carbonate CaCO_3 (being calcite, aragonite, vaterite, and ikaite) and ACC rapidly crystallises upon dehydration, typically within 1 hour at room temperature, to either aragonite or calcite^[21-22]. Scanning Electron Microscopy (SEM) shows the transformation of ACC over this hour period via a vaterite phase in figure 1.2.^[22]

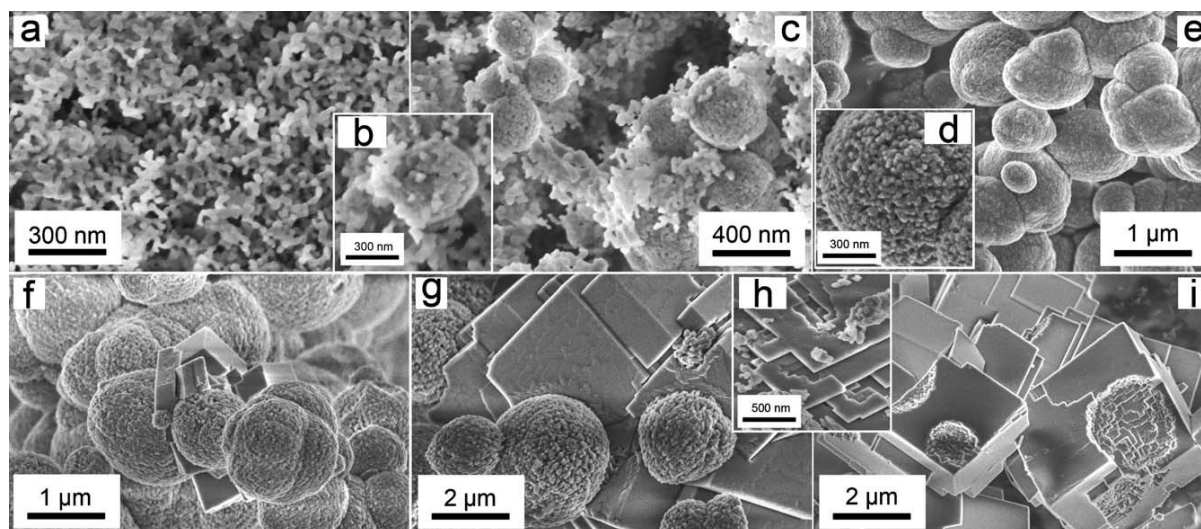


Figure 1.2 – SEM of the transformation of ACC (small spheres in (a)) via vaterite phase (large spheres in (e)) and finally to calcite (large cubes in (i)) over the period of 1 hour.^[22]

Although the term amorphous calcium carbonate has been used to classify calcium carbonates for approximately a century^[22] there remains to be presented a comprehensive set of structural data and corresponding structural model for an ACC phase. Structural characterisation of ACC using infrared and Raman spectroscopy is frequently reported ^[23-24] but is difficult to interpret in terms of disordered atomic structures. X-ray absorption spectroscopy has provided the most direct probe of Ca in ACC phases, and a Ca-O bond length of 2.40Å and coordination number of approximately 6 are typically

reported ^[25]. A key experimental technique for studying the atomic structure of amorphous materials is diffraction over a large angular range of scattering sufficient to obtain information about the pair distribution function ^[26]. However, such diffraction studies of ACC have been limited due to its instability. Notably there was a high energy x-ray diffraction study of two types of ACC reported by Michel et al in 2008^[17].

The x-ray diffraction data of Michel et al^[17] are used for Reverse Monte Carlo (RMC) modelling by Goodwin et al in 2010^[27]. The RMC study reported that the same results were obtained for two different starting configurations: a disordered monohydrocalcite (dMHC) model (i.e. $n=1$), and a random model containing the same molecular units. The RMC model obtained for ACC was reported to have a calcium rich network (referring to Ca-O-Ca linkages) and Ca-poor channels (regions more than 4 Å away from a calcium atom). The RMC fits to data for the $S(Q)$ and $G(r)$ for the dMHC and the random models can be seen in figure 1.3 and the pictorial representation of the computational model is figure 1.4.

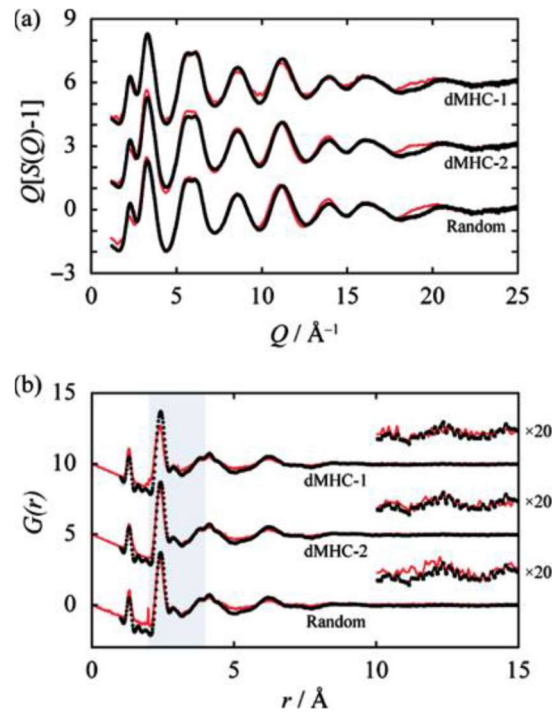


Figure 1.3 – Goodwin fits to data for dMHC and Random models of ACC.^[27]

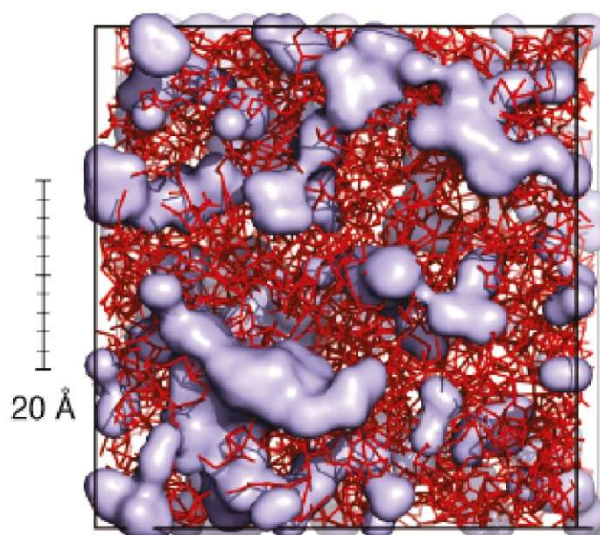


Figure 1.4 – Goodwin computational model, with the calcium poor channels in purple and the calcium framework in red.^[27]

A recent study of the structure of ACC^[28] used a combination of ^{43}Ca NMR and molecular dynamics (MD) modelling. Using the Goodwin et al model as a starting point it was found that the Ca-rich and Ca-poor channels proposed by Goodwin et al undergo “significant structural reorganization” and “shrink in size” during the 2 ns MD simulation.

1.3.1.2 *Magnesium Stabilised Amorphous Calcium Carbonate*

One way to facilitate diffraction studies is to work with more stable forms of ACC which allow more time-consuming experiments to be performed, such as neutron diffraction. The use of both neutron and x-ray diffraction provides important complementary information due to the different scattering powers of elements for neutrons and x-rays. It has been reported that ACC can be stabilised with various additives such as magnesium^[29-31], phosphate^[30], and poly(aspartic acid)^[31]. The present study is focused on Mg-stabilised ACC. The addition of a very small amount of magnesium greatly increases the longevity of the sample because interactions between Mg^{2+} and H_2O molecules slow down the dehydration dynamics^[30]. Another benefit of adding magnesium is the smaller size of the Mg^{2+} ion compared to other potential additives and thus the Mg^{2+} ions should have a minor effect on the structure of “pure” ACC. The use of Mg stabilised ACC has made it possible to measure neutron and x-ray diffraction data which is reported here for the first time.

It has been reported^[32] that in many biological organisms that Mg^{2+} ions have been found alongside ACC which has led some to theorise that the Mg^{2+} ions are present to help stabilise the ACC whilst in the organism.^[33]


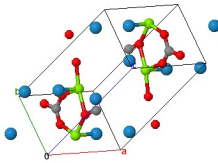
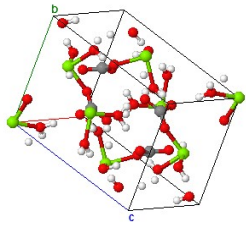
1.3.1.3 *Amorphous Magnesium Carbonate*

Whilst amorphous magnesium carbonate (AMC) is not a biomineral, its similarity in composition to both ACC and Mg-ACC was a strong motivation to study this material.

AMC exists as one of five “simple” polymorphs of magnesium carbonate. Other polymorphs exist but they contain magnesium to hydroxyl bonds (thus making an $\text{Mg}(\text{OH})_2$ molecule for example). These

were determined to be too far detached from the metal-carbonate systems studied in this work and were omitted. The three crystalline variations of magnesium carbonate and the amorphous form are:

Table 1.2 – Polymorphs of magnesium carbonate

Type of Magnesium carbonate	Crystal structure†	Composition	Density (g/cm ³)	Space Group	Unit Cell Dimensions (Å)
Magnesite	 [8][34]	MgCO ₃ Magnesium (green) Carbon (grey) Oxygen (red)	2.958 ^[35]	R3c ^[35] Trigonal – Hexagonal Scalenohedral	a=4.633 ^[35] c=15.150
Nesquehonite	 [36]	MgCO ₃ ·3H ₂ O Magnesium (green) Carbon (grey) Oxygen (red) H ₂ O (blue)	1.836 ^[37]	P2 ₁ /n ^[37] Monoclinic - Prismatic	a=12.00 ^[37] b=5.39 c=7.68
Lansfordite	 [38]	MgCO ₃ ·5H ₂ O Magnesium (green) Carbon (grey) Oxygen (red) Hydrogen (white)	1.730 ^[39]	P2 ₁ /a ^[39] Monoclinic - Prismatic	a=12.48 ^[39] b=7.55 c=7.34
Amorphous Magnesium Carbonate	-	MgCO ₃ ·nH ₂ O	?	?	?

Recently, in 2013, it was reported that super high surface area material (approximately 800 m²/g – a current World Record) magnesium carbonate had been synthesised at the University of Uppsala, Sweden which was named “Upsalite”. This material gathered much attention in the press as it could become a competitor to zeolites which can be used to control moisture levels, as ingredients in laundry detergents and remediate contaminated soils.^[40] The reaction pathway used to produce Upsalite is shown below in figure 1.5

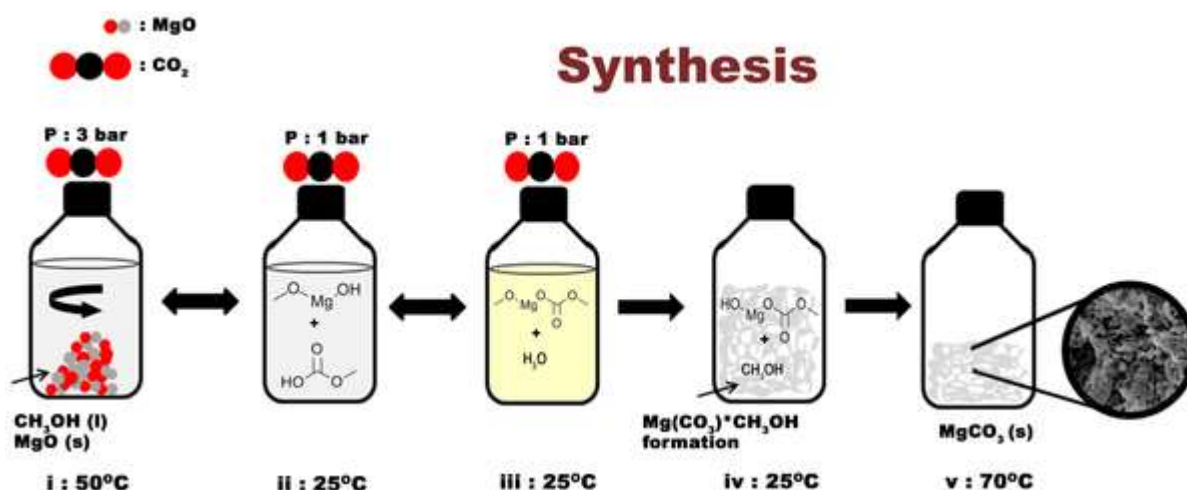


Figure 1.5 – Synthesis pathway of Upsalite^[40]. MgO is added to ethanol and the mixture is stirred in a CO₂ atmosphere whilst being heated to 50°C before the atmospheric pressure and temperature are reduced in stage ii the mixture is then left for several days before the Upsalite has completely formed and settled to the bottom of the reaction liquor.

For this work, the author decided to focus on a ‘traditional’ AMC as Upsalite requires specialised equipment and the Upsalite product still contains some un-reacted starting product (primarily crystalline MgO – see figure 1.6 below)^[40 Support Info.] which would over-complicate structural characterisation of the amorphous material beyond the scope of this work.

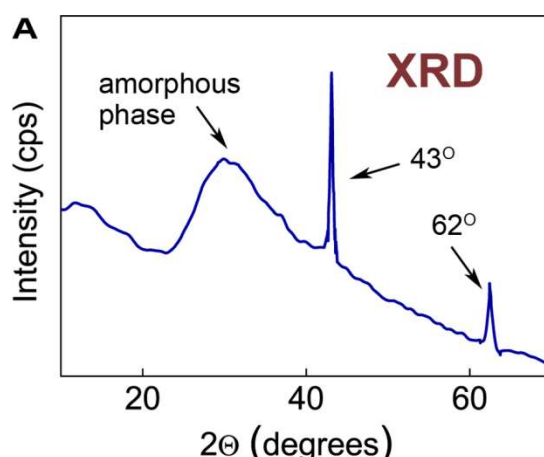


Figure 1.6 – XRD pattern taken for Uppsalite sample shows clearly the presence of an amorphous phase but also the presence of a crystalline phase with sharp peaks at 43° and 62° respectively (these correspond to crystalline MgO)^[40 Support Info.]

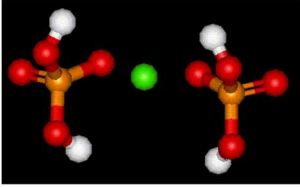
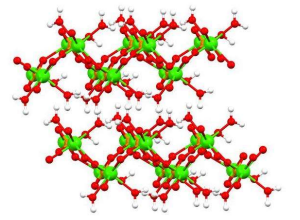
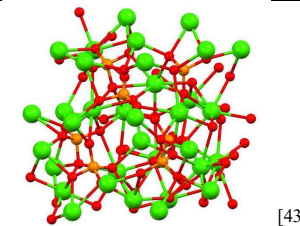
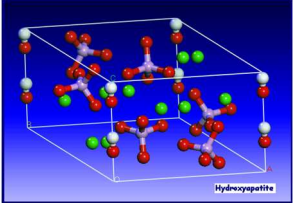
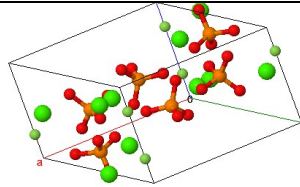
1.3.2 Amorphous Phosphates

1.3.2.1 Amorphous Calcium Phosphate

While ACC is the metastable storage medium for the shells and exoskeletons of marine organisms, amorphous calcium phosphate (ACP) is the human analogue. ACP is found within the bones of humans and other mammals. Thought to be performing a similar role to ACC, ACP is a storage facility for calcium within the endoskeleton of mammals.

ACP is part of a wide-ranging family of calcium phosphate materials. The most common of these are:

Table 1.3 – Polymorphs of calcium phosphate

Type of Calcium Phosphate	Crystal structure†	Composition	Density (g/cm ³)	Space Group	Unit Cell Dimensions (Å)
Monocalcium phosphate	 [41]	Ca(H ₂ PO ₄) ₂ Calcium (green) Phosphorous (orange) Oxygen (red) Hydrogen (white)	2.220 ^[41]	Ia ^[41] Monoclinic	a=5.812 ^[41] b=15.180 c=6.239
Dicalcium phosphate	 [42]	CaHPO ₄ Calcium (green) Phosphorous (orange) Oxygen (red) Hydrogen (white)	2.929 ^[42]	P1 ^[42] Triclinic	a=6.910 ^[42] b=6.627 c=6.998
Tricalcium phosphate	 [43]	Ca ₃ (PO ₄) ₂ Calcium (green) Phosphorous (orange) Oxygen (red)	3.140 ^[44]	P2 ₁ /a ^[43] Monoclinic	a=12.887 ^[43] b=27.280 c=15.219
Hydroxyapatite	 [45]	Ca ₅ (PO ₄) ₃ (OH) Calcium (green) Phosphorous (purple) Oxygen (red) Hydrogen (white)	3.08 ^[46]	P6 ₃ /m ^[46] Hexagonal - Dipyramidal	a=9.41 ^[46] c=6.88
Apatite	 [47]	Ca ₁₀ (PO ₄) ₆ (x) ₂ where x = OH, F, Cl or Br Calcium (light green) Phosphorous (orange) Oxygen (red) x (dark green)	Various	P6 ₃ /m ^[47] Hexagonal – Dipyramidal	a=9.38 ^[47] c=6.89
Amorphous calcium phosphate	-				

Calcium phosphates and ACP have been widely studied due to their suitability within mammalian organisms. One field where calcium phosphates have been widely applied is dentistry, calcium phosphates, particularly hydroxyapatite have shown great promise in coatings for teeth and cements/fillings.^[48-49]

Previous work on the structural characterisation of ACP was conducted at the University of Kent using heat treatments to reduce hydrogen content.^[50] The reduction of hydrogen content was beneficial for the neutron scattering experiments that were performed (to reduce inelastic scattering of neutrons). Heat treatment at 200°C and 450°C were conducted after TGA analysis indicated two regions of water loss at these temperatures. The data from these experiments were used for Reverse Monte Carlo (RMC) modelling and the fits to data and pictorial model are figures 1.7 and 1.8 respectively

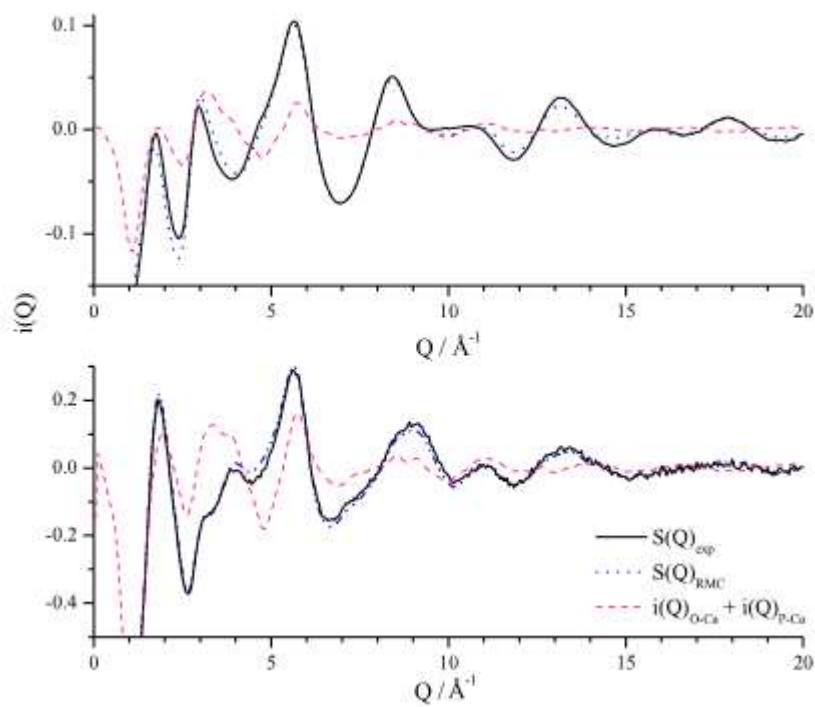


Figure 1.7 - RMC fit to experimental $i(Q)$: (top) RMC fit to neutron diffraction data and (bottom) RMC fit to x-ray diffraction data.^[50]

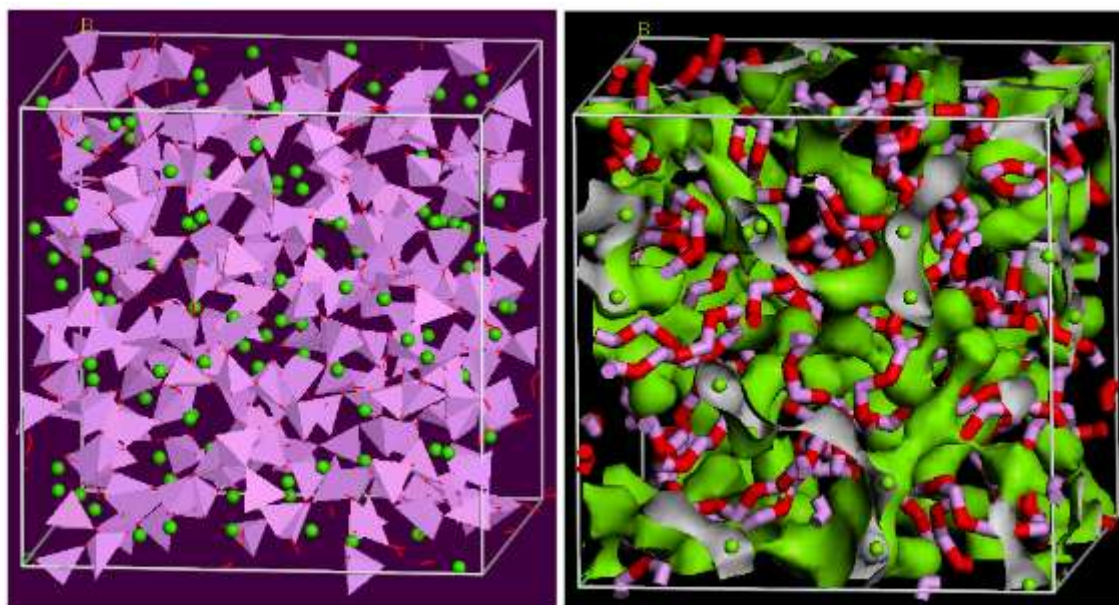


Figure 1.8 - The RMC model of ACP. (Left) The phosphate units as purple tetrahedra and the green calcium ions as spheres. (Right) The -P-O-P-O- backbone (purple and red chain) and the calcium clusters (green surface).^[50]

Analysis of the data and the RMC model found that the Ca-O correlations had a broad distribution mostly around 2.35Å but some up to 3.0Å. In addition the P-O correlation was sharply defined as 1.8Å due to heavy restraint within the RMC modelling. It was also stated that the average bond angle for the P-O-Ca was 127° which agrees with the experimental diffraction data.^[50]

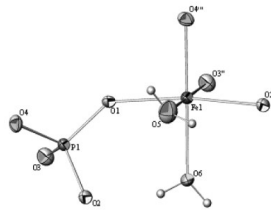
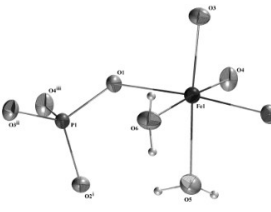
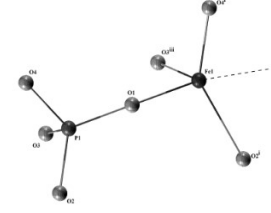
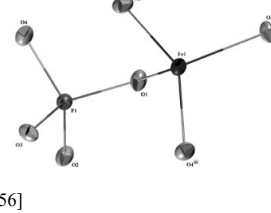
The author wishes to extend this work and carry out neutron and x-ray diffraction of ACP before doing RMC modelling on the data. However, instead of the heat-treated ACP that Wetherall et al^[50] studied, the author will attempt to prepare a deuterated sample of ACP and study that.

1.3.2.2 Amorphous Iron Phosphate

One of the major drawbacks with Amorphous calcium phosphate (ACP) is limited chemical durability^[51]. Greaves et al^[52] attributed this to P-O-P bonds being easily hydrated, in the same work it was detailed that addition of iron oxides replaces the P-O-P bond with the more stable P-O-Fe bond. These more stable iron phosphates, which include amorphous iron phosphate (AFP), have shown promise in being applied to make laser materials and to dispose/contain nuclear waste.^[53-55]

Iron phosphates exist with either Fe²⁺ or Fe³⁺ ions. The most common iron phosphates with both ions are displayed in table 1.3 below.

Table 1.3 – Polymorphs of iron phosphate

Type of Iron Phosphate	Crystal structure†	Composition	Density (g/cm ³)	Space Group	Unit Cell Dimensions (Å)
Monoclinic iron phosphate dihydrate	 [56]	FePO ₄ ·2H ₂ O	2.87 ^[56]	P2 ₁ /n ^[56] Monoclinic	a=7.560 ^[56] b=8.081 c=5.012
Orthorhombic iron phosphate dihydrate	 [56]	FePO ₄ ·2H ₂ O	2.87 ^[56]	Pnma ^[56] Orthorhombic	a=9.814 ^[56] b=5.789 c=4.782
Monoclinic iron phosphate	 [56]	FePO ₄	3.056 ^[56]	P2 ₁ /n ^[56] Monoclinic	a=5.480 ^[56] b=7.480 c=8.054
Orthorhombic iron phosphate	 [56]	FePO ₄	3.056 ^[56]	Pbca ^[56] Orthorhombic	a=9.171 ^[56] b=9.456 c=8.675
Amorphous iron phosphate	-	FePO ₄ ·nH ₂ O	?		

It has been documented that some of the polymorphs in table 1.4 are also found in the mineral kingdom.^[56-57]

In recent years, work has been conducted on iron phosphates as additives to lithium ion batteries, these new batteries are known as lithium iron phosphate batteries (LFP).^[58] This work is of great significance as the lithium ion industry is growing exponentially each year. Benefits of LFP batteries over conventional lithium cobalt oxide batteries are that the LFP batteries have a greater power density, longer lifetime (approximately more than 10 years) and are safer.^[59-62]

At the University of Kent, a previous study was conducted on amorphous iron phosphates using experimental data and molecular dynamics (MD) simulation.^[63]

A range of iron phosphate glasses were prepared and studied using neutron and x-ray diffraction, these experimental data were then modelled using the MD software package DL_POLY. The results from these MD simulations can be seen below in figures 1.9 and 1.10.

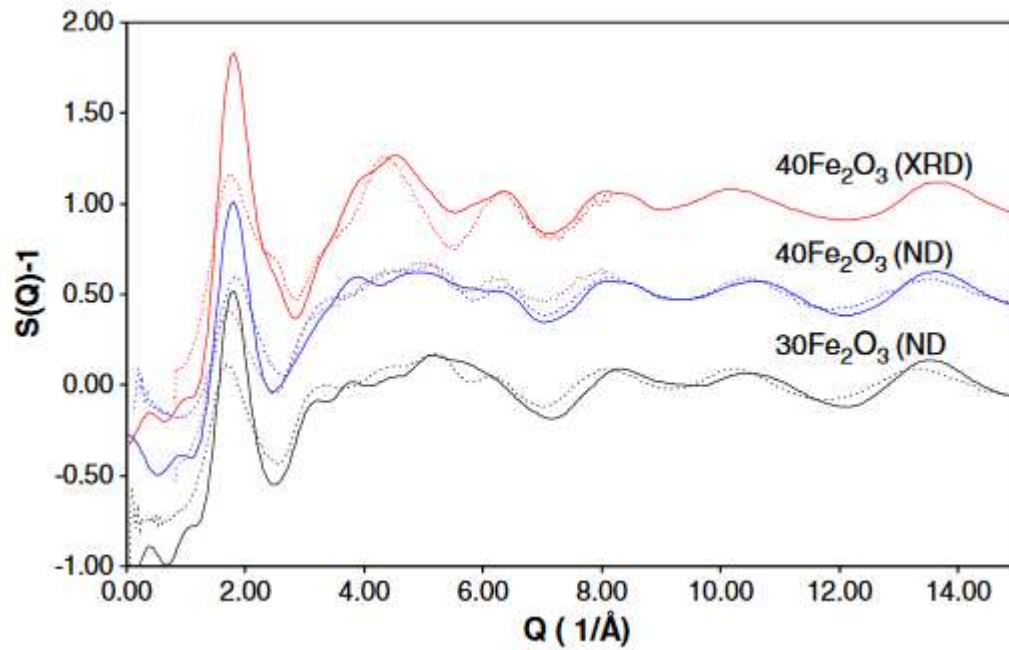


Figure 1.9 - MD fits to neutron and x-ray diffraction $S(Q)$ for iron phosphate glasses of varying compositions.^[63]

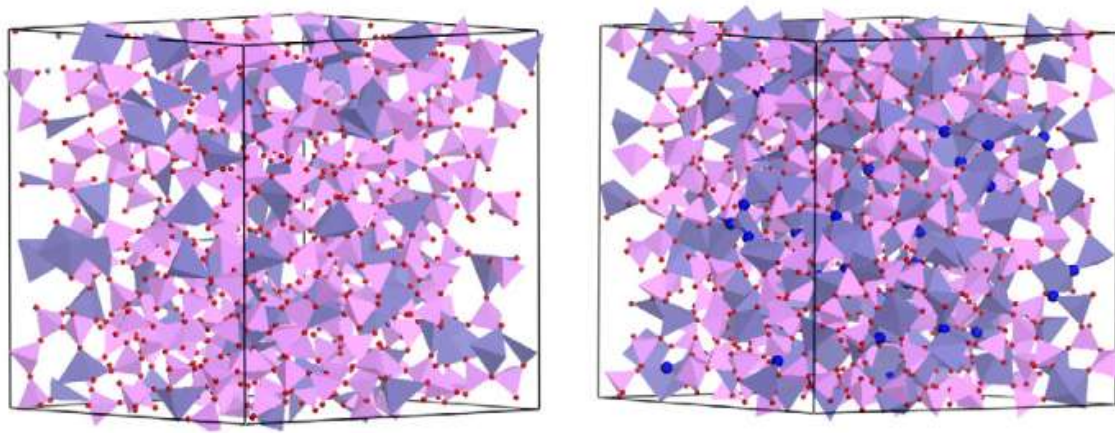


Figure 1.10 - Iron phosphate glasses models showing the phosphate tetrahedrals, the larger (blue) spheres are non network oxygen that are not bonded to a phosphorous.^[63]

The results from Al-Hasani et al^[63] showed good agreement with the previously reported experimental results from Hoppe^[64] and Wright^[65]. These being that the P-O-P bond angle has a broad distribution around 151° and the Fe-O bond length being approximately 1.90 \AA .

In the current work, the author will be attempting to recreate the MD simulations from Al-Hasani et al^[63] on AFP using the RMC method and compare results.

1.3.3 Amorphous Sulfates

1.3.3.1 Amorphous Calcium Sulfate

In 2012, a paper published by Wang et al^[66], detailed a new precipitation pathway for calcium sulfate dihydrate (commonly known as gypsum) via an amorphous precursor. This was the first evidence of an amorphous calcium sulfate (ACS) precursor. A tunnelling electron microscope (TEM) image of the amorphous precursor is figure 1.11.

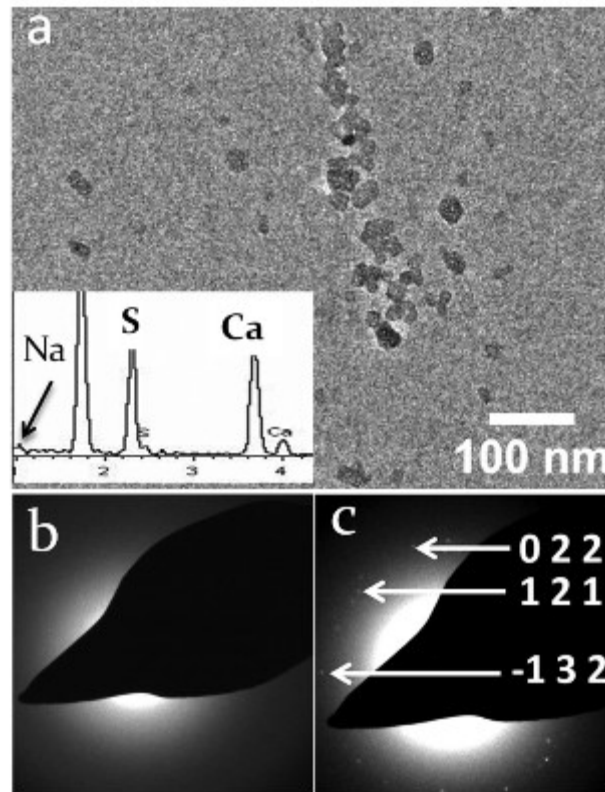
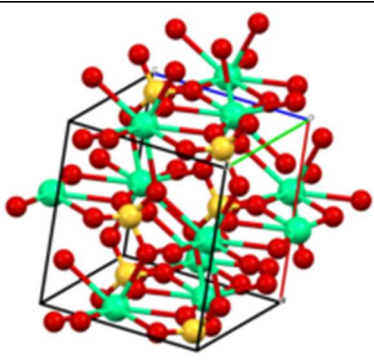
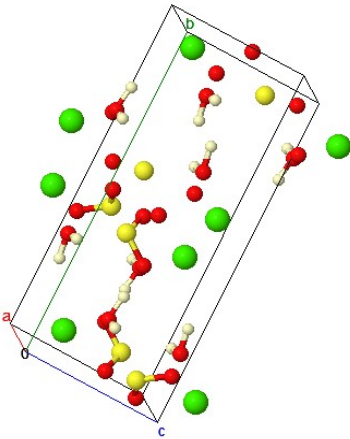
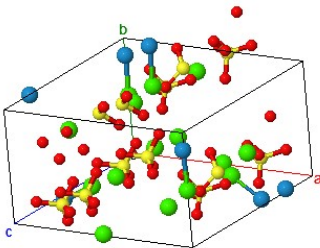


Figure 1.11 - Tunnelling electron microscope (TEM) images of ACS (a) 1 minute after precipitation, (b) the selected area electron diffraction pattern of ACS, showing it is amorphous and (c) ACS after irradiation with electron beam showing crystallisation of CaSO_4 ^[66]

Whilst calcium sulfate is not directly a biomineral, there have been studies that indicate the calcium sulfate can help with bone growth and defects as illustrated by Orsini et al^[67] in their animal testing on rabbits. Calcium sulfates close resemblance to similar materials such as calcium carbonate and calcium phosphate was additional reasoning to warrant further study of this material, both in this work and in the wider scientific community.

Amorphous calcium sulfate is one of four polymorphs currently known and these are detailed in table 1.5 below:

Table 1.5 - Polymorphs of calcium sulfate

Type of Calcium Sulfate	Crystal structure†	Composition	Density (g/cm ³)	Space Group	Unit Cell Dimensions
Calcium sulfate anhydrite	 [68]	CaSO ₄ Calcium (green) Sulfur (yellow) Oxygen (red)	2.960 ^[69]	Amma ^[68] Orthorhombic – Dipyramidal	a=6.991 ^[68] b=6.996 c=6.238
Calcium sulfate dihydrate	 [70]	CaSO ₄ ·2H ₂ O Calcium (green) Sulfur (yellow) Oxygen (red) Hydrogen (white)	2.320 ^[71]	2m ^[70] Monoclinic – Prismatic	a=5.679 ^[70] b=15.202 c=6.522
Calcium sulfate hemihydrate	 [72]	CaSO ₄ ·0.5H ₂ O Calcium (green) Sulfur (yellow) Oxygen (red) H ₂ O (blue)	2.700 ^[71]	B2 ^[72]	a=12.031 ^[71] b=6.296 c=12.671
Amorphous calcium sulfate	-	CaSO ₄ ·nH ₂ O	?		

Additionally, Wang et al published a second paper in 2012 on the subject of ACS and proposed that additives could be added to the precipitation solutions to stabilise the calcium sulfate hemihydrate (bassanite) phase and the amorphous phase. Without the presence of additives, ACS would fully crystallise to calcium sulfate dihydrate within 2 hours of synthesis. The additives proposed in this paper were poly(acrylic acid), poly(styrene-4-sulfonate), sodium triphosphate and magnesium ions. Results from this work show that all four additives had an effect on calcium sulfate precipitation with

the most effective being poly(acrylic acid) which could stabilise the hemihydrate and amorphous phases at lowest concentrations (3000 µg/ml), the triphosphate and magnesium additives were effective but required higher concentrations in order to achieve the same level of stabilisation as with poly(acrylic acid).^[73]

Whilst, the addition of additives would be beneficial to the stability of ACS, adding large polymers (full of hydrogen) were deemed to be too much of a detriment to the sample of ACS for neutron diffraction.

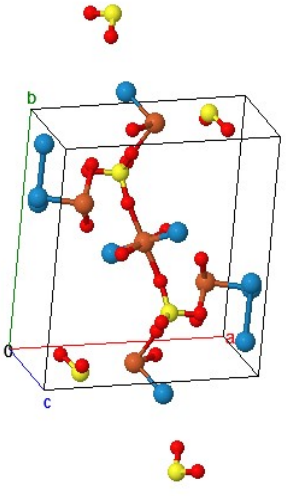
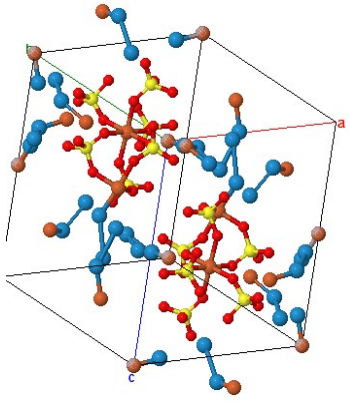
1.3.3.2 Amorphous Iron Sulfate

Amorphous Iron Sulfate (AFS) came to the attention of the research community when a Mars Rover mission^[74] returned analysis of the Martian surface which found areas of gypsum (crystalline calcium sulfate) and the interesting discovery of amorphous materials such as iron oxides, calcium sulfates and AFS.

The surface of Mars makes an ideal environment for the propagation and production of AFS as there is no atmospheric water. This is beneficial because AFS is hygroscopic and atmospheric water would present complications and retard the growth of AFS and cause the material to appear as a red-yellow glass like material compared to the yellow powder when AFS is prepared without the presence of atmospheric water.

Amorphous iron sulfate is one of 4 polymorphs of iron (III) sulfate, however, the anhydrous form is exceedingly rare, and these are given in Table 1.6:

Table 1.6 - Polymorphs of iron sulfate

Type of Iron Sulfate	Crystal structure†	Composition	Density (g/cm ³)
Iron sulfate pentahydrate	 [75]	Fe ₂ (SO ₄) ₃ ·5H ₂ O	1.898 ^[76]
Iron sulfate nonahydrate	 [77]	Fe ₂ (SO ₄) ₃ ·9H ₂ O	2.11 ^[76]
Amorphous iron sulfate	-	Fe ₂ (SO ₄) ₃ ·nH ₂ O	?

From the literature, no synthesis of AFS had been published at the time of carrying out this project. However, after completion of the project in 2014 a study of amorphous iron sulfates was presented at the American Geophysical Union by Sklute et al^[78].

1.4 Project Aims

Using the information presented in sections above, the aims of this work are to investigate the unknown atomistic structures of the materials presented in the introduction. As an additional line of enquiry, does ACC (or any of the other minerals in this chapter) exhibit the calcium-rich and calcium-poor regions as shown by Goodwin et al^[27]. In summary, the aims of this project are;

- Successfully synthesise stable forms of the amorphous materials of study.
- Conduct experimental diffraction (neutron and x-ray) studies of these stable materials.
- Use the data from these experiments to produce atomistic models of the amorphous materials.

2. Theoretical Background

2.1 Diffraction of non-crystalline solids

2.1.1 Pair correlation function

2.1.1.1 Crystalline materials

Crystals are composed of a regular three-dimensional distribution of atoms that is represented by a unit cell. A unit cell describes the smallest symmetrical configuration that can be periodically repeated to form the crystalline structure. The structure of the crystal is provided by the size and shape of the unit cell and the atomic coordinates inside the unit cell (or “basis”).

In a crystalline solid the positions of atoms follow the crystal lattice. Each atom i has a position \mathbf{R}_i which is at a certain point in the lattice

Equation 2.1
$$\mathbf{R}_i = n_x \mathbf{a} + n_y \mathbf{b} + n_z \mathbf{c}$$

where \mathbf{a} , \mathbf{b} and \mathbf{c} are the lattice vectors of the unit cell, and n_x , n_y and n_z are integers.

2.1.1.2 Non-crystalline materials

The fundamental definition of an amorphous material is that they are non-crystalline. Unlike crystalline materials, their basis can be described as infinite and therefore statistically have a randomised structure. An amorphous solid may have a certain degree of local order over a short length scale. This can include repeated atomic structures such as tetrahedral units. Their structure can therefore be described by their short-range localised order, which is not periodically repeated over a larger length scale [1].

In a non-crystalline solid, there is no lattice, so each atom i has a position $\mathbf{R}_i = (x_i, y_i, z_i)$ which cannot be predicted.

Instead, it is informative to consider the distances between atoms, or interatomic distances. For example, the vector between atoms i and j is

Equation 2.2
$$\mathbf{R}_{ij} = \mathbf{R}_j - \mathbf{R}_i = (x_j - x_i, y_j - y_i, z_j - z_i)$$

(In a crystalline solid, this vector will be defined in terms of the lattice vectors.) In a non-crystalline solid, there is disorder in the interatomic distances, and a distribution function is defined. This is referred to as the pair correlation function (or alternatively pair distribution function or radial distribution function).

Firstly, in a non-crystalline solid there is no preferred axis or orientation, so only the magnitude (and not the direction) of the interatomic distance is important.

Equation 2.3
$$R_{ij} = |\mathbf{R}_{ij}| = [(x_j - x_i)^2 + (y_j - y_i)^2 + (z_j - z_i)^2]^{0.5}$$

Secondly, due to disorder, it is important to take the average over all possible central atoms i such that the pair correlation function is

Equation 2.4
$$g(r) = 1/N \sum_i \sum_{j \neq i} \delta(r - R_{ij})$$

where N is the number of atoms and δ is a counting function.

2.1.1.3 *Extraction of the Structural Information*

The advantage of the pair correlation function is that it can be determined experimentally from the structure factor measured in a diffraction experiment. In addition, it can be determined computationally from a computer model which contains the coordinates \mathbf{R}_i of all atoms.

The structural information is held in the pair correlation function. Amorphous structures are short-range and so at low distances the distribution of neighbouring atoms become features of the pair correlation function as peaks. Each peak at a certain distance corresponds to an interatomic distance and the area underneath the peak relates to the number of atoms at that distance. The larger the peak, the more atoms are at that particular distance.

2.1.2 *Theory of diffraction*

2.1.2.1 *Concept of Wave-Particle Duality*

Neutrons and X-rays have the ability to behave as particles and waves. These properties are interchangeable, for example neutrons are created as particles but they behave as waves when they are scattered in a scattering experiment. A massive particle traveling at constant velocity, v , is related to the de-Broglie wavelength [r2]

Equation 2.5
$$\lambda = \frac{2\pi\hbar}{mv}$$

2.1.2.2 *General Scattering Theory in Crystals*

The diffraction pattern produced from the scattered radiation is described using Bragg's Law for a crystal, which relates the wavelength λ , the inter-planar distance d and the angle between the incident/diffracted ray and the crystal plane θ ,

Equation 2.6
$$n\lambda = 2 d \sin \theta$$

where n is the order of diffraction.

The inter-planar distance separates the lattice planes and the waves are scattered from these planes in the crystal. The path length is exactly one wavelength (for $n=1$) and so the scattered waves constructively interfere, at the angle calculated using the law, as they remain in phase. This then produces the diffraction pattern [r3].

2.1.2.3 *General Scattering Theory in Amorphous Materials*

A scattering event is characterized by the resultant change in the particle's momentum and energy. A change in the momentum results a change in the direction and/ or the velocity of the neutron or X-rays [r4]. The momentum is given as

Equation 2.7
$$\rho = \hbar k / 2\pi$$

Where k is the wave vector $k = 2\pi/\lambda$.

The resultant interference pattern corresponds to the information of the structural arrangement of the atoms. The scattering intensity I is a function of the incident and scattered wave vectors [r5].

Equation 2.8
$$I = I(Q)$$

The scattering vector, Q , is defined as the momentum change for a scattering event and represented as the difference in the wave vectors between the incident and scattered waves.

Equation 2.9
$$Q = k_{incident} - k_{scattered}$$

Therefore, the dependence of the scattering intensity I on the scattering vector Q is linked with the structural information of the sample. The change in momentum for the scattering event arises from substituting equation 2.9 into equation 2.7 to yield

Equation 2.10
$$\rho = \hbar Q$$

Where \hbar is the reduced Planck's constant $\hbar = h/2\pi$.

The law of conservation of energy is used to describe the energy exchange between the incident neutron and the sample. For the purpose of determining the structure of a solid, only the elastic scattering of the sample is taken into account and therefore the total change in energy is zero. Using this knowledge, equation 2.9 and the simple trigonometric relationship in figure 2.1, the following for the wave vector transfer [r6]

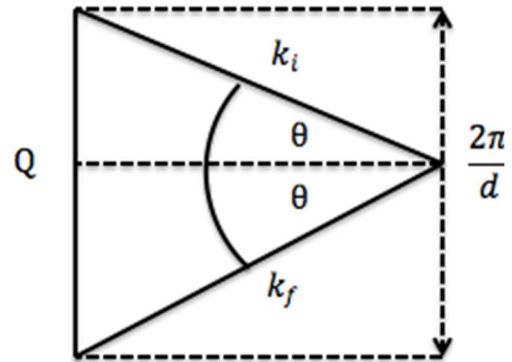


FIGURE 2.1: Illustration of trigonometric relationship between the scattering

Equation 2.11

$$|Q| = 2k_{incident} \sin \theta$$

2.1.2.4 Scattering from a single atom

A constant beam of particles with fixed wavelength and travelling in the z direction can be described as a complex plane wave

Equation 2.12

$$\varphi_i = \varphi_o e^{ikz}$$

An interaction with a fixed single atom will produce the particles to move radially outward if the origin is centred on the atom. The scattered wave will then take the form of a spherical wave as a result of this

Equation 2.13

$$\varphi_{scattered} = \varphi_{initial} f(Q) \frac{e^{ikr}}{r}$$

2.1.2.5 Scattering from multiple atoms

Figure 2.2 shows a simple illustration of an atom at an interatomic distance, vector \mathbf{r} , relative to the origin O. The atom is located at point P [r7].

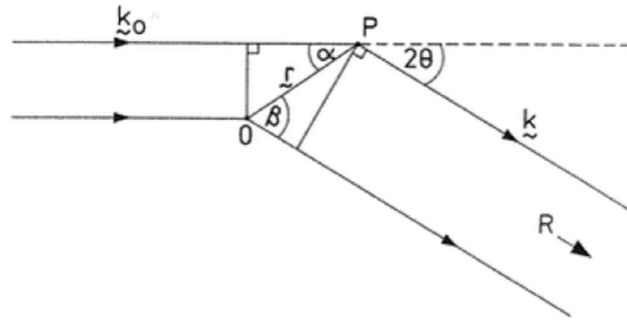


FIGURE 2.2: Illustration of scattering for multiple atoms.

This setup will produce a phase difference Φ between the scattered waves at the event and the detected waves [r7].

Equation 2.14
$$\Phi = \frac{2\pi(rcos\alpha - rcos\beta)}{\lambda}$$

Within this relation

Equation 2.15
$$\mathbf{r} \cdot \mathbf{k}_{initial} = \left(\frac{2\pi}{\lambda}\right) rcos\alpha$$

Equation 2.16
$$\mathbf{r} \cdot \mathbf{k}_{final} = \left(\frac{2\pi}{\lambda}\right) rcos\beta$$

And so through substitution, the phase difference becomes

Equation 2.17
$$\Phi = (\mathbf{k}_{initial} - \mathbf{k}_{final}) \cdot \mathbf{r} = \mathbf{r} \cdot \mathbf{Q}$$

And the amplitude of the scattered wave is as follows

Equation 2.18
$$A_1(Q) = f(Q)e^{ir \cdot Q}$$

As mentioned in previous sections, the form factor $f(Q)$ represents the scattering length for neutron scattering and the corresponding form factor for X-ray scattering. For multiple atoms, the amplitudes are combined as a summation over all the atoms p in the sample, taking into account their relative phase [r7].

Equation 2.19
$$A_{multiple}(Q) = \sum_P f_p(Q) e^{ir \cdot Q}$$

The scattered intensity is produced by multiplying $A_1(Q)$ by its complex conjugate. The intensity only depends on the interatomic distances regardless of the origin.

Equation 2.20
$$I_{multiple}(Q) = \sum_P \sum_q f_p(Q) f_q(Q) e^{ir_{pq} \cdot Q}$$

The scattered intensity for multiple atoms can be written in terms of the scattering length for neutron scattering, whereas the equation remains the same for X-ray diffraction. As mentioned in later sections, the scattering length depends on the isotopes within the sample and so to convert the above equation, the substitution is the average value for each element that is present [r7].

Equation 2.21
$$I_{multiple}(Q) = \sum_P \overline{b_p^2} + \sum_{p \neq q} \sum \overline{b_p} \overline{b_q} e^{ir_{pq} \cdot Q}$$

The bar represents averaging over isotopes for a given element [r7].

The first term is a result of the incoherent scattering (a component of self-scattering) and does not depend on the interatomic distances. The incoherent term arises from the sum of the intensities of scattering by individual nuclei. The waves scattered by different nuclei will not produce an interference pattern. For amorphous materials, there will be some incoherent scattering due to the randomised distribution of the atoms, however, this will not provide structural information [r6] [r8].

The second term describes the coherent scattering (from the distinct scattering) and this term describes the connection between the positions of the atoms. The coherent term arises from averaging the isotopes of each element in the structure and depends on the interference of the scattered waves. The coherent scattering cross section holds the structural information [r6] [r9] and is given as

Equation 2.22
$$\sigma_{coh} = 4\pi(\overline{b})^2$$

2.1.2.6 *Scattering Length for neutron scattering*

The form factor $f(Q)$ depends on wavelength and scattering angle. For neutron diffraction, these terms do not change and so the result is

Equation 2.23
$$f(Q) = b$$

The term b is the scattering length and depends on the nucleus of the atom [r5]. The scattering length depends on the isotope because of its dependence on the nucleus however it does not distinguish between atomic numbers of elements.

2.1.2.7 *Form Factor for x-ray scattering*

There are significant differences between the scattering of X-rays and neutrons by atoms but they can be treated as complementary to each other. The form factor $f(Q)$ where Q is defined in equation 2.23. The interaction of X-rays is long-range and electromagnetic with the electrons within the atoms. As a consequence of these properties, the form factor $f(Q)$ for X-ray scattering diminishes as Q increases. The form factor $f(Q)$ for X-ray scattering is proportional to the atomic number. The form factor $f(Q)$ for X-rays is very different compared to neutrons because the interaction from the neutrons is short-range and so enables measurements to a higher value of Q [r6].

2.1.2.8 *Total Scattering Cross Section*

This is related to the scattering length and given by

Equation 2.24
$$\sigma_{total} = 4\pi b^2$$

The total scattering cross-section σ_{total} is a combination of the scattering cross-section σ_{scatt} and the absorption cross-section σ_{abs} . The absorption cross section arises from the likelihood of a neutron being absorbed rather than scattered and this reduces the measured scattered events. The probability of absorption for neutron scattering is small. To account for the likelihood of absorption events, the sample is treated as a box with containing a proportion of absorption cross sections. The number of absorption cross sections depends on the depth of the box itself and the total number of nuclei in the beam. The final intensity of the beam I_{Final} emerging from the box can be described with an exponential law relating the initial intensity $I_{initial}$, the depth of the box, x , and the linear absorption coefficient, μ , as follows.

Equation 2.25

$$I_{Final} = I_{initial} e^{-\mu x}$$

The linear absorption coefficient arises from the composition of the atoms within the box and the total cross section of the material. The total cross section is further dependent on the weighted summation of the absorption and scattering coefficients of the individual atoms.

Equation 2.26

$$\mu = \frac{N\sigma\rho}{A}$$

where

μ = linear absorption coefficient (cm^{-1})

N = Avogadro's number (6.022169×10^{23})

σ = total cross section (barns = 10^{-24} cm^2)

ρ = density of absorber material (g cm^{-3})

A = atomic weight of the absorber atoms (g)

2.1.2.9 *Differential Cross Section*

The total scattering cross section is deduced as the ratio of scattering events per fixed time to the incident flux Φ [r6]. The differential cross section arises from the scattered neutrons α in a sample containing N atoms at a solid angle and defined by

Equation 2.27

$$\frac{d\sigma}{d\Omega} = \frac{\alpha}{N\Phi d\Omega}$$

The energy distribution of the scattered neutrons is described by the differential cross section, which is analogous to a physical target. The differential cross section is produced from the processed raw data, which has been corrected [r6].

2.1.2.10 *Total Structure Factor*

Since the coherent scattering produces the structural information, the incoherent scattering result is omitted.

The coherent partial differential cross section is defined as

Equation 2.28
$$\frac{d^2\sigma}{d\Omega dE_{coh}} = \int \frac{d^2\sigma}{d\Omega dE_{coh}} dE = \frac{k_{final}}{k_{initial}} \frac{\sigma_{coh}}{4\pi} NS(\mathbf{q}, \omega)$$

Where $S(\mathbf{q}, \omega)$ is defined as the total structure factor and describes the effect of the atomic structure and the term σ_{coh} describes the effect of the nuclei [r9]. The Fourier transform of the total structure factor with respect to \mathbf{q} and ω provides the time dependent pair correlation function [r6].

Equation 2.29
$$G(\mathbf{r}, t) = \frac{\hbar}{(2\pi)^3} \iint S(\mathbf{q}, \omega) e^{-i(\mathbf{q}\cdot\mathbf{r} - \omega t)} d\mathbf{q} d\omega$$

Completed, this forms the particle density operator, which shows that the time dependent pair correlation function becomes independent of t as time approaches infinity.

Equation 2.30
$$\rho(\mathbf{r}, t) = \sum_m \delta(\mathbf{r} - \mathbf{R}_m(t))$$

The elastic scattering is represented by the $\delta(\hbar\omega)$ term in the total structure factor [r9] [r8].

2.1.2.11 *Weighting Factors*

For neutron diffraction, the total structure factor is equal to the weighted sum of the partial structure factors [r9].

Equation 2.31
$$S(\mathbf{q}) = \sum_{AB} \omega_{AB} S_{AB}(\mathbf{q})$$

Consequently, the pair correlation function $g(\mathbf{r})$ is the Fourier transform of the structure factor and so is also equal to the weighted sum of the partial correlation functions

Equation 2.32
$$g(\mathbf{r}) = \sum_{AB} \omega_{AB} g_{AB}(\mathbf{r})$$

The term ω_{ab} corresponds to the weighting factors of elements A and B (which are interchangeable) with concentrations c_A and c_B respectively and is given as

Equation 2.33
$$\omega_{ab} = \frac{c_A c_B \overline{b_A b_B}}{\bar{b}^2}$$

The weighting factors are required for the modelling because they describe the scattering power of the different types of atoms according to their concentrations and cross sections. The weighting factors for X-ray diffraction and neutron diffraction are not the same because of the dependence scattering cross sections, which are different between X-ray and neutron.

2.1.2.12 *Structure Factor*

The coherent partial cross section in equation 2.28 and the structure factor written in terms of the time dependent pair correlation function

Equation 2.34
$$S(\mathbf{q}) = \int S(\mathbf{q}, \omega) d\hbar\omega = \int G(\mathbf{r}, 0) e^{i\mathbf{q}\cdot\mathbf{r}} d\mathbf{r}$$

At $t=0$, the operators $\rho(\mathbf{r}, t)$ commute and the time dependent pair correlation function is written in terms of the pair distribution function $g(\mathbf{r})$ which is therefore the Fourier transform of the structure factor [r9].

Equation 2.35
$$G(\mathbf{r}, 0) = \rho_0 g(\mathbf{r}) + \delta(\mathbf{r})$$

For amorphous materials, the pair correlation function $g(r)$ only depends on the interatomic distance r .

2.1.3 *Diffraction experiments*

2.1.3.1 *Diffraction measurement*

A diffraction experiment involves a measurement of the intensity as a function of the magnitude of the scattering vector, Q [r7]. For a variation in the scattering vector, there are two possible methods corresponding X-ray and neutron diffraction experiments, which is purely a consequence of the type of radiation. During an X-ray diffraction experiment, the variation in the scattering vector arises from measurements over a range of angles with a fixed wavelength. Conversely, the variation in the scattering vector for a time of flight neutron diffraction experiment results from a variation in the wavelength at a fixed angle.

2.1.3.2 *Neutron Diffraction Experiment*

Neutrons are subatomic particles that hold no charge and have a mass close to that of the proton. They interact with nuclei through the strong force and have a magnetic moment [r2]. Additionally, the unique interactions between neutrons and matter are highly complex between their nuclear spins and magnetic moments and so their ability to penetrate matter is not dependent the element [r4].

A pulsed neutron source was used to produce the neutron diffraction. A pulsed neutron source is ideal because of the wide range of Q values. The spallation target produces a pulse of neutrons with a pulse width from colliding a target comprised of heavy elements with high-energy protons [r2]. A moderator reduces the neutron velocity and its thickness is chosen to maximise the flux as a function of wavelength [r7].

Therefore, the scattering experiment uses the time of flight method. The detector measures the scattered neutrons with varying wavelengths at a fixed angle. The varying wavelengths provide a variation in the scattering vector. This produces the following relation [r6]

Equation 2.36
$$\lambda(t) = \frac{2\pi\hbar}{mL} t$$

There are advantages to using neutrons to probe atomic structure. The most relevant for this project is that the wavelength of the neutrons is similar to inter-atomic distances and so they can be used in a diffraction experiment to probe atomic structures. Additionally, they have a weak interaction with solids and so are highly penetrating and can be used to probe into the depth of the sample.

2.1.3.3 *Synchrotron X-Ray Diffraction Experiment*

X-rays are electromagnetic radiation occurring in the electromagnetic spectrum between the ultra-violet region and γ -rays. They are generated from colliding high-energy electrons with matter (usually a metal anode target). The electrons undergo an extreme deceleration and the change in kinetic energy produces the X-rays. Two types of radiation are produced: a broad spectrum called white radiation and multiple monochromatic wavelengths [r11].

The experimental data was produced from a diffraction experiment that used synchrotron radiation, which is produced when electrons, travelling at relativistic speeds, are deflected in magnetic fields. The synchrotron contains a series of storage rings and magnets guide the electrons. As the electrons intersect the magnetic field perpendicular to their direction, they experience a force perpendicular to both the direction of the electrons and the magnetic field thus travelling in a circular orbit. The X-rays are produced tangentially because the electrons are being radially accelerated within the magnetic field. The radiation produced is continuous, which allows for specific wavelengths to be selected with a monochromator and is heavily collimated, which improves resolution [r12] [r10].

2.1.3.4 *Normalisation and Background Correction*

An important part of data correction for this project is the normalisation of the experimental data. The variations of flux with time are corrected by dividing the number of events by the monitor counts [r6]. The background scattering is also measured with the absence of the sample and this is subtracted from the raw data.

2.1.3.5 *Incoherent Compton Scattering (X-Ray)*

The difficulty in X-ray diffraction experiments is due to the presence of incoherent Compton scattering, which amplifies at high values of the scattering vector, Q . This is eliminated by a choice of two methods. The Compton scattering can be reduced by using a monochromator during the experiment itself or the coherent scattering is extracted from the total scattering intensity using background fitting techniques [r7].

2.1.3.6 *Attenuation Correction (Neutron)*

Attenuation of the single scattering cross section is a result of the combination of multiple scattering and absorption. The attenuation cross-section σ_{att} is equal to a combination of the scattering and absorption cross section. At large wavelengths, the combination of the absorption σ_{abs} and incoherent cross sections σ_{inc} is dominant.

Equation 2.37
$$\sigma_{att} < \sigma_{abs} + \sigma_{inc}$$

And so the beam width and sample dimensions are changed as required to allow for a good estimation of the attenuation cross-section [r6].

2.1.3.7 *Static Approximation of Differential Cross Section (Placzek Correction)*

The differential cross section is produced directly from the scattering of the sample. The diffraction experiment produces instantaneous views of the structure at the moment of the detection event. Therefore inelastic scattering events cannot be ignored but must be corrected due to the application of the static approximation to the coherent differential cross section. The static approximation for the total differential cross section applies to the small energy difference between the incident and scattered X-ray or neutron. The correction is applied to the data that digresses from the static approximation and so it is assumed that the corrected data is produced from elastic scattering [r6].

2.2 Computational modelling

2.2.1 Interatomic potentials

Interatomic potentials describe the interactions between the atoms [r13]. Mathematically, the short-range interatomic potentials such as Lennard Jones potentials can be calculated using

Equation 2.38
$$U_{ij} = \frac{A}{r_{ij}^{12}} - \frac{B}{r_{ij}^6}$$

Where U_{ij} is the potential, r_{ij} is the separation of the ions i and j and A and B are variable potential parameters.

The term in r^{-12} is a repulsive term which is caused by the Pauli exclusion principle. The attractive term $-\frac{B}{r_{ij}^6}$ is a Van der Waals term that considers the dipole-dipole interactions.

The long-range interactions between charged ions such as O^{2-} and Si^{4+} are known as Coulomb interactions, and can be calculated by using the Coulomb equation

Equation 2.39
$$E_{Coulomb} = \frac{e^2}{4\pi\epsilon_0} \sum_{ij} \frac{q_i q_j}{r_{ij}}$$

Where e is the charge of an electron, ϵ_0 is the permittivity of free space, q is the charge on an ion, and r_{ij} is the distance between the ions i and j . Calculating the long range interactions can be made less computationally expensive by using the Ewald summation method [r13].

The total potential energy of the system is

Equation 2.40
$$U = \frac{1}{2} \sum_i \sum_{j \neq i} U_{\alpha(i)\alpha(j)}(r_{ij})$$

The summation in equation 2.40 proceeds over all atom pairs in the system, and the factor of $\frac{1}{2}$ is needed to prevent double counting of atom pairs.

2.2.2 Monte Carlo modelling

In a standard Monte Carlo simulation [r13] the acceptance of a move is based on the usual Metropolis condition, namely if the change in the potential energy of the system as a result of the move,

Equation 2.41
$$\Delta U = U_{after} - U_{before}$$

is less than zero the move is always accepted, and if it is greater than zero, the move is accepted with probability

Equation 2.42
$$P(\Delta U) = \exp\left[-\frac{\Delta U}{kT}\right]$$

This simple procedure ensures the system proceeds along a Markov chain and over a period of time visits a large volume of the available phase space.

2.2.3 Empirical Potential Structure Refinement (EPSR)

The potential energy in EPSR [r14] consists of two primary terms, the reference potential energy, U_{Ref} , and the empirical potential (EP) energy, U_{Ep} . U_{Ref} takes on a standard form, i.e. Lennard Jones as described above, and the potential parameters may be available from the literature. U_{Ep} on the other hand does not take any standard form and, once the simulation with the reference potential alone has come to equilibrium, the EP is used to guide the atomic and molecular moves in directions that give the closest representation of the diffraction data.

The method that appears to be most successful for generating the empirical potential (EP) is in the form of a series of power exponential functions:-

$$U^{(EP)}(r) = kT \sum_i C_i p_{n_i}(r, \sigma_r)$$

Equation 2.43

where

$$p_n(r, \sigma) = \frac{1}{4\pi\rho\sigma^3(n+2)!} \left(\frac{r}{\sigma}\right)^n \exp\left[-\frac{r}{\sigma}\right]$$

Equation 2.44

the C_i are real, but can be positive or negative, and σ_r is a width function to be set by the user. The total atomic number density of the simulated system is ρ .

At the beginning of the m^{th} iteration of the algorithm each distinct pair of atoms, j , will have a set of coefficients, $C_{k,m}^{(j)}$, which are used to form the empirical potential for that atom pair. Following equation 2.43 the EP at the beginning of the m^{th} iteration for any particular pair of atoms, j , is determined from

$$U_m^{(j)}(r) = kT \sum_k C_{k,m}^{(j)} p_{n_k}(r, \sigma_r)$$

Equation 2.45

(At the outset, with $m = 0$, the coefficients $C_{k,m}^{(j)}$ are set to zero.)

The fit to the i^{th} dataset of a particular experiment can be represented by a weighted sum over all the pairs of atom types of the relevant simulated partial structure factors $S_{\alpha\beta}(Q)$:

$$F_i(Q) = \sum_{j=1,N} w_{ij} S_j(Q)$$

Equation 2.46

After the m^{th} iteration the differences between data and fit, i.e. $(D_i(Q) - F_i(Q))$, are calculated. In EPSR, the coefficients C_i are estimated directly from the difference in diffraction data by fitting a series of the form

$$U_{EP}(Q) = \sum_i C_i P_{n_i}(Q, \sigma_Q)$$

Equation 2.47

to the difference data in Q -space. This is possible because the function $p_n(r, \sigma)$ has an exact 3-dimensional Fourier transform to Q -space

$$P_n(Q, \sigma) = 4\pi\rho \int p_n(r) \exp(i\mathbf{Q} \cdot \mathbf{r}) d\mathbf{r}$$

$$= \frac{1}{(n+2) \left(\sqrt{1+Q^2\sigma^2} \right)^{n+4}} \left[2 \cos(n\alpha) + \frac{(1-Q^2\sigma^2)}{Q\sigma} \sin(n\alpha) \right]$$

Equation 2.48

where $\alpha = \arctan(Q\sigma)$.

This gives rise to a set of difference coefficients, $C_k^{(i)}$, one for each supplied dataset, which change as the simulation proceeds. These difference coefficients are then accumulated in the empirical potential coefficients for the $(m+1)^{\text{th}}$ iteration.

$$C_{k,m+1}^{(j)} = C_{k,m}^{(j)} + \sum_{i=1,M} w_{ji}^{-1} C_k^{(i)}$$

Equation 2.49

Ideally the difference coefficients should go to zero when the simulation approaches the data closely. Once the EP has stopped changing, or the absolute energy of the EP has reached its specified limit, the simulation can be used to extract ensemble averages of required quantities.

3. Methods

3.1 Experimental Methods

3.1.1 Synthesis

Within this study, the majority of sample preparations will utilise a vacuum filtration system. This method involves the addition of two or more solutions being added to a reaction vessel, at which time a precipitation reaction occurs and the resultant wet precipitate is then filtered off under vacuum. The precipitate is then washed and dried, with flowing air, before it is ready for analysis.



Figure 3.1 - Example setup of a vacuum filtration system. Image courtesy of J.D. Rodriguez-Blanco.

A typical procedure like this takes approximately 2-3 minutes and yields 0.1g of material (approximately, depending on which material) which was then stored in glass vials ready for experimentation.



Figure 3.2 - Glass vial containing prepared amorphous sample.

In contrast, one subsection of this work will comprise of ball-milling a crystallised commercial reagent in order to 'break up' these crystals and produce an amorphous product.

Ball-milling is a technique that involves grinding or "milling" a sample. The grinding action is achieved by impact of hardened balls against the powdered sample within the mill.

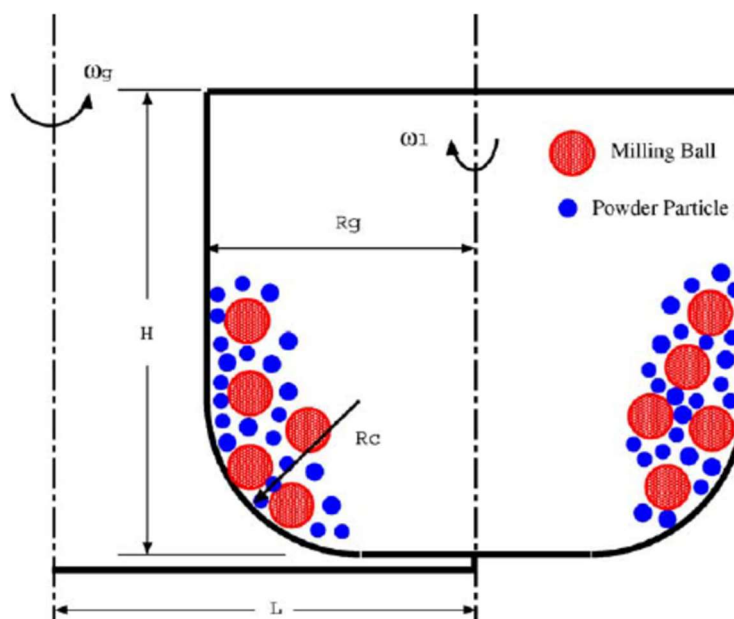


Figure 3.3 - Example cross-section of a ball-mill. The hollow cylinder of the mill is rotated around the ω_1 axis.^[79]

A ball mill consists of a hollow cylindrical shell rotating about its axis. The axis of the shell may be either horizontal or at a small angle to the horizontal. It is partially filled with grinding media in the form of balls (red spheres in figure 3.3). For this work a cylinder and balls made of yttria stabilised zirconia were used. The length of the mill is approximately equal to its diameter.

More specific details will follow within the relevant results chapters.

3.1.2 Lab-based Characterisation

3.1.2.1 XRD

X-ray powder diffraction (XRD) is a rapid analytical technique primarily used for phase identification of a crystalline material and can provide information on unit cell dimensions. In 1912, it was discovered by Max von Laue that a crystalline substance acts a diffraction grating (within three-dimensional space) for x-ray wavelengths similar to the planes of the crystal lattice.

Over the following century XRD equipment has been developed with increasing sensitivity and scope. As mentioned previously, one of the most common uses for XRD is the identification of unknown crystalline materials. Determination of unknown solids is critical to studies in geology, environmental science, material science, engineering and biology.

Applications include (but not limited to):

- characterization of crystalline materials
- identification of fine-grained minerals such as clays and mixed layer clays that are difficult to determine optically
- determination of unit cell dimensions
- measurement of sample purity

With specialized techniques, XRD can be used to:

- determine crystal structures using Rietveld refinement
- determine of modal amounts of minerals (quantitative analysis)

The majority of laboratory based x-ray diffraction methods are based on the generation of x-rays in a cathode ray tube (figure 3.4). Within the cathode ray tube, a filament is heated to produce electrons, these electrons are then accelerated towards the target material (which can be copper, iron, silver) by applying a voltage. The target material is bombarded with electrons and when they have sufficient energy, they will excite and dislodge inner shell electrons from the target material, this excitement causes the production of x-rays. These x-rays are filtered through a monochromator to produce monochromatic x-rays which are then directed at the sample of study (placed in a sample holder), passing through the sample and are diffracted. These diffracted x-rays are recorded by an x-ray detector. A key component is the angle between the incident and diffracted rays.

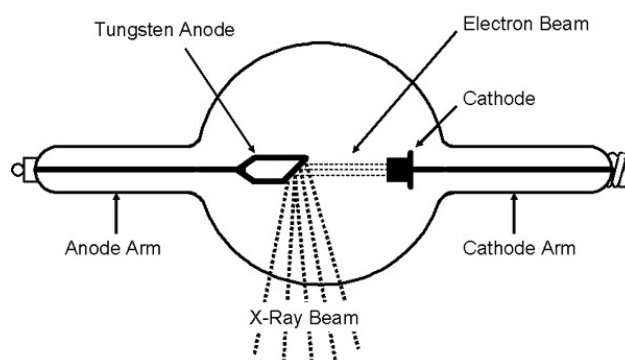


Figure 3.4 - Schematic of a typical cathode ray tube.^[80]

The geometry of older XRD instruments has the x-ray beam at an angle θ to the sample of study, while the x-ray detector is mounted on an arm to collect the diffracted x-rays, this rotates at an angle of 2θ . The angle and rotation of the sample is maintained by a component termed a goniometer. For typical scans, data is collected at 2θ from $\sim 5^\circ$ to 70° . Current XRD instruments operate on a θ/θ orientation, this means that both the x-ray source and detector are mounted on arms that rotate at θ/θ angles.

The purpose of collecting diffracted x-rays over a range of 2θ is in order to satisfy the Bragg equation (defined below in equation 3.1).

Equation 3.1
$$n \cdot \lambda = 2 \cdot d \cdot \sin\theta$$

This law relates the wavelength (λ) of electromagnetic radiation, determined from the target material in the cathode tube, and the order of reflection (n) to the diffraction angle (θ) and the lattice spacing in a crystalline sample (d). By scanning the sample through a range of 2θ , all possible diffraction directions of the lattice should be attained due to the random orientation of the powdered material. Conversion of the diffraction peaks to d -spacings allows identification of the mineral because each mineral has a set of unique d -spacings. However, should the sample of study be amorphous and thus, have no lattice then no diffraction peaks will appear. This is illustrated in figures 3.5

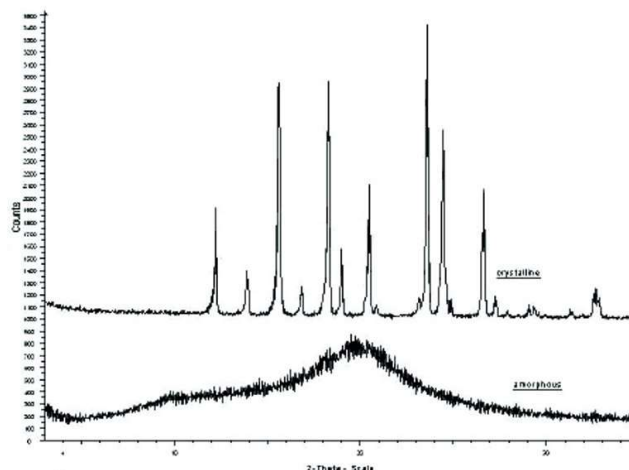


Figure 3.5 - XRD diffraction pattern of; crystalline material (top) showing well defined peaks and amorphous material (bottom) showing a very broad diffraction pattern.^[81]

3.1.2.2 TGA-DSC

Thermal analysis is a branch of materials science where the properties of materials are studied as they change with temperature. First developed in 1962 by E.S. Watson and M.J. O'Neill, several methods are now commonly used – these are distinguished from one another by the property which is measured, below is a list of techniques used in the present work:

- Thermogravimetric analysis (TGA): mass
- Differential thermal analysis (DTA): temperature difference
- Differential scanning calorimetry (DSC): heat difference

For this work, TGA-DSC will be used primarily to determine the composition of the amorphous material being studied but secondly to try and give an indication of possible heat-treatment temperatures.

Thermogravimetric analysis (TGA) is commonly used to determine selected characteristics of materials that exhibit either mass loss or gain due to decomposition, oxidation, or loss of volatiles (such as moisture). Common applications of TGA are

- Materials characterization through analysis of characteristic decomposition patterns
- Studies of degradation mechanisms and reaction kinetics
- Determination of organic content in a sample
- Determination of inorganic (e.g. ash) content in a sample

This may be useful for corroborating predicted material structures or simply used as a chemical analysis to study the effects of temperature/time on a sample of study.

Differential thermal analysis (DTA) is a method of thermal analysis which measures the physical and chemical properties that change within a sample materials. These measurements can either be as a function of increasing temperature, or as a function of time.^[82] Physical properties, such as second-order phase transitions, including vaporization, and desorption can be studied using DTA analysis. DTA can provide information about chemical phenomena like chemisorptions, desolvation (especially dehydration) and decomposition.^[82]

Differential scanning calorimetry (DSC) is a thermoanalytical technique in which the amount of energy (in the form of heat) is required to increase the temperature of a sample of study is compared against a reference as a function of temperature. Both the sample and reference are maintained at nearly the same temperature throughout the experiment. This can give an indication of how chemically stable a sample is or at what temperature the sample begins to degrade.

Example TGA-DSC measurements are shown below to indicate desorption and crystallisation

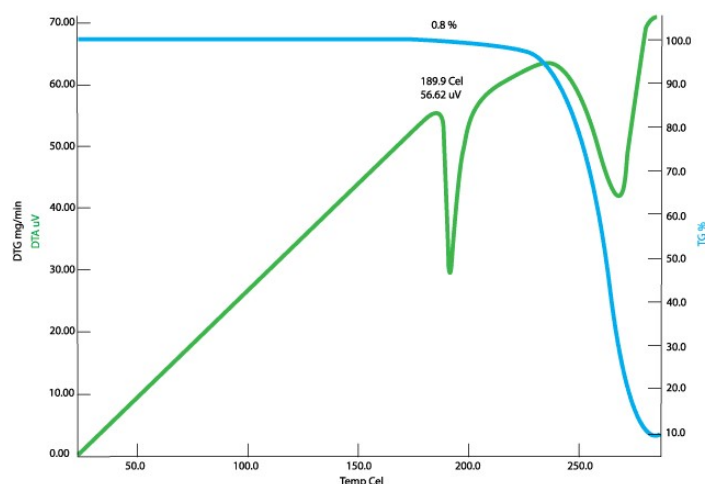


Figure 3.6 - A typical TGA-DSC experiment, the TGA (green) shows a crystallisation 'peak' at just below 200°C and the DSC (blue) shows 0.8% loss due to dehydration until approximately 250°C which could be related to crystallisation processes.^[83]

3.1.2.3 He-Pycnometry

A helium (He) pycnometer (also known as a gas pycnometer) is a laboratory device which measures the density of a solid. The solid can be regularly shaped, porous or non-porous, monolithic, powdered or granular. The He-pycnometer employs a method of gas displacement and the volume-pressure relationship of a gas, known as Boyle's Law.

Boyle's law is an experimental gas law, named after chemist and physicist Robert Boyle, who published the original law in 1662.^[84] that describes the pressure of a gas and how it tends to increase as the volume of a gas decreases. A modern statement of Boyle's law is:

"The absolute pressure exerted by a given mass of an ideal gas is inversely proportional to the volume it occupies if the temperature and amount of gas remain unchanged within a closed system."^[85]

Mathematically, Boyle's law can be stated as below in equations 3.2 and 3.3

Equation 3.2
$$P \propto 1/V$$

Equation 3.3
$$P.V = k$$

where P is the pressure of the gas, V is the volume of the gas, and k is a constant. This constant, k , is the product of pressure and temperature for a given mass, so long as temperature is a constant. To compare the same substance under two different sets of conditions, equation 3.3 can be expanded to give the following:

Equation 3.4
$$P_1 \cdot V_1 = P_2 \cdot V_2$$

In equation 3.4 it shows that, as the volume of gas increases, the pressure decreases proportionally. Conversely, as volume decreases, the pressure of the gas increases. The relationship in equation 3.4 can be exploited to form the basis of He-pycnometry below in equation 3.5 and how that equation relates to a schematic of a He-pycnometer in figure 3.7.

Equation 3.5
$$V_s = V_c + \frac{V_r}{\left(1 - \frac{P_1}{P_2}\right)}$$

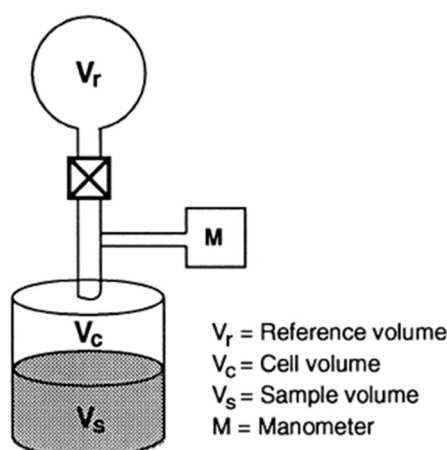


Figure 3.7 - Schematic of a He-pycnometer.^[86]

Where; V_s - the sample volume, V_c - the volume of the empty sample chamber (determined in the instrument calibration), V_r - the volume of the reference volume (from calibration), P_1 is the first pressure (the empty sample chamber) and P_2 is the second (lower) pressure after the gas has filled the combined volumes of sample chamber and reference chamber (with sample present). By comparing V_s and V_c then it is possible to determine the density of the sample as the amount of gas within the cell volume cannot displace the volume of the sample, thus it can be calculated how much sample is present within this volume giving the density of the sample.

Equation 3.6
$$\rho_s = m_s / V_s$$

Prior to a pycnometry measurement, the mass of the sample material is recorded (m_s) and thus the density (ρ_s) can be calculated using equation 3.6 above.

3.1.2.4 FTIR

Fourier transform infra-red spectroscopy (FTIR) is a laboratory-based technique used to obtain an infra-red (IR) spectrum of absorption/emission of a solid, liquid or gas. An FTIR spectrometer collects high spectral resolution data over a wide spectral range simultaneously. This is a significant

advantage over a dispersive spectrometer which measures intensity over a narrow range of wavelengths at a time.

The term Fourier transform infra-red spectroscopy originates from the mathematical process (Fourier transform) that converts the raw data into the actual spectrum.

FTIR spectrometers predominantly take measurements in the mid and near IR regions of the electromagnetic spectrum, illustrated below in figure 3.8.

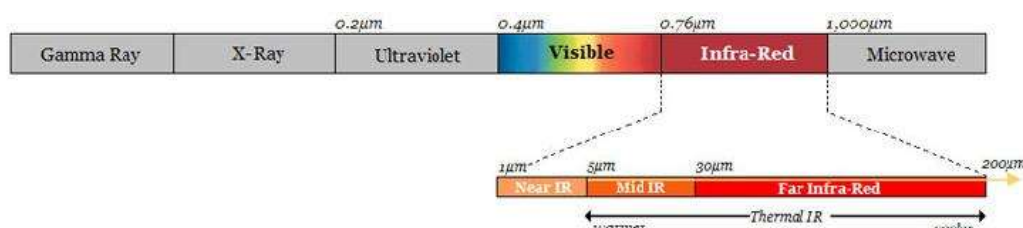


Figure 3.8 - The electromagnetic spectrum, with the infra-red highlighted between 0.76µm and 1000µm. FTIR instruments usually collect spectra in the near IR (1µm to 5µm) and mid IR (5µm to 30µm).^[87]

A typical FTIR is made up of the 4 following components:

- **IR source**
The most common source is a silicon carbide element which is heated to approximately 1100K to 1200K.
- **Monochromator**
The purpose of a monochromator is to separate and transmit only a limited portion of the optical spectrum towards the sample. This enables the user to use only a limited bandwidth of light. This is of benefit as it increases the sensitivity of the measurement and reduces the response time as the FTIR does not need to cycle through all the IR wavelengths on the sample.
- **Beam splitter**
A beam splitter's purpose is to split the IR light in two, with one portion of light travelling through the sample and the other portion travelling straight to the detector (via a series of mirrors). For the mid-IR region, the beam splitter is usually comprised of potassium bromide (KBr) but can sometimes be made of sodium chloride (NaCl).
- **Detector**
Spectrometers measuring mid-IR wavelengths use pyroelectric detectors. These detectors respond to changes in temperature at varying intensity of IR radiation. The elements within the detectors are either deuterated triglycine sulfate (DTGS) or lithium tantalate (LiTaO₃). Both DTGS and lithium tantalate detectors operate at ambient temperatures and typically a scan takes just few seconds. Should the user require higher sensitivity or faster response then cooled photoelectric detectors can be employed. Liquid nitrogen cooled mercury cadmium telluride (MCT) detectors are widely used for high sensitivity and fast response (approximately 10ms) in the mid-IR.

How these components are generally arranged within and FTIR are shown in figure 3.9.

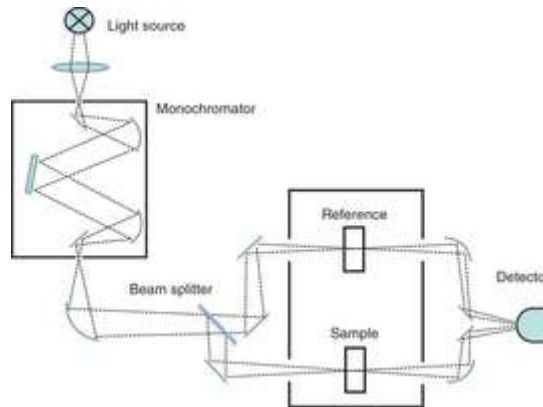


Figure 3.9 - Schematic of a typical FTIR spectrometer.^[88]

3.1.2.5 XRF

Following similar principles to XRD (discussed in section 3.1.2.1), when an x-ray strikes a sample from an x-ray tube in addition to it being scattered through the material, it can be absorbed by the a constituent atom. The process that governs this absorption of an x-ray is that all of the energy from the x-ray is transferred to an innermost electron of an atom, this is called the "photoelectric effect". Should the x-ray have transferred sufficient energy to the electron, it can be ejected from its stable energy level (known as the ground state) to a higher energy level. This excitation creates a vacancy at the lower energy level and is an unstable condition for the atom. After a time, the excited electron will 'fall' back down to it is more stable energy level (known as relaxation). When this happens, radiation is emitted from the atom, characteristic of the particular energy level and electron involved. As each element has a unique set of energy levels, each element produces a unique set of energies when excited.

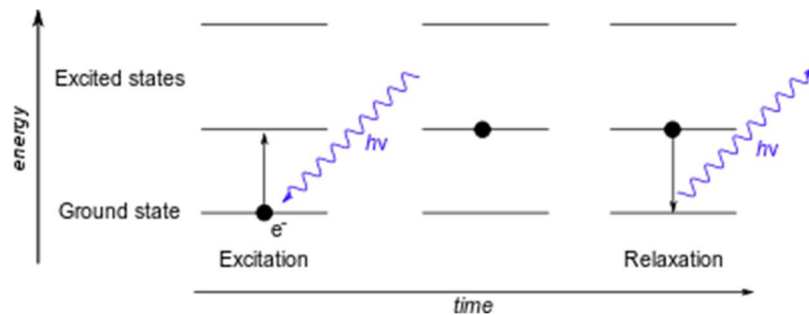


Figure 3.10 - Diagram to show how excitation and relaxation occurs in electron energy levels.^[89]

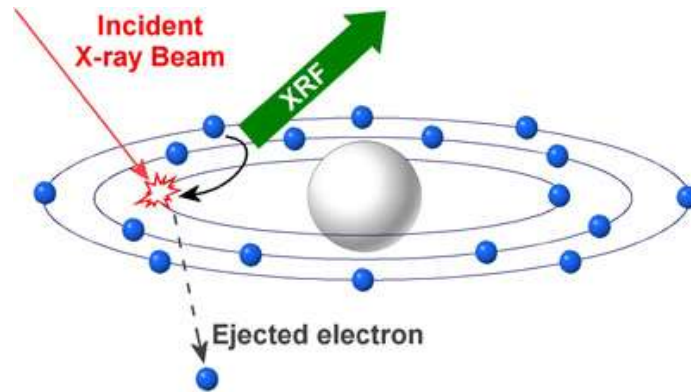


Figure 3.11 - Graphical representation of the x-ray fluorescence (XRF) process, showing the incident x-ray beam dislodging an electron and producing fluorescence.^[90]

These unique energies for each atom allows one to non-destructively measure the elemental composition of a sample, these emissions are called x-ray fluorescence (XRF). A measurement is typically done with a solid state detector, these are most commonly silicon PIN diode (Si-PIN), silicon drift detectors (SDD) or cadmium telluride (CdTe). In most cases the innermost K and L shells of electrons (illustrated below in figure 3.12) are involved in XRF detection. A typical x-ray spectrum from an irradiated sample will display multiple peaks of different intensities once the signals are processed through a digital pulse processor.

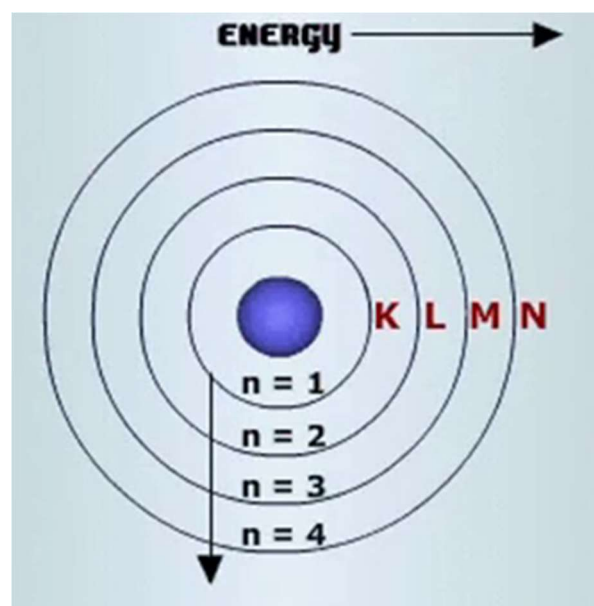


Figure 3.12 - Graphical representation of electron shells, primarily K and L shell electrons are involved in XRF.^[91]

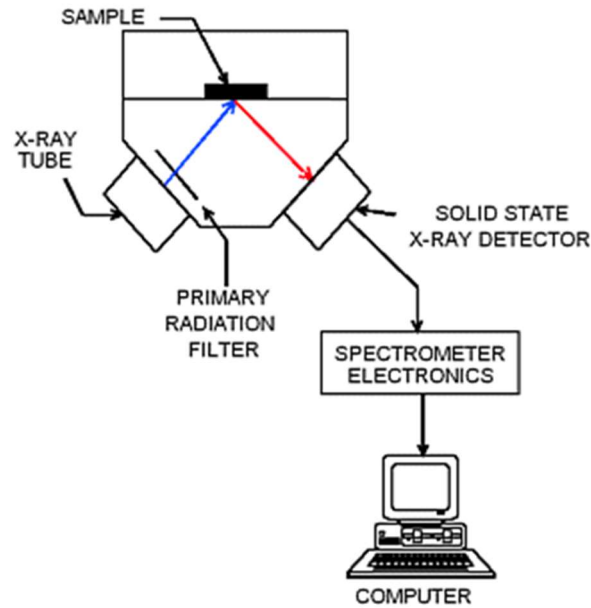


Figure 3.13 - Schematic of a typical XRF process.^[92]

At the end of the XRF process, the user will be presented with an elemental composition of the studied sample.

3.1.3 Central Facility Experiments

3.1.3.1 XRD

The principles of central facilities x-ray diffraction experiments are essentially the same as the laboratory based XRD (detailed in 3.1.2.1) but with x-rays of higher energies, which are generated using facilities known as synchrotrons.

A synchrotron is a type of circular particle accelerator. A circular particle accelerator works by accelerating charged particles (electrons) through sequences of magnets arranged in a circular 'ring'. The particles are accelerated to almost the speed of light, as the particles approach the speed of light they begin to produce light. The faster the particles move, the brighter the light - this is called synchrotron light and is predominantly in the x-ray region of the electromagnetic spectrum. Typically this synchrotron light is millions of times brighter than light produced from conventional sources and 10 billion times brighter than the Sun. This means that the brighter the light, the more energy the x-rays have and this leads to higher levels of sensitivity than laboratory based XRD.

The UK has an x-ray synchrotron in near Oxford and it is called Diamond Light Source and it operates with electrons travelling at approximately 3GeV.

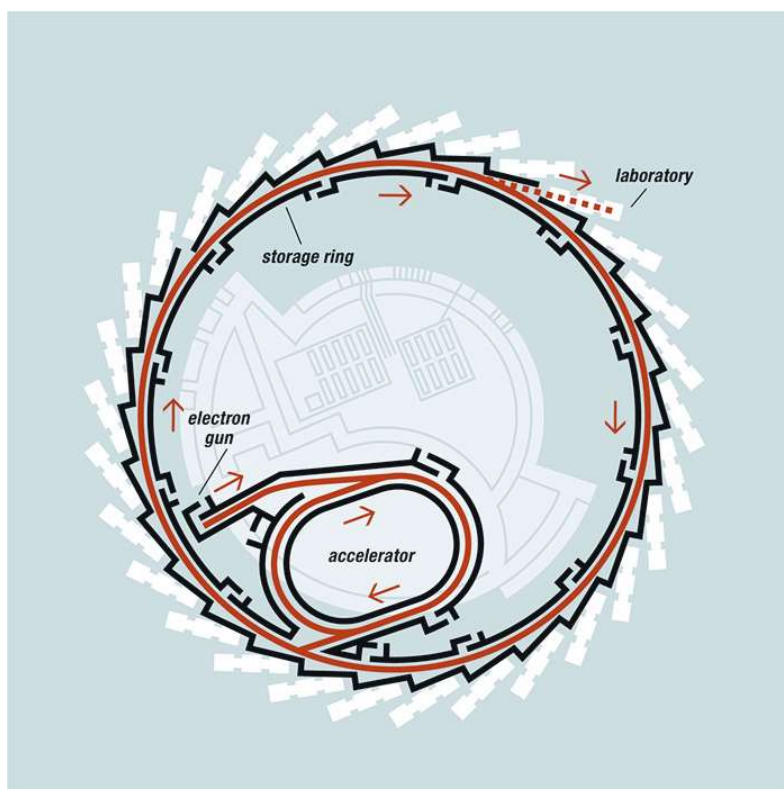


Figure 3.13 - Schematic of Diamond Light Source, UK. The path of the accelerated particles is shown in red with the white "beamlines" positioned off the storage ring.^[93]

There are synchrotrons around the world with a few being; ESRF in France, DESY in Germany, Elettra in Italy and Argonne National Laboratory in USA.

In terms of operation, synchrotron XRD and laboratory-based XRD are fairly similar as they are both governed by the Bragg equation (equation 3.1 detailed in 3.1.2.1). Typically the sample of study is placed in the x-ray beam and detectors are placed at angles of 2θ (either with fixed detectors or on a rotating arm).



Figure 3.14 - XRD beamline at the Elettra synchrotron in Italy, x-rays approach along the red line's path before hitting the sample and being scattered. Scattered x-rays are recorded using the detector mounted on the rotating arm.

The most important difference is the energy of the x-rays produced. With the greater energies involved in synchrotron experiments this results in an increased resolution of the scattering pattern. This is particularly beneficial for studying amorphous materials as in the laboratory, a typical amorphous XRD pattern is rather broad (see figure 3.5) but with synchrotron x-rays, the short range order can be investigated in greater detail. One trade-off of the greater resolution is an increase in collection time - laboratory XRD is approximately 4 hours for one sample, synchrotron XRD is around 24 hours (depending on the specific sample).

3.1.3.2 EXAFS

Another use for synchrotron x-rays are to study x-ray absorption of a material. This is conducted in two ways:

- EXAFS (Extended X-ray Absorption Fine Structure)
- XANES/NEXAFS (X-Ray Absorption Near Edge Structure/Near Edge X-ray Absorption Fine Structure)

Both are regions of the spectrum obtained from XAS (X-ray Absorption Spectroscopy). EXAFS corresponds to the oscillating part of the spectrum at higher energies above the absorption edge (appearing as a sudden, sharp peak), starting at roughly 50 eV and extending to about 1000 eV above the edge (shown in Figure 3.15). Through mathematical analysis of this region, one can obtain local structural information for the atom in question.

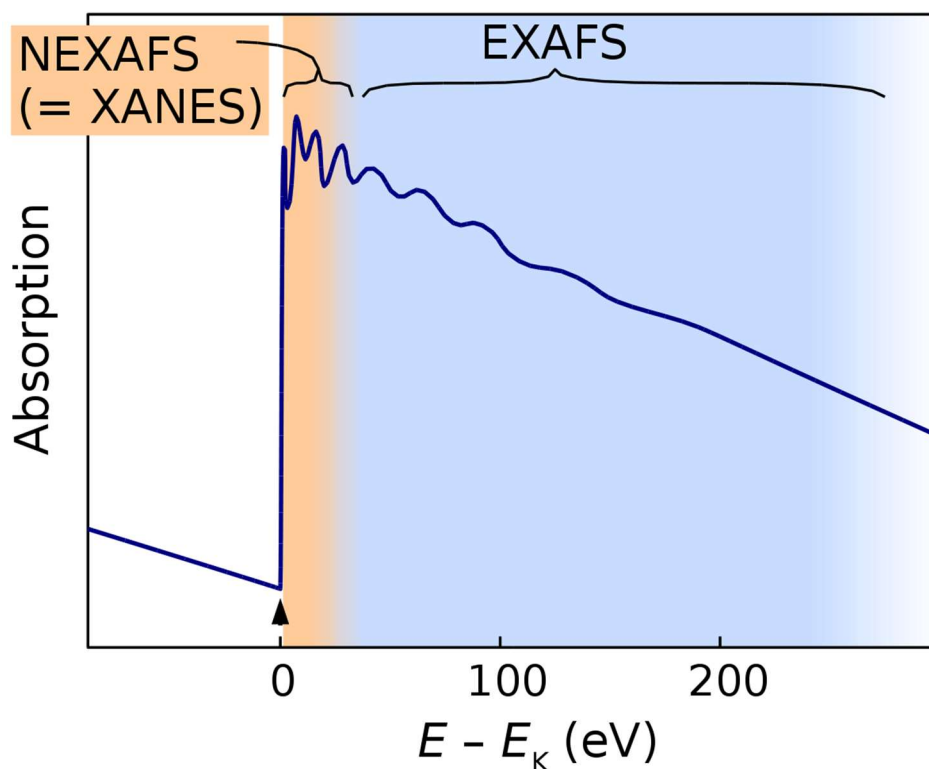


Figure 3.15 - Diagram to show the EXAFS (Extended X-ray Absorption Fine Structure) and XANES (X-Ray Absorption Near Edge structure) regions.^[94]

Similarly to XRF (section 3.1.3.5), XAS involves a process in which an x-ray beam is applied to an atom and causes the ejection of an electron, usually a core electron. The ejection of this core electron leaves a vacancy in the core shell, and an outer electron relaxes to fill that vacancy. This phenomenon is only observed when the energy of the x-ray exceeds the ionization energy (the energy required to eject an electron from its shell) of the electrons in that shell.

The basis of EXAFS theory is related to the x-ray absorption coefficient. The x-ray absorption coefficient, μ , describes the relationship between the x-ray beam intensity going into a sample material and the x-ray intensity leaving the sample after travelling a distance (known as x) within the sample. The absorption coefficient is described mathematically as:

Equation 3.6
$$\mu = - \frac{d(\ln I)}{dx}$$

In equation 3.6, dx is the distance travelled by the x-ray beam through the sample, and I is the intensity of the x-ray beam. In a typical EXAFS spectrum, such as that in figure 3.15, when energy (usually in eV) is plotted against absorbance then various sharp peaks will be observed. These peaks (known as edges), which vary by atom, correspond to the ionization of a core orbital, K-edges describing the excitation of the innermost 1s electron, and L-edges and M-edges referring to the same for higher energy orbitals. These edges correlate to the K, L and M shells discussed in section 3.1.3.5 and displayed in figure 3.12.

After each edge, a series of downward oscillations will be observed. Wave interactions between the ejected electron and the surrounding electrons in the absorbing atom are the cause of these oscillations. Some of these waves are 'backscattered' by neighbouring atoms (known as backscattering atoms) when the emitted waves from the absorbing atom hit neighbouring atoms and change paths, returning to the absorbing atom. When these waves interfere constructively, they form a maxima in the oscillations, whereas minima result from destructive interference. All these oscillations are characteristic of the atoms surrounding the absorbing atom and their corresponding distance from each other. A graphical representation of how these oscillations result in the EXAFS plot is shown below in figure 3.16.

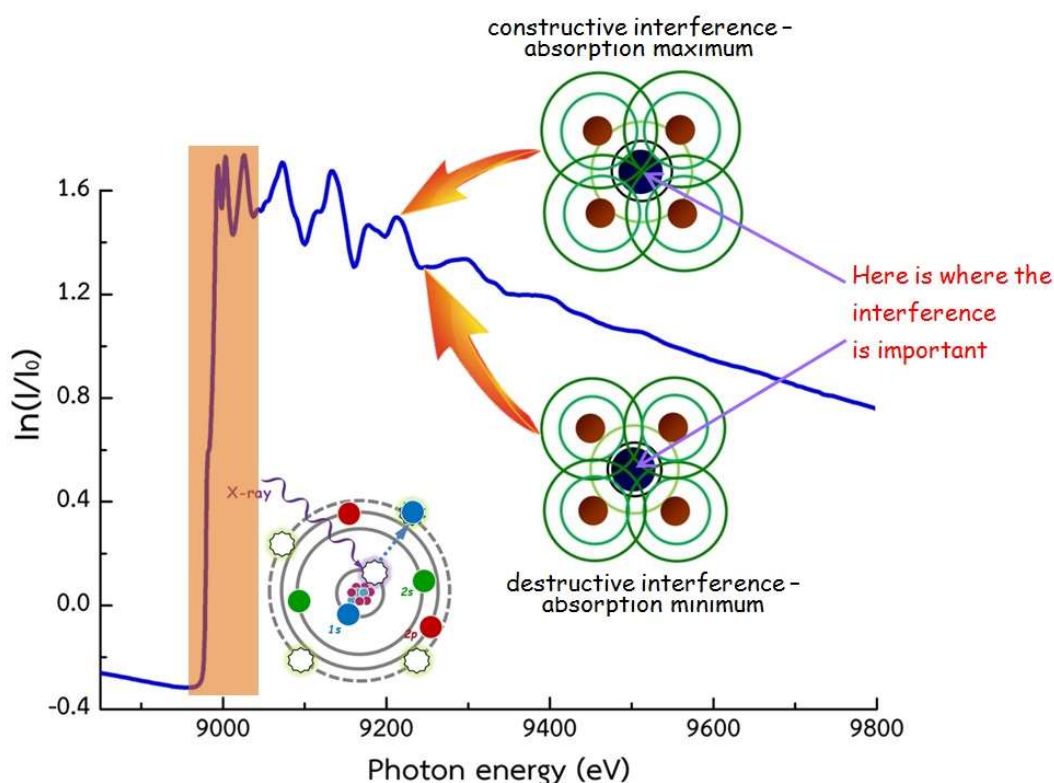


Figure 3.16 - Graphical representation of how constructive and destructive interference correspond to EXAFS plot.^[95]

3.1.3.3 Neutron Scattering

A complimentary central facility technique to XRD and EXAFS is neutron scattering (also known as neutron diffraction).

Neutrons are neutrally charged sub-atomic particles which means they are not affected by charge-charge interactions like protons (positive charge) and electrons (negative charge). This neutrality enables neutron to penetrate deeper into the atomic and/or magnetic structure of a material.

The material to be examined is placed in a beam of thermal neutrons to obtain a diffraction pattern that provides information of the structure of the material. The technique is similar to synchrotron XRD but due to the different scattering properties of neutrons and x-rays, complimentary information can be obtained. Neutron diffraction has some unique characteristics when compared to other types of radiation. This makes it very useful for the study of the atomic structure of liquids, amorphous materials and crystalline materials.

Diffraction using neutrons can see the ordered part of material samples; for ordered systems (crystals) - their overall crystal structure but also defects and deviations from the crystal order; for disordered systems - the ordered portions (usually short-range) existing amid this overall disorder.

Methods of diffraction can be divided into two interactions:

- Nuclear diffraction - Diffraction due to the interaction between neutrons and atomic nuclei.
- Magnetic diffraction - Diffraction due to the interaction between the magnetic moments of neutrons and magnetic moments of atoms.

The UK has a neutron facility in Oxford, UK called the ISIS Neutron Source Facility. It is situated near the Diamond Light Source.

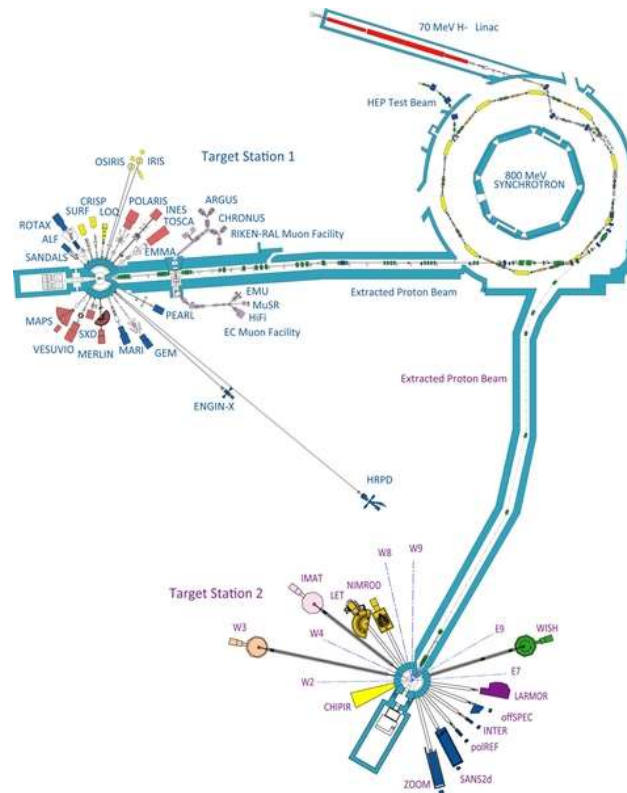


Figure 3.17 - Schematic of the ISIS neutron facility in Oxford, UK. The beamlines are located around two target stations for the synchrotron ring.^[96]

The measurement principle of neutron diffraction is based on the Bragg Equation, like that of XRD (discussed in 3.1.2.1 using equation 3.1). Neutrons are generated in a similar fashion to x-ray generation in synchrotron. Protons are accelerated (at 84% the speed of light at ISIS) around a synchrotron ring but, unlike x-ray generation, the protons are fired at a solid target, typically tungsten, and this collision releases neutrons. These neutrons are then directed at beamline instruments such as SANDALS (which stands for Small ANgle Diffraction of Amorphous Liquids and Solids) and NIMROD (Near and Intermediate Range Order Diffractometer).

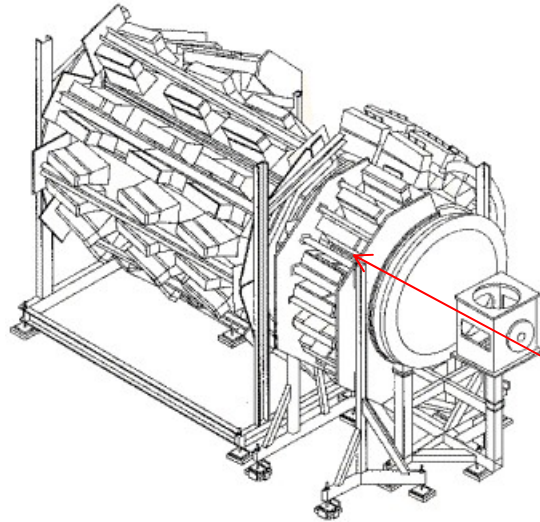


Figure 3.18 - Schematic of the SANDALS diffractometer where neutrons enter via the red pathway into the sample and are then diffracted. These diffracted neutrons are recorded using angle-mounted detectors past the sample.^[97]

After diffracted neutrons are recorded the subsequent counts can be mathematically analysed to generate real-space data for the atomistic structure of the sample material. This is done by using the recorded data and producing a quantity known as a structure factor or $S(Q)$. The structure factor is a mathematical representation of how a material and its constituent atoms diffract radiation (in this case neutrons) and is represented thus:

Equation 3.7
$$S(Q) = \frac{1}{\sum_{j=1}^N f_j^2} \cdot \sum_{j=1}^N \sum_{k=1}^N f_j f_k e^{-iq(R_j - R_k)}$$

The structure factor is equation 3.7 shows how for a neutron beam of wavelength λ with N atoms at stationary positions f_j , $j = 1, \dots, N$ illustrates the positions of atoms within the sample material.^[98-100]

The generated structure factor can be computationally modelled to extract specific atom positions and interactions.

3.2 *Computational Methods*

3.2.1 *GHEMICAL*

In order to create input files for computational modelling, the software package GHEMICAL was used to create and save atom files (.ato) for specific molecular ions, ie. CO_3^{2-} and PO_4^{3-} rather than having individual C and O atoms incorporated into the computational model. Tethering these atoms to their subsequent groups would greatly reducing computational workload.

GHEMICAL is computational chemistry package which can perform a number of varied tasks but for this work, the following features were utilised:

- Options for studying a molecular system using :
 - Geometry Optimization.
- File import/export features provided by OpenBabel.
- OpenGL graphics presentations :
 - molecular graphics presentations :
 - Ball-And-Stick.
 - Wireframe.
 - molecular editing tools :
 - add and remove atoms and bonds.
 - add or remove Hydrogens automatically.
 - measurement tools for measuring :
 - distances.
 - angles.
 - torsions.
 - visualization options :
 - coloured planes.
 - coloured surfaces.
 - volume rendering.

In addition to all these features, GHEMICAL has a very useful graphical user interface (GUI).

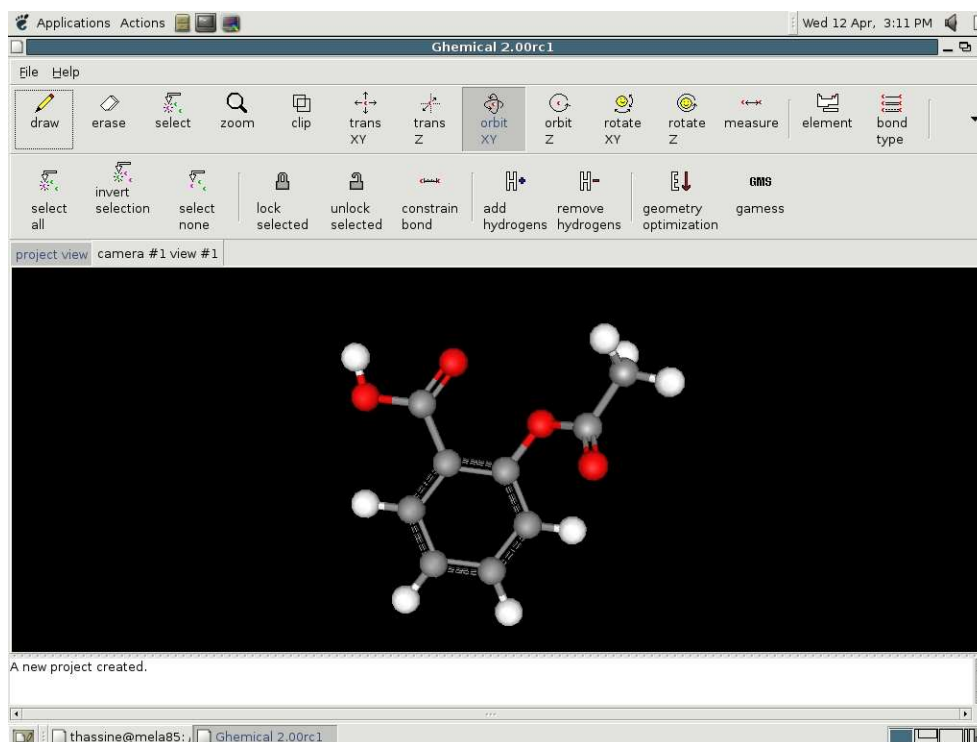


Figure 3.18 - The graphical user interface (GUI) of the GHEMICAL software package with an example molecule.

3.2.2 GUDRUN

In order to work with the data gathered from central facilities experiments, it was necessary to perform reduction on the raw data gathered. To analyse neutron data, a specific and tailored software package was needed, this is called GUDRUN-N. This program was developed by the Disordered Materials Group at ISIS.^[101]

GUDRUN-N has an on-board GUI which aids the full correction of neutron data from SANDALS (the beamline to be used at the ISIS neutron facility). The corrections performed by GUDRUN are as follows:

- Detector dead-time - for a short period of time (typically a few microseconds) after a neutron event, the detector is 'dead'. The amount of time a detector is dead varies depending on the detector type. This dead time can be measured directly by an encoder within the detector used to detect events.
- Normalisation to the incident beam monitor - the incident neutron beam is recorded for each experiment to remove variations due to fluctuations in the proton beam. The incident beam is counted by placing a monitor before the beam hits the sample, this recorded incident beam is then divided out of the raw data.
- Background subtraction - for each experiment, the scattering from an empty sample holder and the empty instrument are sampled. These measurements constitute the background scattering, this is then removed during the data analysis.
- Vanadium standard calibration - a vanadium standard is used to calibrate the differential cross section. Vanadium is used in particular because it has a known density and it can be formed into plates or cylinders of high purity. It is important that the vanadium standard is measured under the same beam conditions as the sample.

- Inelastic scattering - the two ways that neutrons scatter are elastically and inelastically. Typically, for nuclei of greater mass than a neutron, the correction for inelastic scattering is very small.^[102] The biggest culprit for inelastic scattering from a sample is the presence of hydrogen (due to hydrogen's similar mass to a neutron)

Alongside the above corrections, the composition and density of the sample material are required to generate an output data file. Below in figure 3.19 is a screenshot of GUDRUN on the sample page.

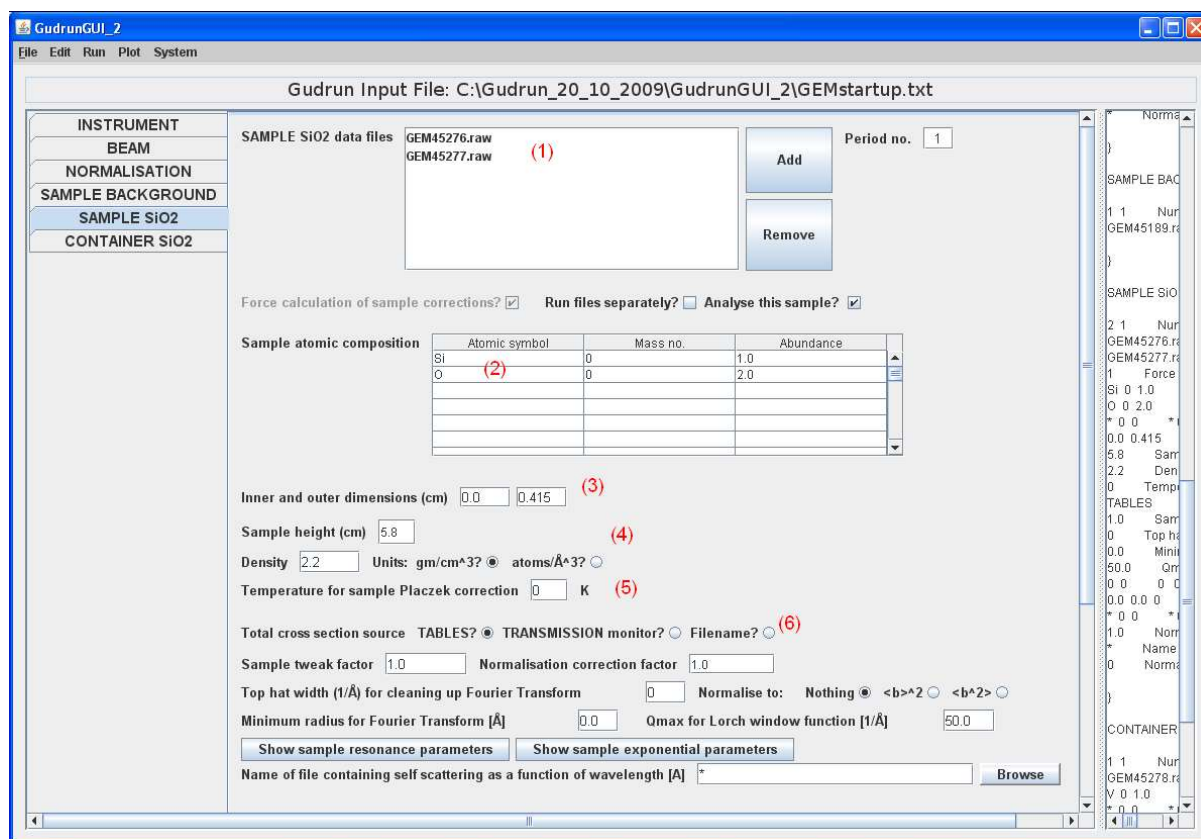


Figure 3.19 - Screenshot of the GUDRUN GUI for a sample of SiO₂. (1) is where the raw data files are added, (2) the composition of the sample, (3) width of the sample, (4) density of the sample, (5) temperature of the sample and (5) the cross section source should be set to TABLES.^[103]

3.2.3 EPSR

Modelling of diffraction data is a key technique in the study of amorphous materials. The EPSR (Empirical Potential Structural Refinement) method^[104] was specifically developed for modelling the structure of molecular liquids^[105], but it is also applicable to amorphous solids with molecular units due to the inherent disorder in both systems. EPSR is a computational technique addressing the problem of calculating a three-dimensional structure exploiting the information contained in diffraction data.

EPSR uses a Monte Carlo method which samples different structures against an “acceptance” criterion, but unlike similar Monte Carlo methods such as Reverse Monte Carlo (RMC), the acceptance criteria is the energy minimum based on the interatomic potentials. EPSR is like RMC in using the diffraction data to guide the modelling process, but unlike RMC, the difference between the simulated and experimental diffraction is used to adjust the interatomic potentials. EPSR iterates a direct Monte Carlo simulation of a molecular system, correcting the pair interaction potential between

molecules at each stage of the iteration by comparison with the diffraction data sets. Below is a flow chart to show the operation of the EPSR algorithm:

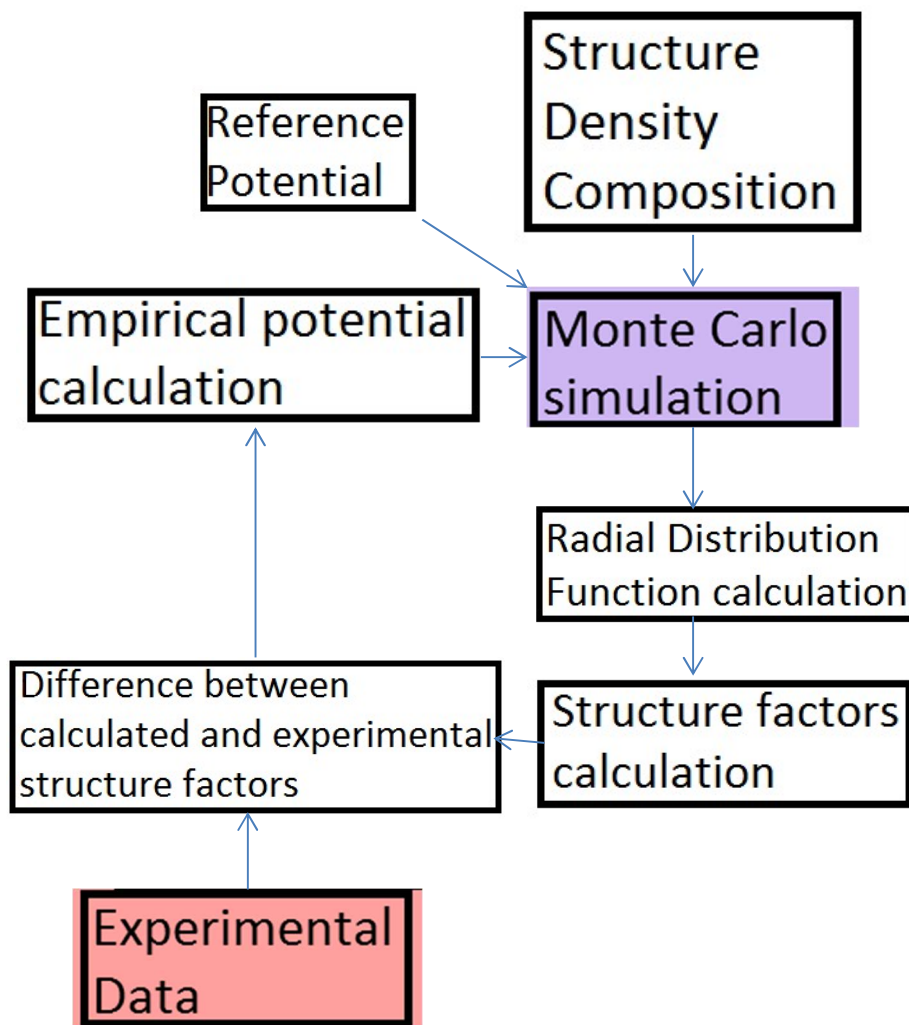


Figure 3.20 - EPSR algorithm flow chart starting with the experimental data (input by user)

For this project, a generic EPSR method was developed for use on all experimental data sets. Any deviations from which will be discussed in the relevant chapter.

1. Using molecular units, generated in GHEMICAL, a cubic box is generated with experimentally accurate composition and density.
2. The molecules unites were randomly translated to move them apart throughout the box. To further separate the molecules, the molecules were randomly rotated and translated 10,000 times.
3. Starting inter-molecular potentials for each inter-atomic pair correlation $i-j$ were generated by EPSR using built-in parameters for Lennard-Jones potentials for each pair of elements. Coulomb interactions are included with formal charges for ions.
4. The EPSR procedure initially relaxed the random starting configuration to an energy minimised structure using a simulated annealing approach with a temperature sequence: 10,000 K, 5000 K, 1000 K, 500 K and 300 K. At each temperature EPSR carries out Monte Carlo sampling of structures until reaching an equilibrium minimum energy.
5. This process was iterated approximately 20,000 times.

6. The potential refinement was then implemented within the EPSR

The difference between the simulated and experimental neutron and x-ray diffraction data are used to adjust the inter-atomic potentials. The comparison between simulation and experiment is carried out using the structure factors $S(Q)$.

3.2.3.1 *EPSR vs. RMC*

EPSR and RMC are both viable analytical routes to determine structures from diffraction but after testing and evaluating the EPSR software package compared to the latest RMC (RMCPProfile) package, the author decided to utilise EPSR. This was based on a number of factors but the most compelling was that EPSR is tailor-made to work with disordered systems, like amorphous biominerals. EPSR has the ability to model short range order and atom interactions of a sample in a chemically realistic way. The price for this chemical realism however, is an increase in computing time.

The decision to not work with RMCPProfile was also based on the fact that RMCPProfile not only fits to experimental diffraction data but also to a reference "Bragg file" which is the reference crystal pattern which is highly unsuitable for a work focused on amorphous materials only. This feature can be deactivated but is an added complication which could have an adverse effect of the resultant model.

4. Results & Discussion

4.1 Amorphous Calcium Carbonate (ACC)

4.1.1 Synthesis

The first method trialled in this study was using a procedure detailed by Koga et al^[20] which was translated from Japanese to English and detailed the synthesis of ACC using calcium chloride, sodium carbonate and addition of small amounts of sodium hydroxide (to adjust the pH of the solution). Most recent syntheses of ACC are based on or reference the Koga method so this seemed like the best starting point to synthesise ACC.

Additionally, the Koga method was used and adapted by Michel et al^[17] where small quantities of sodium carbonate and calcium chloride were mixed together. This method was chosen for the work in this thesis because in Michel et al's study the sample of amorphous calcium carbonate (ACC) was used in a high-energy x-ray diffraction experiment so it was decided that this would be ideal. However, after numerous attempts by the author of this thesis, and by collaborators at the University of Leeds, to replicate the synthesis performed by Michel et al, all that could be produced was crystalline calcite.

In a paper by Jiang et al^[29] it was discussed that ACC could be produced and stabilised with addition of small amounts of Mg^{2+} ions. This became an alternate line of investigation and will be discussed further in chapter 4.2.

To create a stable sample of “additive-free” ACC, a method developed by Rodriguez-Blanco et al^[106] was used because resulting samples of ACC were shown to be stable for a period of approximately 3 days after synthesis – a huge improvement on other previous attempts by this author and previously reported^[22,29] stable samples of ACC. Stock solutions were prepared of the various reagents (seen in Table 4.1)

Table 4.1 – Stock solution preparation for ACC synthesis

Concentration of Stock Solution (mM)	Reagent	Mass (g)	Volume of Stock Solution (mL)
100	Calcium Chloride hexahydrate ($CaCl_2 \cdot 6H_2O$)	21.908	1000
100	Sodium Carbonate (Na_2CO_3)	14.204	1000

To prepare ACC, 7 mL each of the 100 mM solutions of $CaCl_2$ and Na_2CO_3 were transferred to separate polypropylene tubes. The $CaCl_2$ and Na_2CO_3 solutions were mixed rapidly to produce a white precipitate in a Millipore™ glass filtration kit. This was then filtered (in under 30 seconds) through a Cyclopore® 0.2 μm pore size, track-etched polycarbonate membrane filter (47 mm diameter) and washed with isopropanol and dried in flowing air.

A deuterated sample of ACC was prepared on site at the ISIS neutron facility (see Figure 4.1) to enable study by neutron diffraction. The above method was modified to take place in an Argon glovebox. These modifications include preparing the solutions of $CaCl_2$ and Na_2CO_3 in D_2O and isopropanol- d_8 was purchased from Sigma-Aldrich. During the drying procedure the washed precipitate, along with the membrane filter, was placed in a 28 mL glass sample bottle in a desiccator

inside the Argon glovebox. When sufficient amount of sample was prepared, the desiccator was sealed and kept under vacuum for a minimum of 1 hour before loading into a sample holder and the sample holder loaded immediately onto the beamline.



Figure 4.1 - Experimental synthesis setup at ISIS facility in an Argon gas chamber showing the vacuum pump (left), filtration kit (centre) and solutions made in D₂O (right)

4.1.2 *Lab-based characterisation*

4.1.2.1 *Laboratory XRD*

To determine whether a sample was crystalline or amorphous, a freshly prepared sample was analysed using a Philips PW1730 diffractometer with a Cu anode, over a range of 10-70° 2 θ with a step size

0.02°. Figure 4.2 shows the x-ray diffraction pattern of a typical sample prepared by the Koga synthesis, figure 4.3 a Michel synthesis and figure 4.4 is that from a Rodriguez-Blanco synthesis.

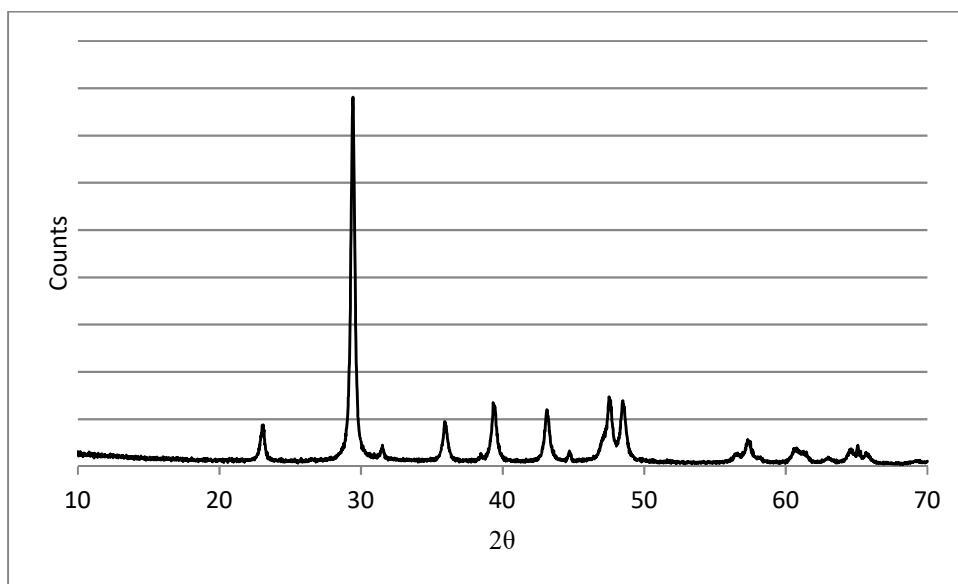


Figure 4.2 – XRD pattern of Koga synthesis of ACC, clearly showing a crystalline sample of calcite

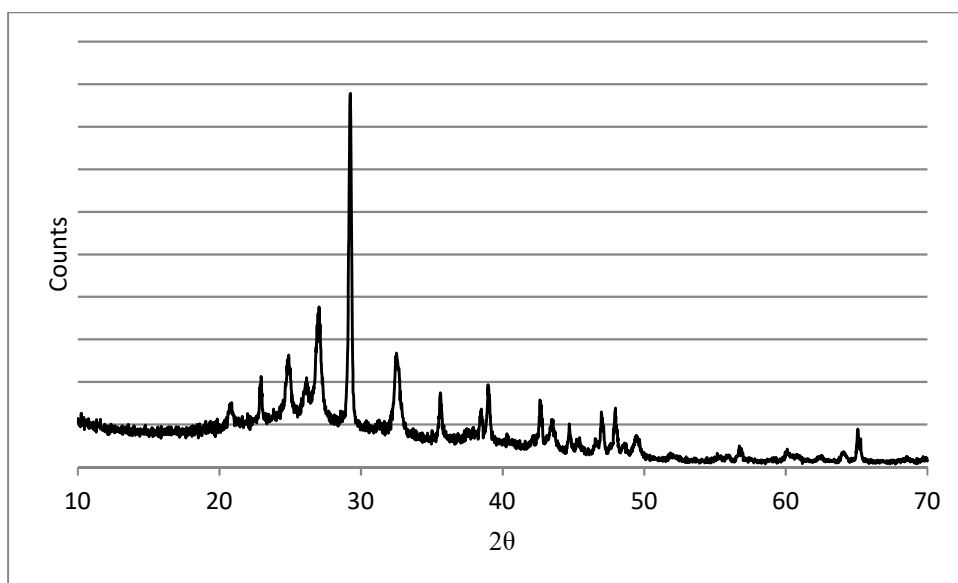


Figure 4.3 – XRD pattern of a Michel synthesis sample of ACC, showing a crystalline sample calcite but with some underlying disorder.

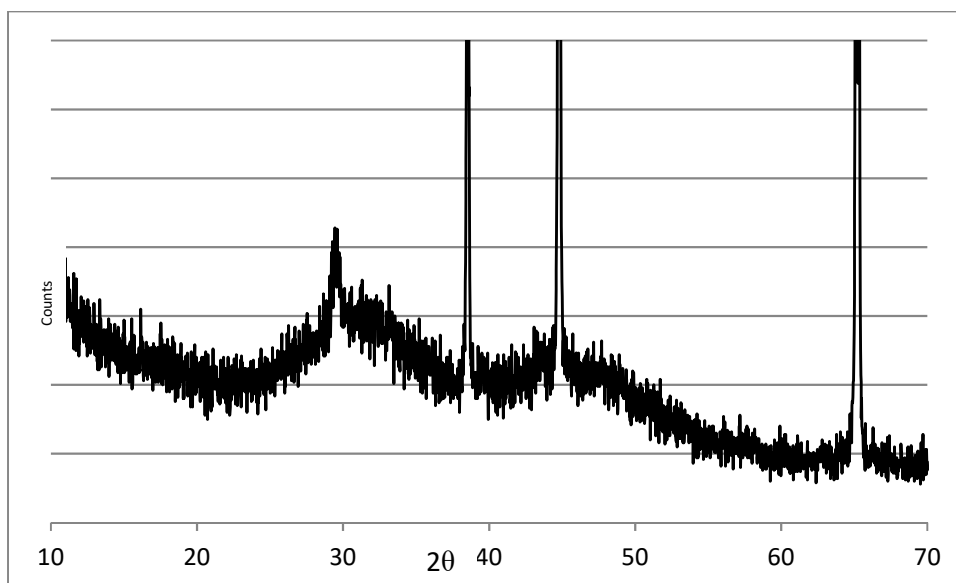


Figure 4.4 - XRD pattern of Rodriguez-Blanco synthesis sample of ACC, this sample is amorphous. The Bragg peaks are from the x-ray beam penetrating the thin layer of sample and correspond to the aluminium sample holder

From figures 4.2-4.4 it is clear to see that the best sample synthesis is the Rodriguez-Blanco method as it is the only amorphous sample (with the exception of the Bragg peaks corresponding to the x-ray beam penetrating the thin layer of sample and diffracting off the aluminium sample holder/XRD instrument). All samples produced in this work will follow the Rodriguez-Blanco method.

4.1.2.2 *Thermo-Gravimetric Analysis (TGA)*

Normally a TGA-DTA measurement of the sample would be necessary to determine the water content of the sample but analysis of ACC using the TGA-DTA was not feasible due to the rapid dehydration and crystallisation of ACC. To determine the water content of the sample, we used the data from Mg-ACC (section 4.2) which is more stable than ACC but should in theory contain a similar amount of water due to the very similar production methods. It was found that in Mg-ACC the weight loss was consistent with a water content of $n=1.45$. The plot of the TGA-DTA can be seen in section 4.2.

As discussed in the introduction, ACC is said to have a composition of $\text{CaCO}_3 \cdot n\text{H}_2\text{O}$ where $n=1-1.6$ ^[17-20]. Thus the sample of ACC will be of composition $\text{CaCO}_3 \cdot 1.45\text{H}_2\text{O}$ which is consistent with the literature and will be the composition used in the EPSR model of ACC.

4.1.2.3 *Helium Micropycnometry*

A sample of ACC was loaded into a small aluminium can which was then placed into the He-pycnometer and this was left to purge with helium for approximately 10 minutes before operation could begin. This operation was performed on-site at the ISIS neutron facility immediately after the completion of the neutron experiments. The values of P1 and P2 were recorded in an Excel spreadsheet before correcting using the sample mass and container mass (all within Excel), figure 4.5 shows the P1/P2 ratio for ACC.

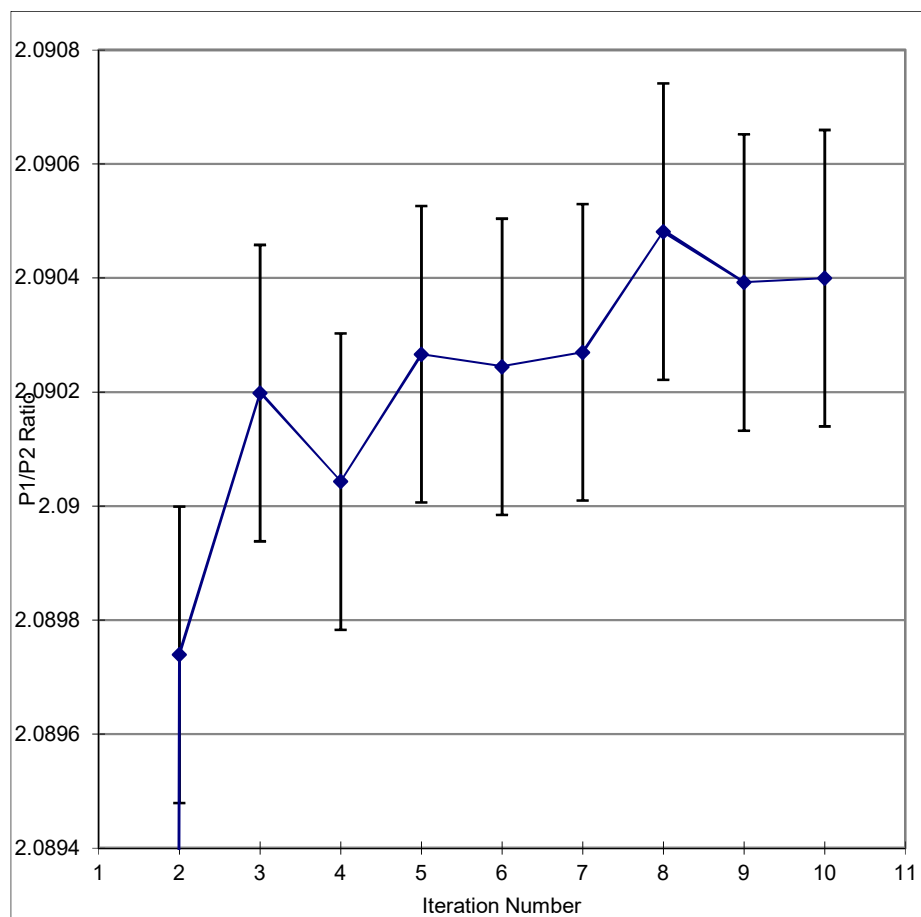


Figure 4.5 – He-pycnometry of ACC sample showing the P1/P2 ratio (as discussed in the experimental methods section), the procedure was repeated until the recorded density was within acceptable limits (1 s.d. - black error bar)

The density of ACC was calculated, using equation 3.5, to be $2.46 \text{ g/cm}^3 \pm 0.0028$ using the results for P1/P2 obtained from a He pycnometer. This density will be used in the EPSR model for ACC.

4.1.2.4 FTIR

Whilst on-site at ISIS, a portable FTIR (lent to us by our collaborators Liane Benning and Juan Diego Rodriguez-Blanco) was utilised to study the amount of deuteration, solvent and stability of the sample. The FTIR was of benefit as it was able to fit in the Argon gas chamber - pictured below in figure 4.6. A sample of D-ACC was prepared and placed on the FTIR to give a real-time FTIR spectrum of the sample, a longer, recorded spectrum was obtained by scanning for approximately 30 minutes (figure 4.7)



Figure 4.6 - the portable FTIR, bottom of the picture (red/black box) and connected to a laptop in the Ar chamber during sample synthesis at ISIS

The results from these tests prior to neutron diffraction are shown in figure 4.7, 4.8 and 4.9 that detail the first, second and third attempts to produce a deuterated sample of ACC.

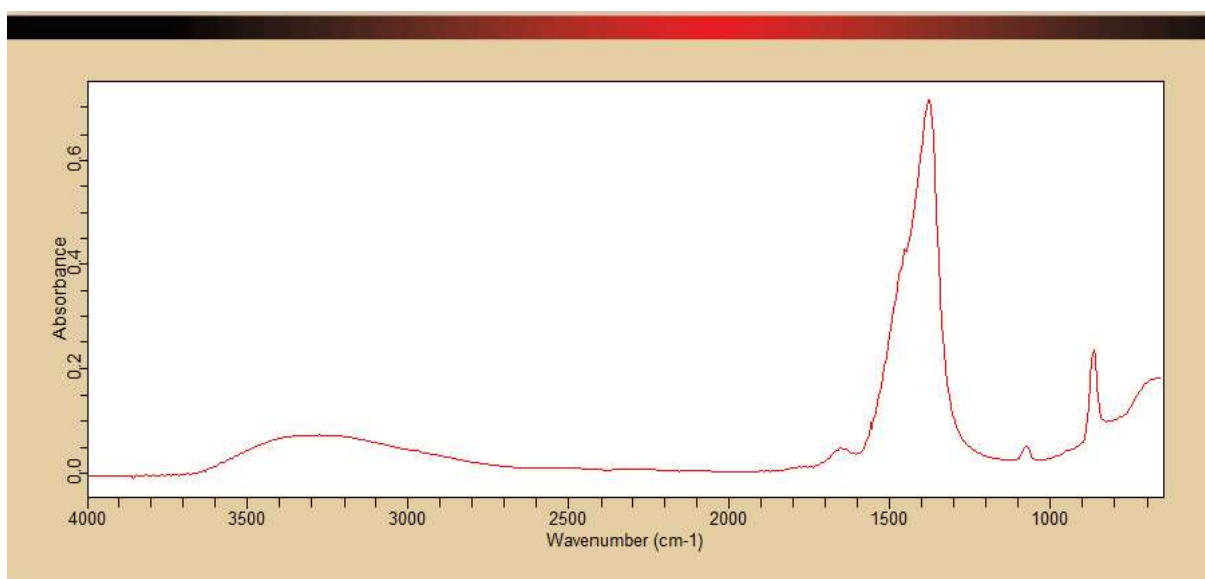


Figure 4.7 – First attempt to produce a deuterated ACC, showing mostly hydrogen content (the broad signal at 3500-3000 cm^{-1}) and a lack of deuterium (which should be seen with a broad signal at approximately 2700-2100 cm^{-1})

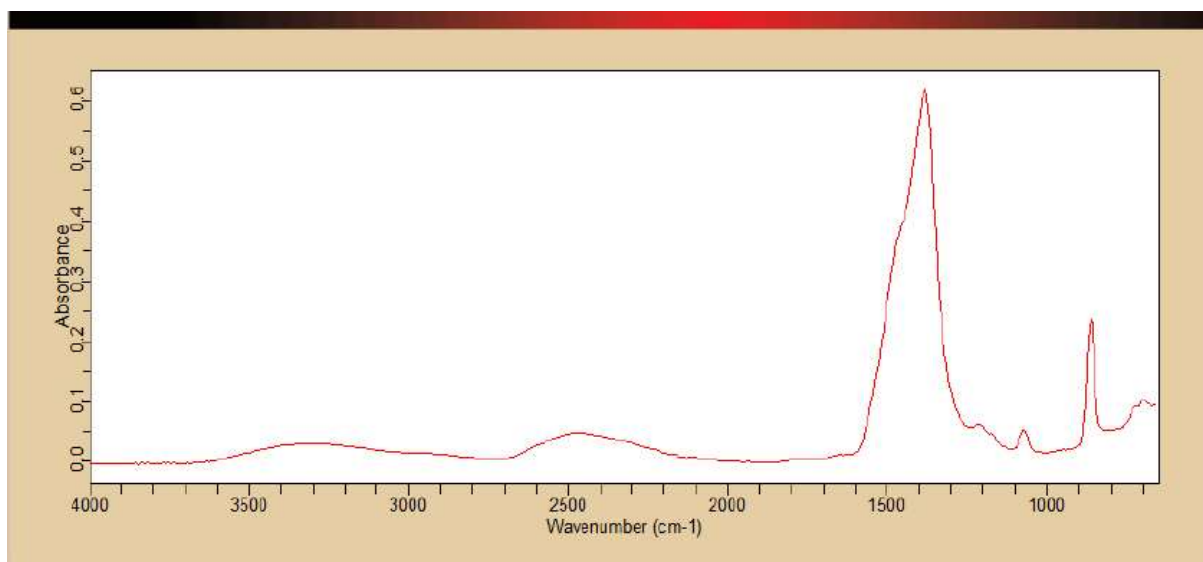


Figure 4.8 – Second attempt to produce deuterated ACC, showing approximate 50% deuteration after integration of the curve under the hydrogen region (3500-3000 cm^{-1}) and deuterium (2700-2100 cm^{-1})

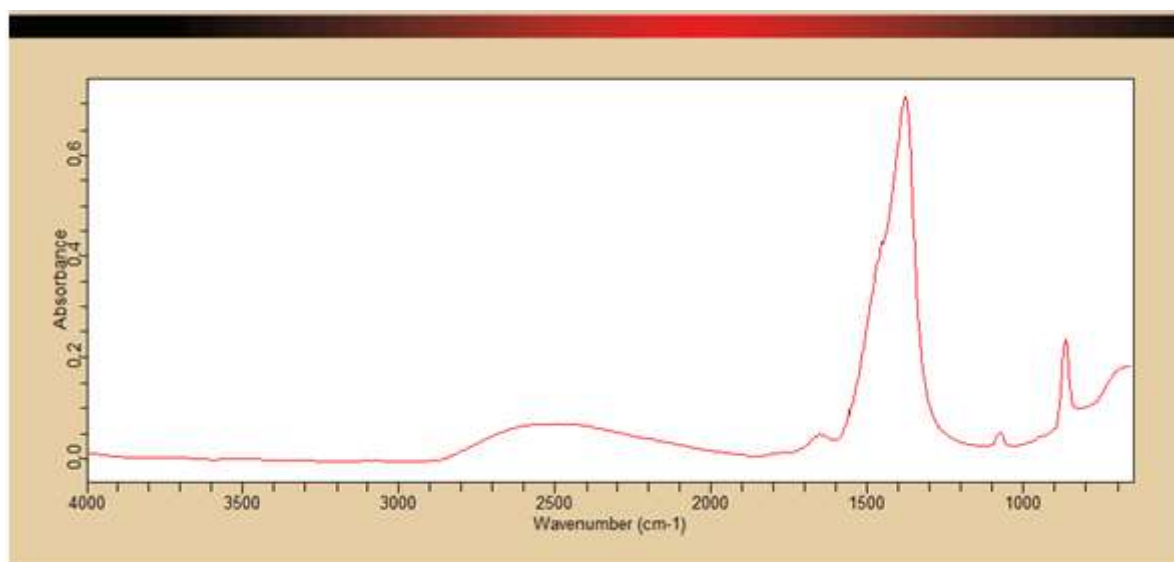


Figure 4.9 – Final attempt to produce deuterated ACC, showing 100% deuteration with the absence of a signal at 3500-3000 cm^{-1} and the only signal present in the deuterium region at 2700-2100 cm^{-1}

From all three attempts, it can be seen that all are stable and deuterated to some extent with attempt one being fully undeuterated in figure 4.7, the second attempt with partial deuteration (approximately 50% deuteration) in figure 4.8 and the final attempt having 100% deuteration (with minor hydrogen content) shown in figure 4.9.

4.1.3 Central Facility Experiments

4.1.3.1 Synchrotron XRD

X-ray diffraction data were collected at the MCX diffractometer^[107] at the ELETTRA synchrotron, Italy, using a x-ray wavelength of $\lambda=0.620 \text{ \AA}$. The non-deuterated sample was synthesized on site at the synchrotron and immediately loaded into a 10 micron thick 1.5 mm diameter silica capillary. The capillary was rotated during the experiment. X-ray diffraction data were collected up to 2θ of 120° or $Q=20 \text{ \AA}^{-1}$. The processing of the raw data included corrections for the background scattering, polarization, sample thickness, absorption, capillary, Compton scattering, and the sharpening function

(equal to the square of the average form factor per atom) using Excel. The structure factor $S(Q)$ profile from x-ray diffraction is shown in Figure 4.10.

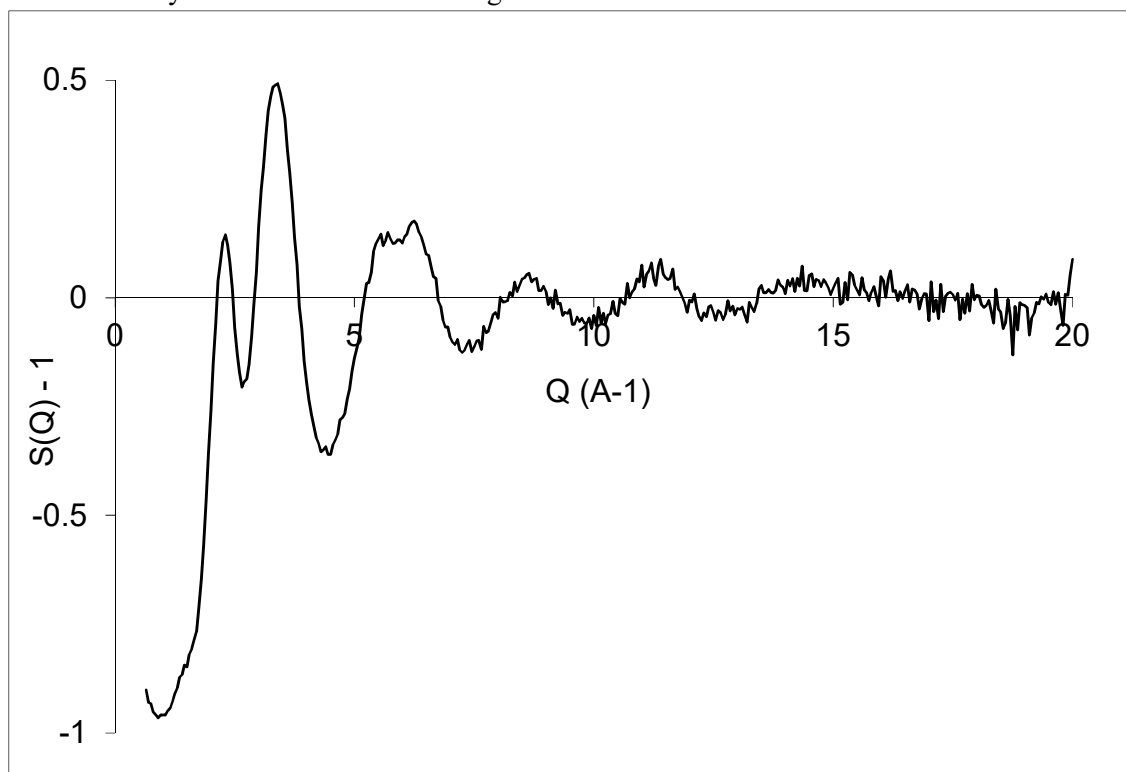


Figure 4.10 – X-ray $S(Q)$ profile of ACC, obtained from the Elettra synchrotron, Italy

Problems occurred when samples of ACC crystallised immediately or soon after being loaded onto the beamline. This decreased the amount of exposure time samples had and can be seen by the “noise” at high Q .

4.1.3.2 EXAFS

At the EXAFS beamline at the ELETTRA synchrotron, Italy non-deuterated samples of ACC were prepared on site and studied together with pre-prepared crystalline standards of calcite, aragonite and monohydrocalcite.

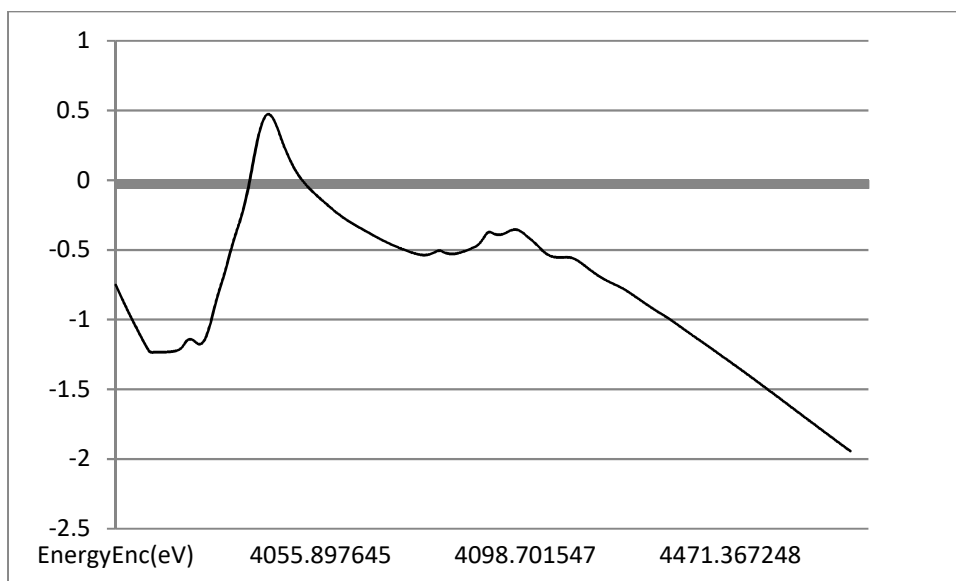


Figure 4.11 - EXAFS of ACC, showing a peak at 4048 eV

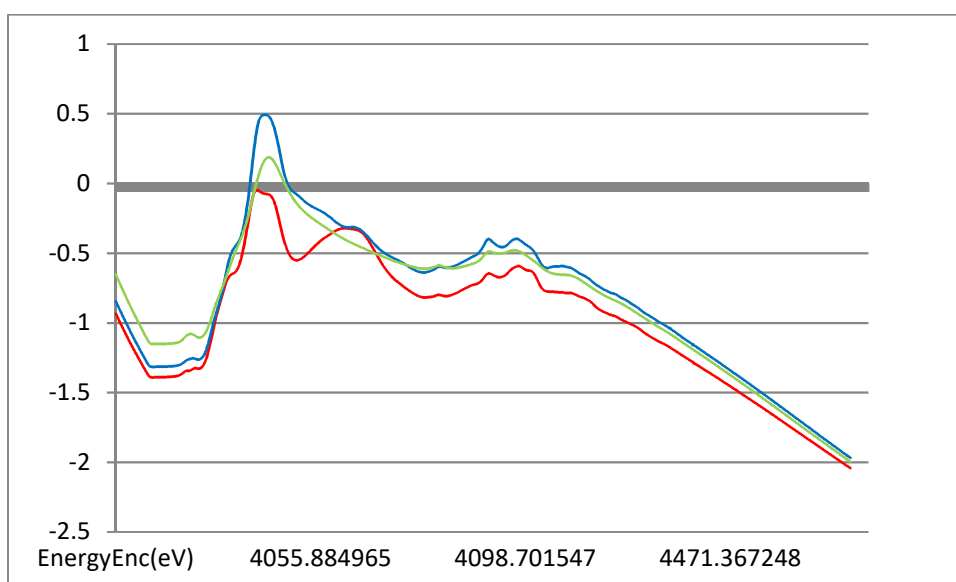


Figure 4.12 - EXAFS of reference samples - calcite (red), aragonite (blue) and monohydrocalcite (green)

4.1.3.3 Neutron Scattering

Neutron diffraction data were measured using the SANDALS diffractometer^[108] at the ISIS pulsed neutron source, UK. The deuterated samples were produced on the day of the experiment and loaded into a flat plate holder sample holder with 25 micron thick TiZr plate 4mm apart (figure 4.13).

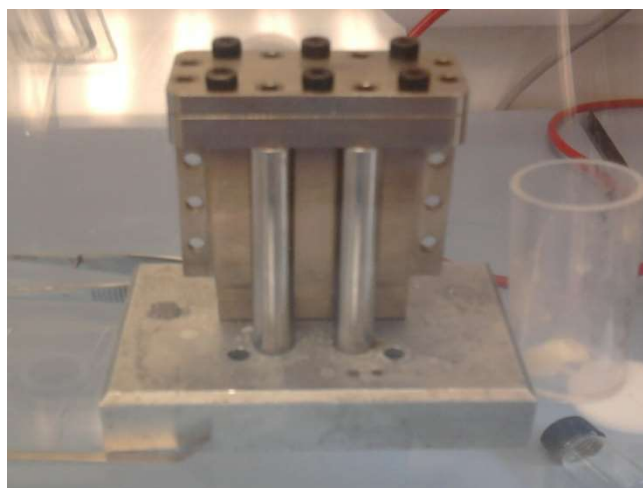


Figure 4.13 - Loaded TiZr sample container in the Ar chamber before being loaded into the SANDALS beamline

The sample holder was sealed and maintained at a temperature of 5 °C during the experiment. Time-of-flight data (i.e. λ is a function of time) were collected over a wide range of up to Q of 30 \AA^{-1} (where $Q = 4\pi \sin \theta/\lambda$). The raw data was processed using the GUDRUN suite of programs.

During the first experiment to study a deuterated ACC sample, shown in figure 4.9, whilst the FTIR spectrum showed that the sample was deuterated, amorphous and stable when the sample was loaded, some isopropanol must have remained on the sample because after analysing the data, it was clear that structure factor profile was very similar to that of isopropanol.

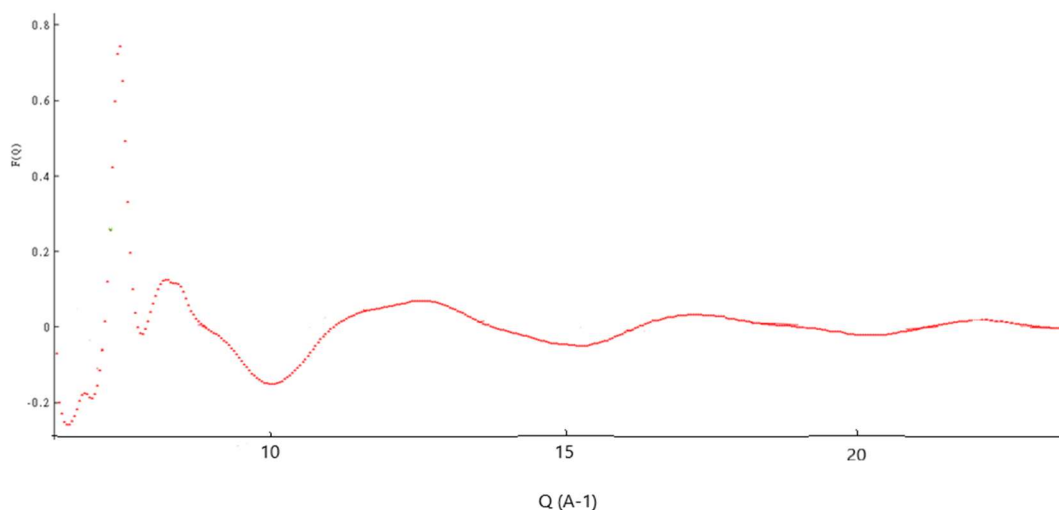


Figure 4.14a – $S(Q)$ profile of the first attempt to study deuterated ACC at ISIS neutron facility, EPSR output before being fit to computational model.

This interpretation was confirmed when comparing with a study by Zetterström et al^[109] who conducted neutron diffraction on various solvents including isopropanol which can be seen in figure 4.14b. It was suspected that inadequate drying of the sample in the glovebox had contributed to the sample being ‘wet’ with isopropanol.

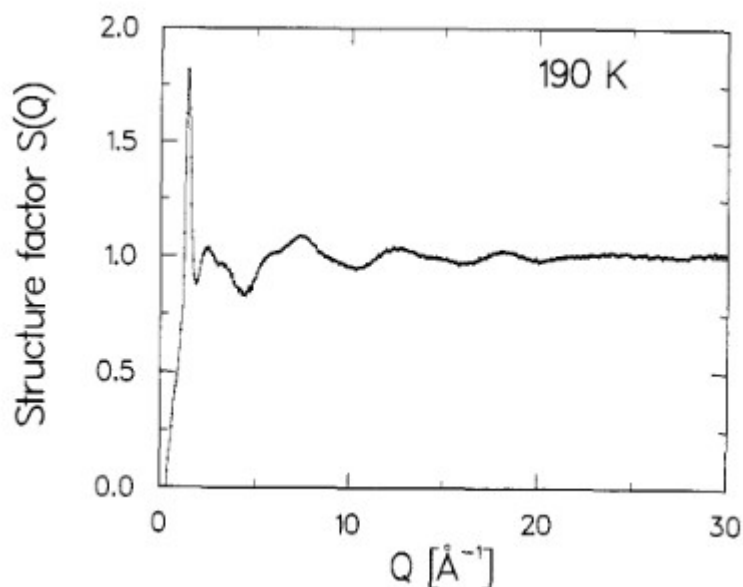


Figure 4.14b – Structure factor of Isopropanol as presented by P Zetterström et al^[109], very similar to figure 4.12

On a subsequent experiment, with adequate drying techniques introduced, to study deuterated ACC, hydrogen was present within the Ar glovebox. Possibly this was due to inadequate purging/flushing of the glovebox after loading or to a source of hydrogen being introduced from our equipment (possibly the pump or if the glovebox being used was not able to remove 100% of the hydrogen). However, the sample produced contained approximately 50% hydrogen and 50% deuterium. The structure factor for this sample can be seen in figure 4.15a below

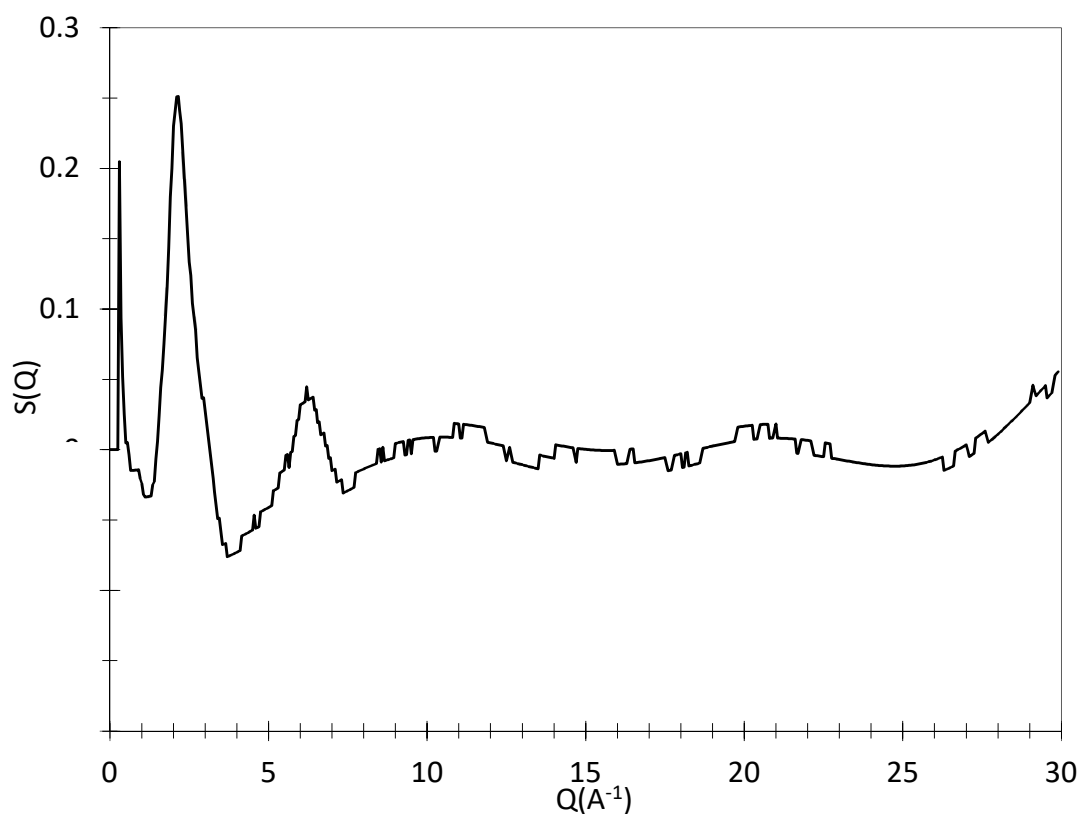


Figure 4.15a - Second attempt to study deuterated ACC with 50/50 split between hydrogen and deuterium.

The third and final attempt to study deuterated ACC was achieved during a SANDALS experiment on deuterated amorphous calcium phosphate (ACP) and resulted in a 100% deuterated sample of ACC being produced with possibly a small contribution from hydrogen but this was deemed to be negligible. This structure factor profile can be seen in figure 4.15b.

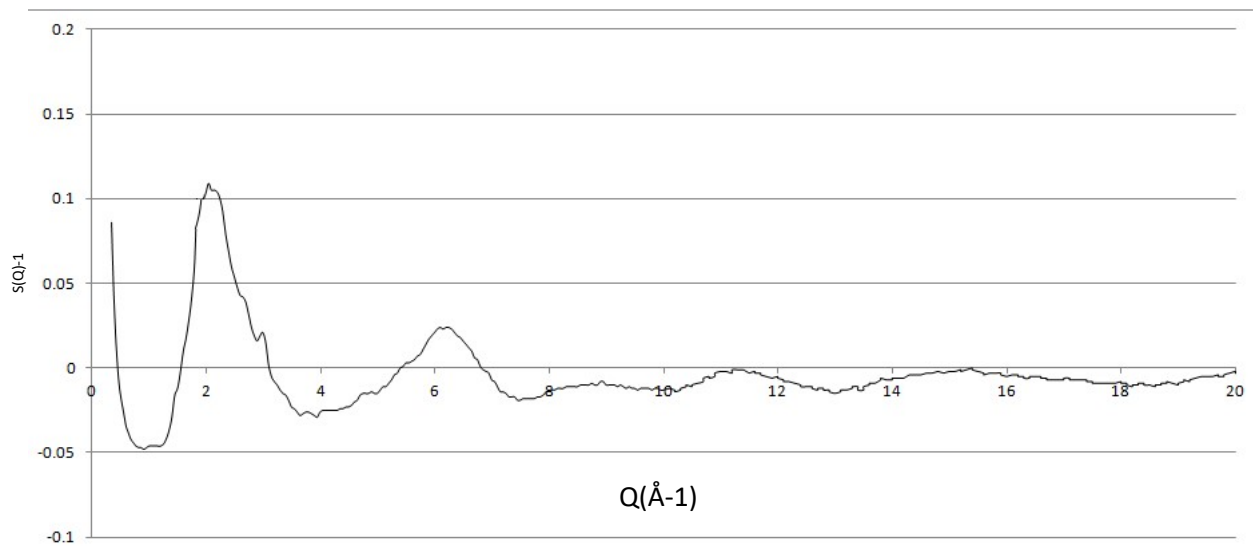


Figure 4.15b - Third attempt to study deuterated ACC with 100% deuterated sample.

Thus, the neutron diffraction experiment confirmed the sample to be fully deuterated and it was these data that were used in subsequent EPSR modelling.

4.1.4 Empirical Potential Structure Refinement (EPSR) Modelling

Structurally realistic molecular units were initially constructed using GHEMICAL4.0 software. A cubic box with length $L=40.65 \text{ \AA}$ containing 1000 Ca, 1000 CO_3 and 1450 D_2O units (total 9250 atoms) was assembled using the EPSR shell. This model corresponds to the measured density for ACC of 2.46 g/cm^3 .

The procedure detailed in section 3.2 and the information above yielded the following atomistic structure of ACC:

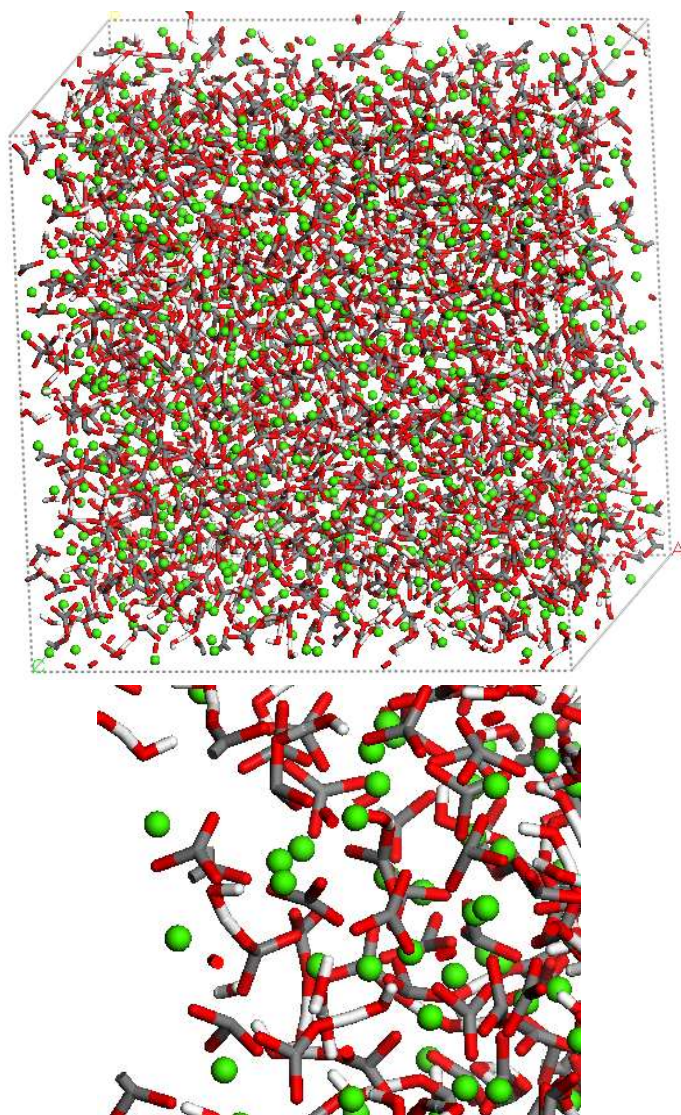


Figure 4.16 - Atomistic Structure of ACC (above), calcium (green), oxygen (red), carbon (grey) and deuterium (white). Below is a zoomed close up of the short-range structure of ACC.

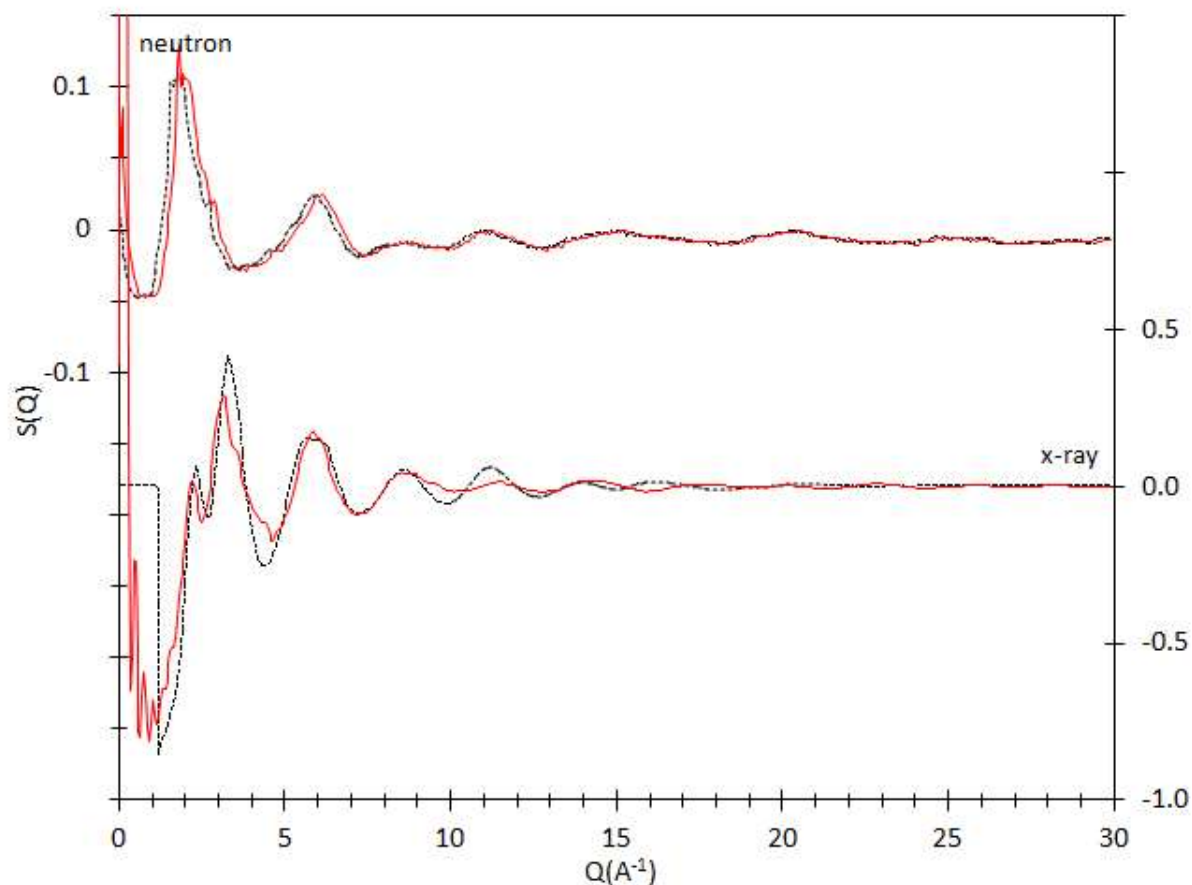


Figure 4.17 - Observed (black) and calculated (red) $S(Q)$ profiles for neutron and x-ray data of deuterated ACC.

Individual pair correlation functions $g_{ij}(r)$ were calculated and those involving CO_3^- ions and H_2O molecules are shown in Figure 4.18. The first four peaks in the PDFs represent the internal structure of the molecules: O-H and H-H distances in H_2O , and C-O and O-O distances in CO_3 . In addition, there are inter-molecular (the interactions between different molecules and molecular units) and intra-molecular (the interactions within molecules or molecular units ie. C-O bond in CO_3 unit) correlations. These correlations and their peak distances are summarised in Table 4.1.

Table 4.1 - Interatomic correlations involving CO₃⁻ ions and H₂O molecular units. (* denotes correlations involving hydrogen bonding)

distance (Å) (approximate)	atoms types i-j	molecular ion units	Coordination Number
0.93 and (1.3)*	H-O	intra and inter* H ₂ O	1.2 and (1.0)
1.25	C-O	intra CO ₃	3.5
1.56 and (1.9)*	H-H	intra and inter* H ₂ O	1.8 (0.8)
2.22	O-O	intra CO ₃	3.0
(2.3)	C-H	inter CO ₃ and H ₂ O	2.6
2.4	Ca-O		6.5 (CO ₃) and 1.0 (H ₂ O)
(2.8)	O-O	inter CO ₃ (and H ₂ O)	N/A (large number of O at distances greater than 2.5 Å)
3.3	Ca-C		6.2 (CO ₃)
(3.3)	C-O	inter CO ₃ (and H ₂ O)	N/A (large number of O at distances greater than 2.5 Å)
(3.5)	C-C	inter CO ₃	5

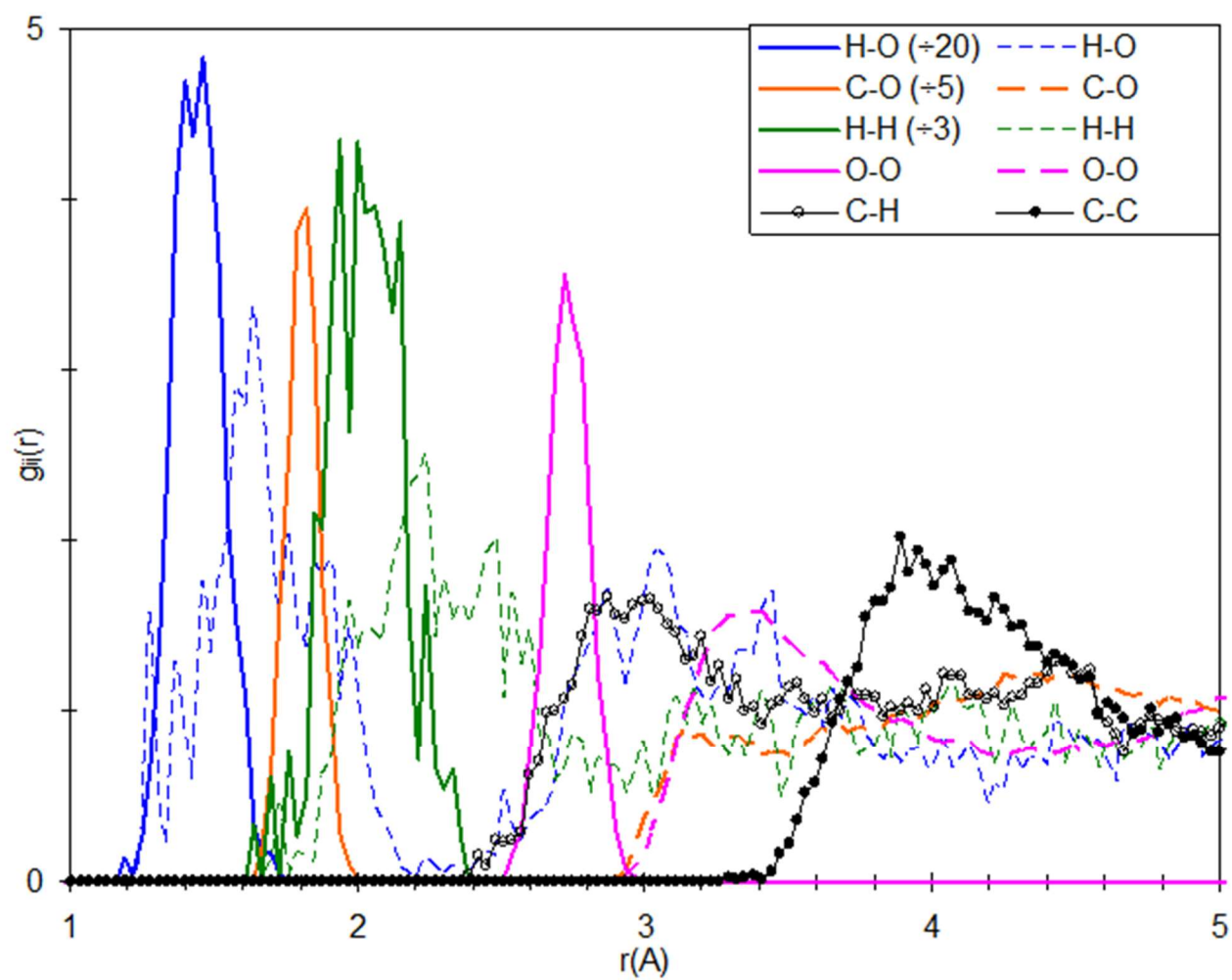


Figure 4.18: pair distribution functions $g_{ij}(r)$ involving CO_3^{2-} and H_2O moieties for D-ACC from EPSR model. (See Table 4.2 for details of the correlations and peak distances).

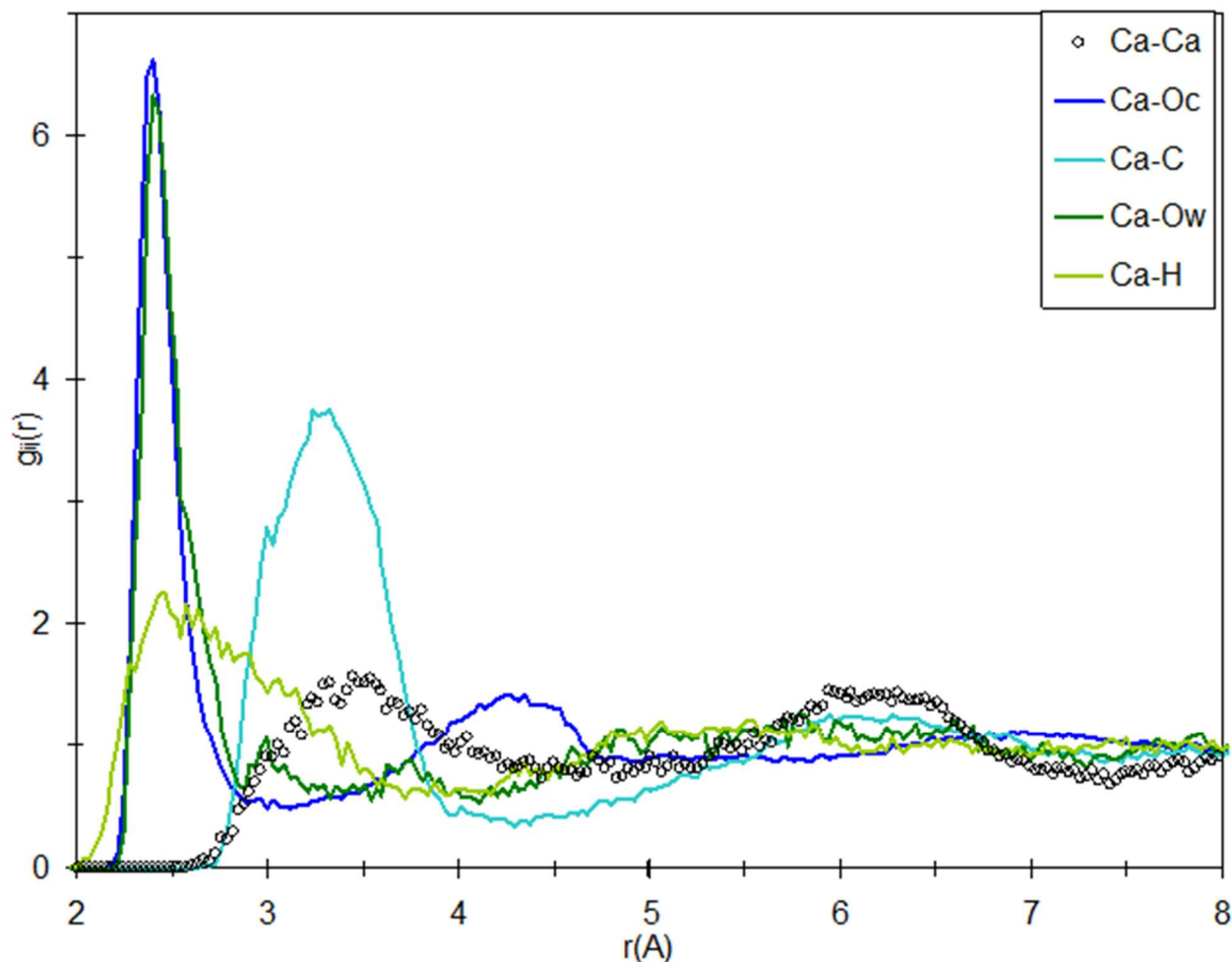


Figure 4.19: pair distribution functions $g_{ij}(r)$ involving Ca for D-ACC from EPSR model. (Note Oc and Ow refer to oxygens in CO_3 and H_2O molecules respectively).

Figure 4.19 shows the pair correlations involving calcium. Most prominent are the Ca-O distances due to Ca bonding to the oxygen atoms which are present in CO_3 and H_2O molecular ions, where the peak distance is 2.42 Å. The average coordination number of Ca is found to be 7.2 which are composed of 6.8 oxygen atoms from CO_3 molecules and 0.6 oxygen atoms from H_2O molecules. These features of the model are in good agreement with the EXAFS results of Michel et al^[17] for ACC prepared by a similar method, which were Ca-O coordination number of 6.5 ± 1.6 and peak distance of 2.42 ± 0.02 Å. Due to the coordination of Ca to oxygen in CO_3 and H_2O molecules, there are consequently noticeable correlations of Ca...C and Ca...H.

The first peak at 3.3-4.5 Å in the Ca-Ca PDF (see Figure 4.19) corresponds to calcium which share bonds with common oxygen, i.e. Ca-O-Ca.

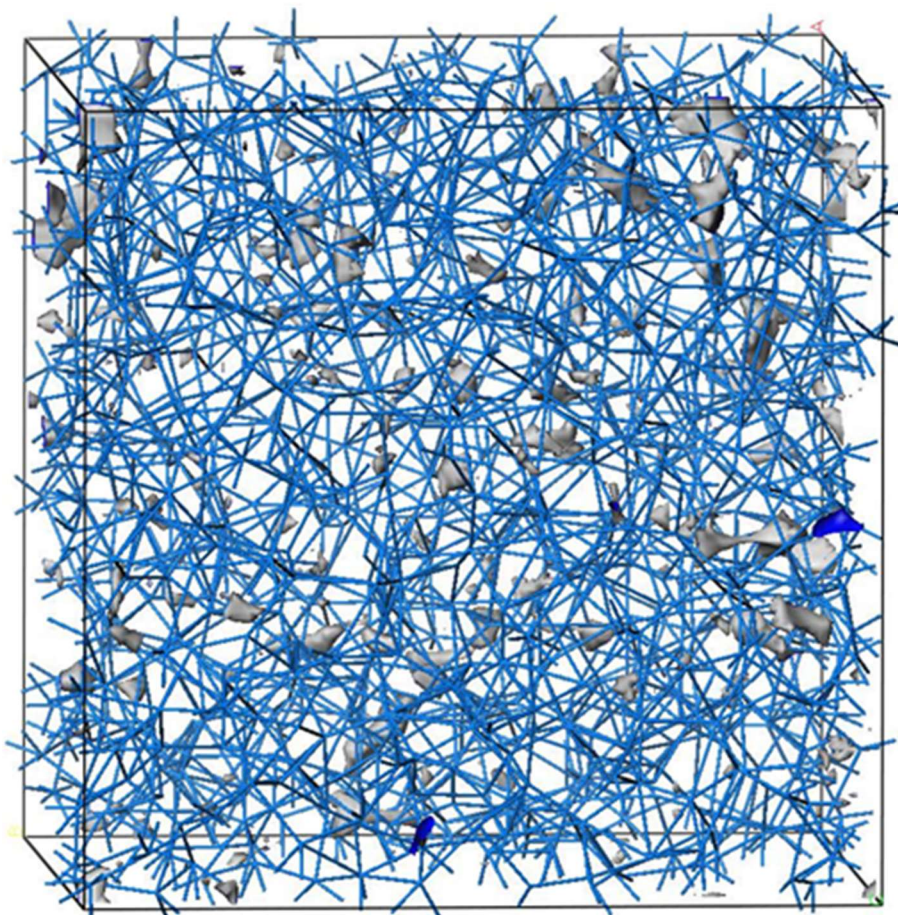


Figure 4.20: EPSR model of D-ACC with blue lines showing the Ca-rich network as blue sticks (i.e. Ca-O-Ca linkages). Marginal volumes of Ca-poor channels (based on the criteria of regions more than 3.3 Å distant from Ca) are shown as grey surfaces. (None are present using a criteria of 4 Å). A similar analysis was reported by Goodwin et al^[27].

Figure 4.20 (blue lines) shows that the "Ca-rich network" (based on Ca-O-Ca linkages) is homogeneously distributed. In addition, there are no Ca-poor channels based on the criteria of regions more than 4 Å distant from Ca. Figure 4.20 (grey surfaces) shows that when using a less stringent definition of Ca-poor channels based on the criteria of regions more than 3.3 Å distant from Ca there are only a few marginal volumes fitting these criteria. The significance of this is that it does not agree with the model produce by Goodwin et al^[17] where large channels of calcium rich and calcium poor regions were observed. This could be because in the Goodwin model, hydrogen was omitted to save on computational power/time. Thus free oxygens were allowed to roam through the model which is unrealistic.

4.2 Magnesium-stabilised Amorphous Calcium Carbonate (Mg-ACC)

4.2.1 Synthesis

As with ACC, the method developed by Rodriguez-Blanco et al^[106] was used due to its success in producing stable samples of ACC. The method was adapted, along with that of Jiang et al^[29] to prepare a sample of magnesium-stabilised ACC (Mg-ACC). In anticipation of this, stock solutions were created (seen in Table 4.3)

Table 4.3 – Stock solution preparation for Mg-ACC synthesis

Concentration of Stock Solution (mM)	Reagent	Mass (g)	Volume of Stock Solution (mL)
500	Magnesium Chloride (MgCl ₂)	47.606	500
100	Calcium Chloride hexahydrate (CaCl ₂ ·6H ₂ O)	21.908	1000
100	Sodium Carbonate (Na ₂ CO ₃)	14.204	1000

To prepare Mg-ACC, 5 mL of the 100 mM solutions of CaCl₂ and Na₂CO₃ were transferred to separate polypropylene tubes. To the CaCl₂ solution 0.5-5 mL of a 500 mM solution of MgCl₂ was added and this was then rapidly mixed with the Na₂CO₃ solution. This mixing produced a white precipitate in a Millipore™ glass filtration kit before being rapidly filtered through a Cyclopore® 0.2 µm pore size, track-etched polycarbonate membrane filter (47 mm diameter) and washed with isopropanol and dried in flowing air.

The precipitate was further heat-treated for 1 hour at a range of temperatures including 100 °C, 150 °C and 200 °C to reduce the water content. Temperatures were determined by TGA-DTA (discussed in section 4.2.2.2). A list of prepared samples of Mg-ACC can be seen in Table 4.4.

Table 4.4 – Prepared samples of Mg-ACC

Sample I.D.	Volume of MgCl ₂ Solution Added (mL)	Heat Treatment (°C)
Mg-ACCunh0.5	0.5	Unheated
Mg-ACCunh1	1	Unheated
Mg-ACCunh2.5	2.5	Unheated
Mg-ACCunh5	5	Unheated
Mg-ACC100	1	100
Mg-ACC150	1	150
Mg-ACC200	1	200

All of the above samples were studied until a suitable candidate was found to study via x-ray and neutron diffraction. As with ACC, a deuterated sample was also produced on site at ISIS for analysis using the method mentioned above and discussed in section 4.1.1.

4.2.2 Lab-based characterisation

4.2.2.1 Laboratory XRD

The samples of Mg-ACC with varying magnesium content (as detailed in Table 4.4) were analysed using XRD to confirm which were amorphous. Figure 4.21 shows the XRD patterns for all of the freshly prepared Mg-ACC samples

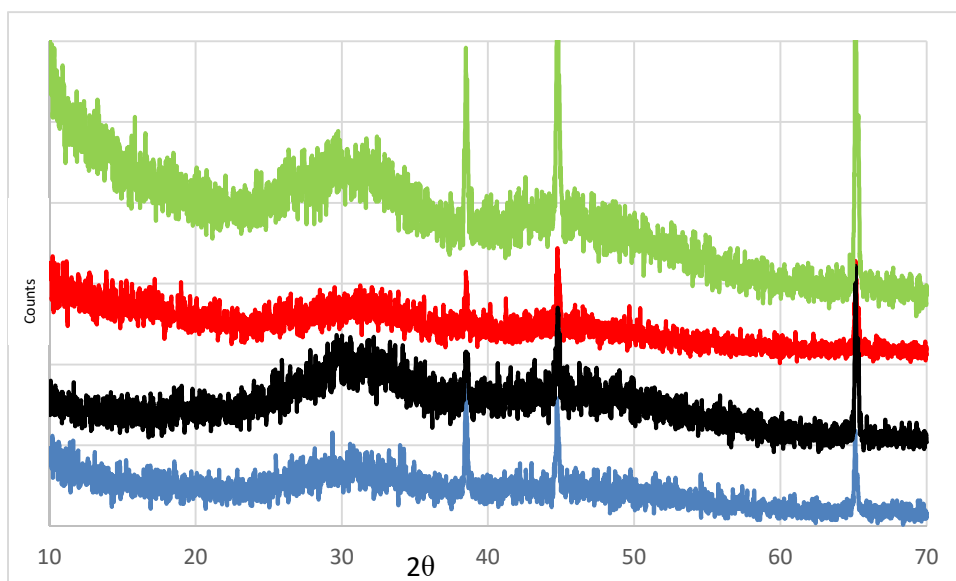


Figure 4.21 - XRD patterns for freshly prepared Mg-ACCunh0.5 (blue), Mg-ACCunh1 (black), Mg-ACC2 (red) and Mg-ACCunh5 (green).

As can be seen in figure 4.21, all of the unheated Mg-ACC samples were amorphous. These amorphous samples were kept sealed in a 5 mL glass bottle secured with lab film and re-measured at varying intervals (1, 3, 7 and 14 days after synthesis). As the objective was to have as little magnesium in the sample as possible, the results for Mg-ACCunh0.5 will be presented first.

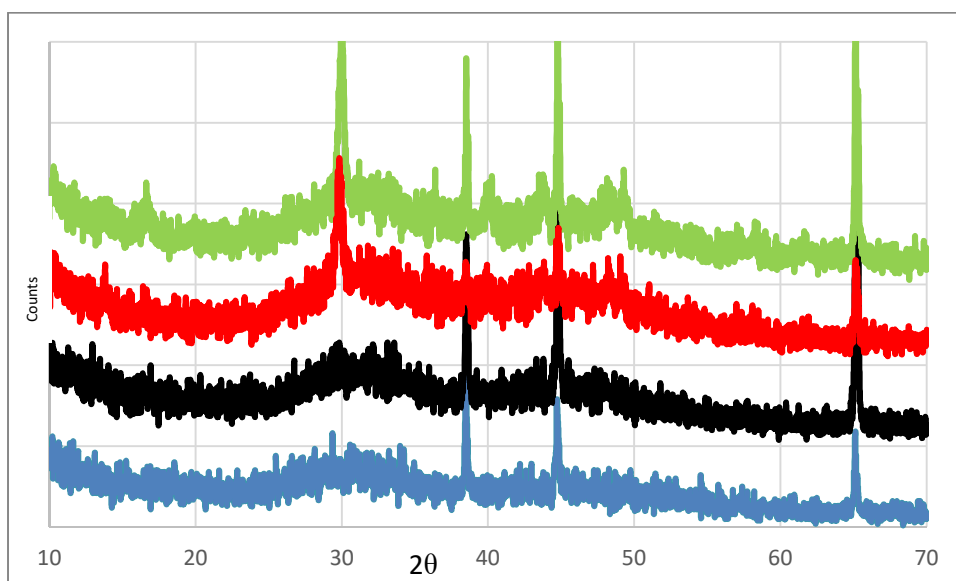


Figure 4.22 – XRD patterns for Mg-ACCunh0.5 over time from 0 days (blue), 1 day (black), 3 days (red) and 7 days (green) after synthesis.

As the sample of Mg-ACCunh0.5 began to crystallise around 3 days after synthesis, it was decided that this product was not suitable for this project as the lack of stability could compromise a central facility experiment. The next set of results are for the Mg-ACCunh1 sample.

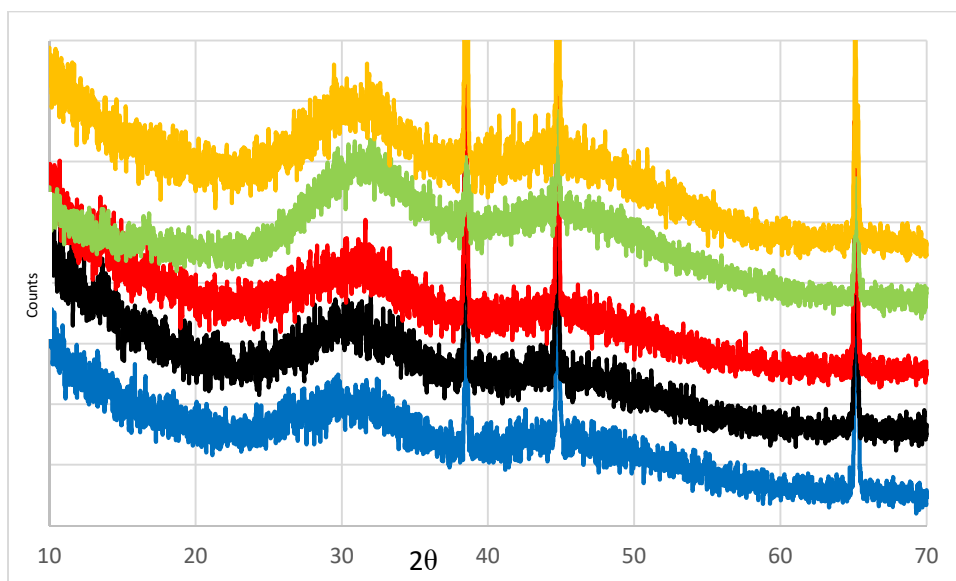


Figure 4.23 – XRD patterns for Mg-ACCunh1 over time from 0 days (blue), 1 day (black), 3 days (red), 7 days (green) and 14 days (orange) after synthesis.

From the XRD data gathered on Mg-ACCunh1, it was determined to be a suitable candidate for heat treatment. Each sample of Mg-ACC was now be prepared in the same manner as Mg-ACCunh1 and subjected to heating for 1 hour at the temperatures detailed in Table 4.4. As the objective of the heat treatment is to drive off as much interstitial water as possible, the results for the highest temperature (determined by TGA-DSC in section 4.2.2.2), 200°C, will be displayed first.

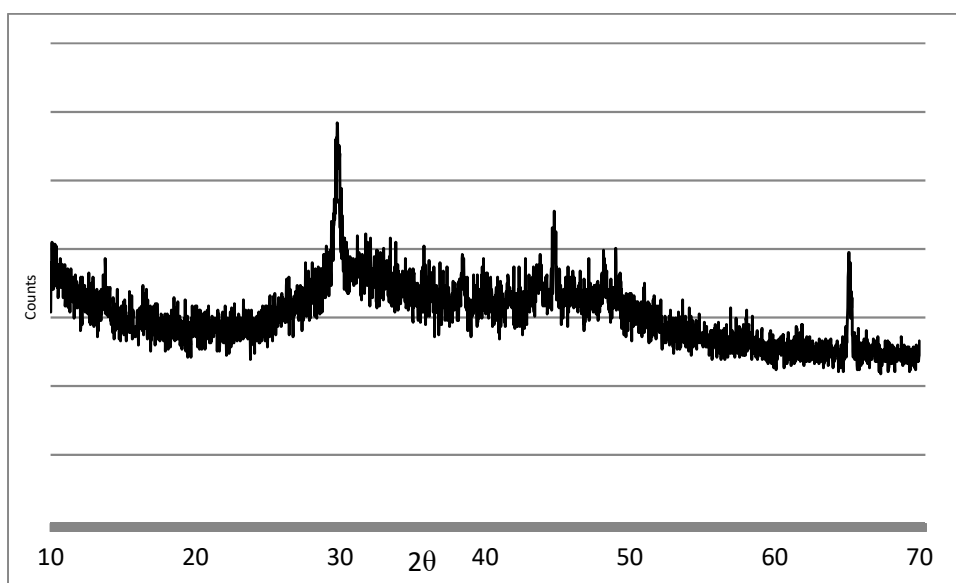


Figure 4.24 - XRD pattern for Mg-ACC200 immediately after 1 hour heat treatment.

As the sample of Mg-ACC200 was crystalline (starting to show the formation of calcite-like crystals) immediately after heat treatment, no further work was conducted on this sample. Attention was turned onto the next sample Mg-ACC150 and the XRD results are shown below:

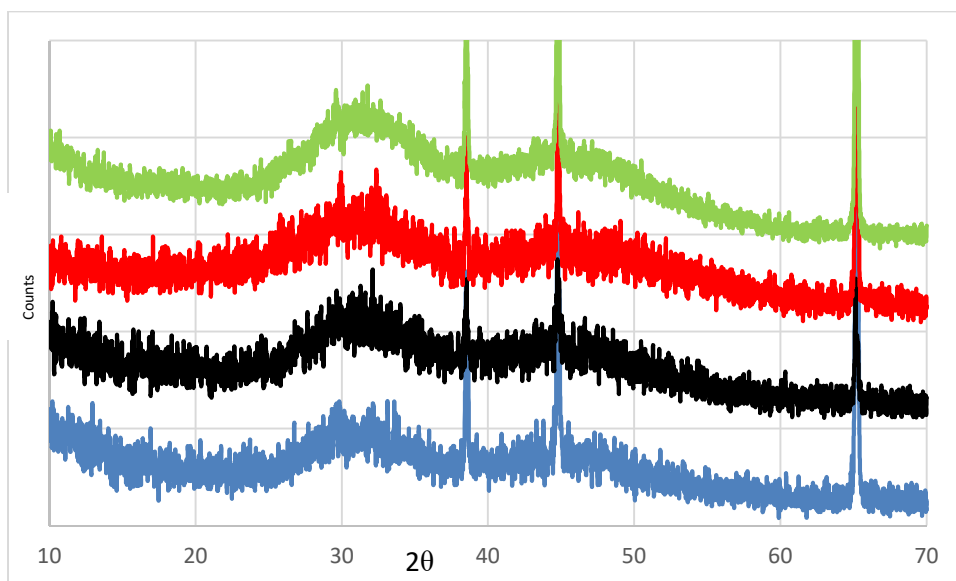


Figure 4.25 - XRD pattern of Mg-ACC150 immediately after 1 hour heat treatment (blue), 3 days (black), 7 days (red) and 14 days (green) after treatment

The Mg-ACC150 sample was amorphous for longer than two weeks which was ideal for central facility experiments with the minimal amount of magnesium added. All further work in this chapter will be based, unless stated otherwise, on Mg-ACC150.

4.2.2.2 *Thermo-Gravimetric Analysis (TGA-DTA)*

A sample of freshly prepared Mg-ACCunh1 was analysed using TGA-DTA and the results are shown in figure 4.26 and 4.27.

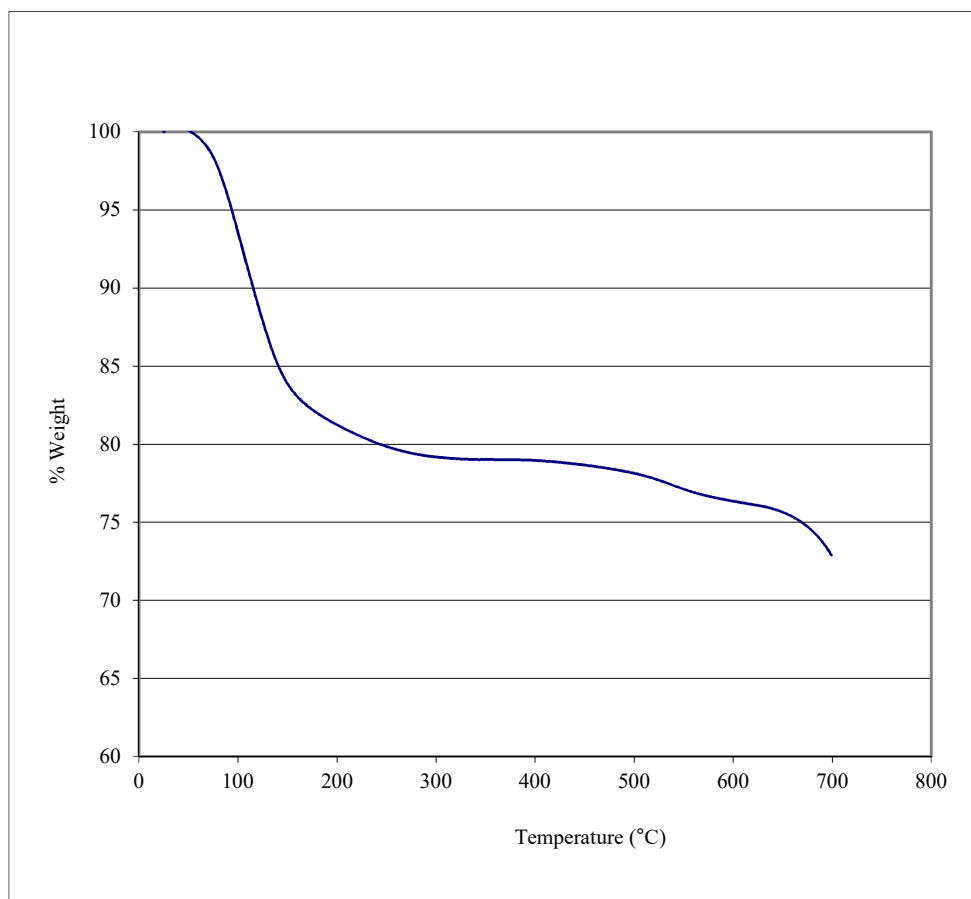


Figure 4.26 – TGA of Mg-ACCunh1, showing weight loss of 18% up to approximately 150°C and 21% to 350°C at which point Mg-ACCunh1 crystallises (see figure 4.27).

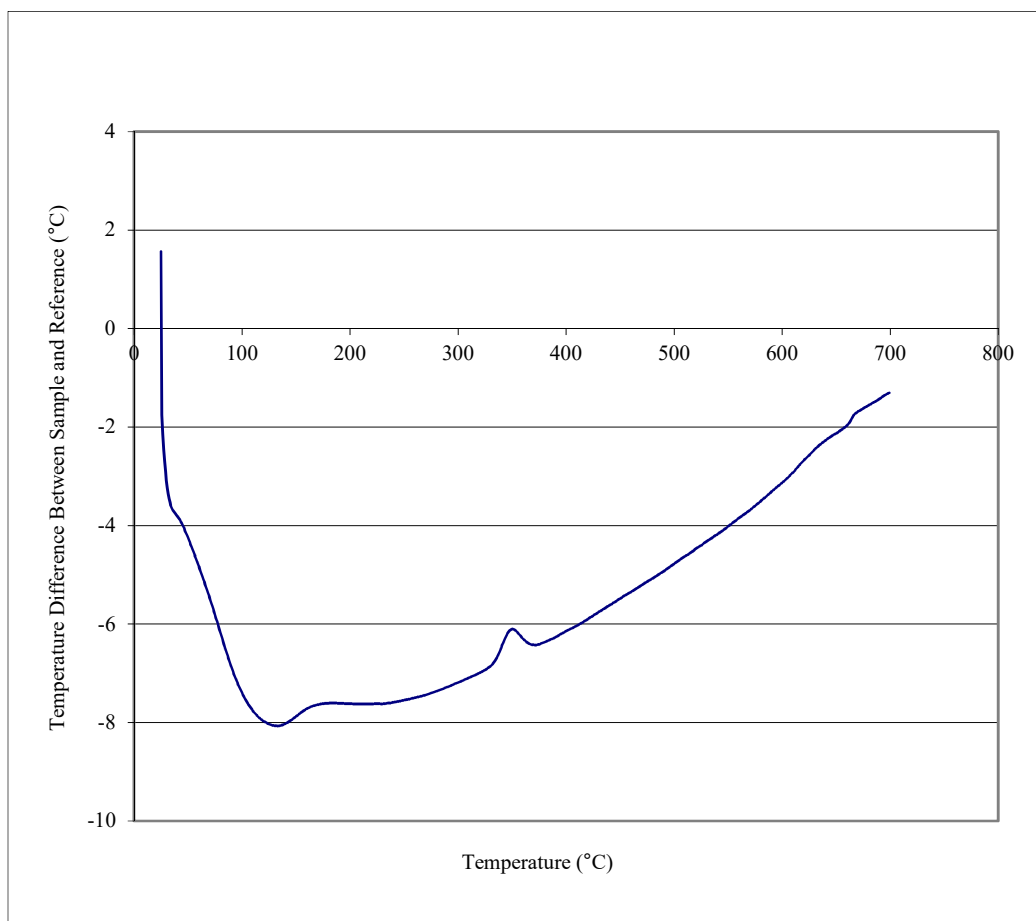


Figure 4.27 – DTA of Mg-ACCunh1 showing a crystallisation peak at approximately 350°C

The TGA-DTA of Mg-ACCunh1 showed weight losses of 18% and 21% up to temperatures of 150 °C and 350 °C respectively, the latter being when calcite crystallises. These weight losses are consistent with a water content of $n=1.45$ before and $n=0.25$ after heat treatment at 150 °C. This reduction of water content is important for neutron diffraction and will be used in the computational model of diffraction data.

4.2.2.3 Helium Micropycnometry

A sample of Mg-ACC150 was loaded into a small aluminium can which was then placed into the He-pycnometer and this was left to purge with helium for approximately 10 minutes before operation could begin. This operation was performed on-site at the ISIS neutron facility approximately 2 weeks after the completion of the neutron experiments due to the Mg-ACC150 sample being radioactive immediately after completion of the experiment. The values of P1 and P2 were recorded in an Excel spreadsheet before correcting using the sample mass and container mass (all within Excel), figure 4.28 shows the P1/P2 ratio for Mg-ACC150.

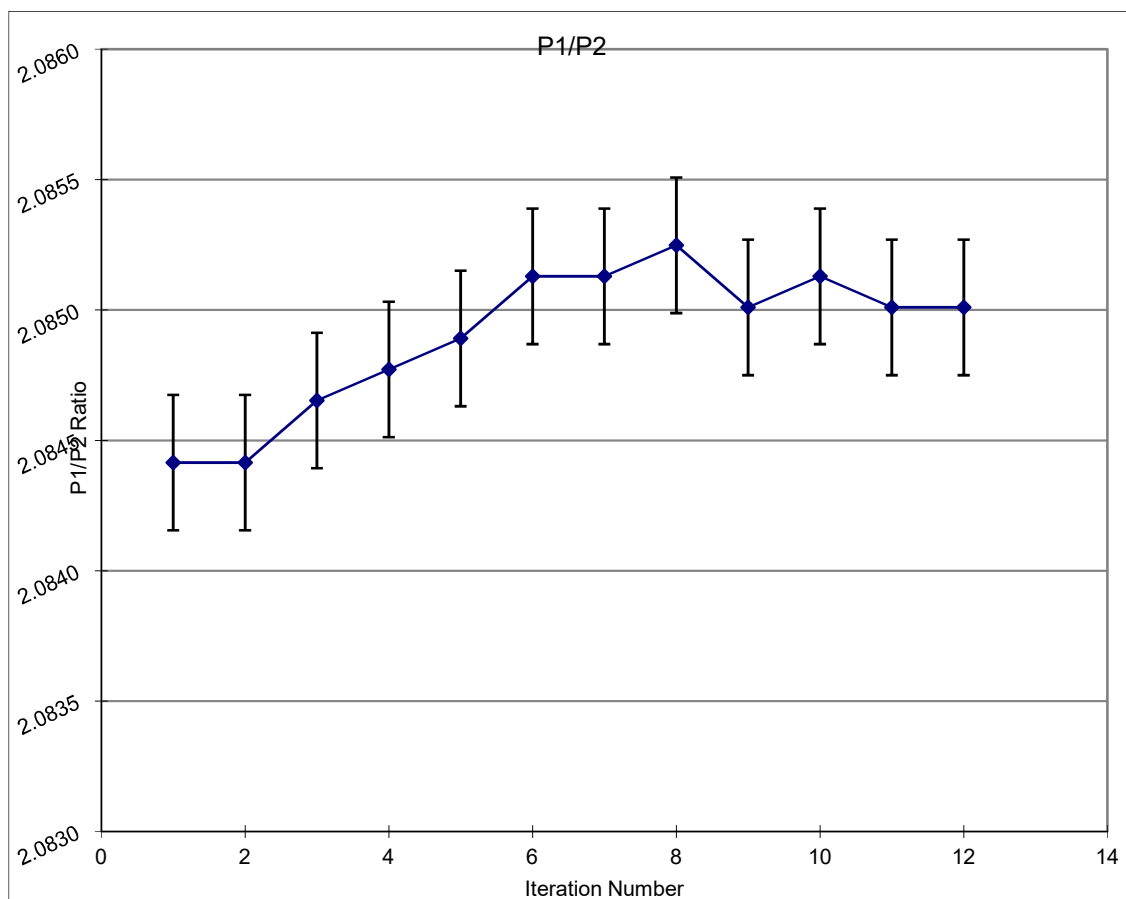


Figure 4.28 - He-pycnometry of Mg-ACC150 sample showing the P1/P2 ratio, the procedure was repeated until the recorded density was within acceptable limits (1 s.d. - black error bar)

The density of Mg-ACC150 was calculated to be 2.19 g/cm^3 using the results for P1/P2 obtained from a He pycnometer. This density will be used in the EPSR model for Mg-ACC150.

4.2.2.4 X-ray fluorescence (XRF)

A number of XRF experiments were carried out on samples of Mg-ACC150 and on average an Mg:Ca ratio of 0.05:0.95 was determined. This would mean that the final formula used for data analysis and the EPSR model would be $\text{Mg}_{0.05}\text{Ca}_{0.95}\text{CO}_3 \cdot n\text{H}_2\text{O}$ where $n = 0.25$.

4.2.3 Central Facility Experiments

4.2.3.1 Synchrotron X-ray Powder Diffraction

X-ray diffraction data were collected at the MCX diffractometer^[107] at the ELETTRA synchrotron, Italy, using a wavelength of $\lambda = 0.620 \text{ \AA}$. The sample was produced prior to travelling to the synchrotron and sealed until it was loaded into a 10 micron thick 1.5 mm diameter silica capillary. The capillary was rotated during the experiment. X-ray diffraction data was collected up to 2θ of 120° or $Q = 20 \text{ \AA}^{-1}$. The processing of the raw data included corrections for the background scattering, polarization, sample thickness, absorption, capillary, Compton scattering, and the sharpening function (equal to the square of the average form factor per atom). The structure factor $S(Q)$ profile from x-ray diffraction is shown in Figure 4.29.

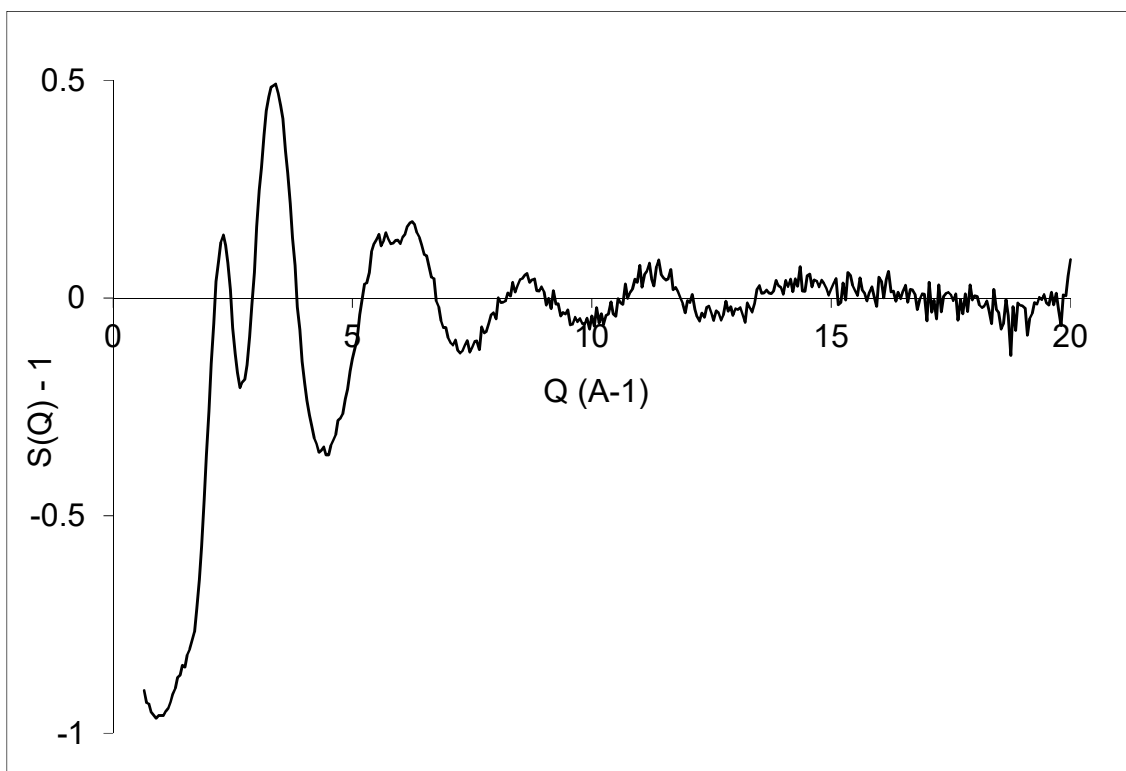


Figure 4.29 - X-ray structure factor profile of Mg-ACC150, obtained from the Elettra synchrotron, Italy

4.2.3.2 Extended X-ray Absorption Fine Structure (EXAFS)

At the EXAFS beamline at the ELETTRA synchrotron, Italy a sample of Mg-ACC150 was prepared in advance and studied together with pre-prepared crystalline standards of calcite, aragonite and monohydrocalcite (see Figures 4.30 and 4.31).

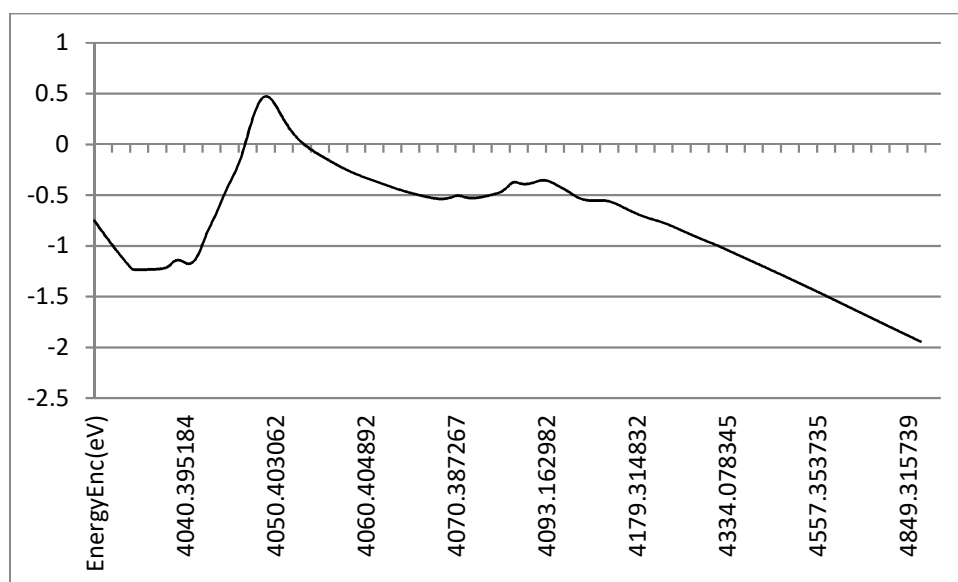


Figure 4.30 - EXAFS of Mg-ACC150, showing a peak at 4048 eV

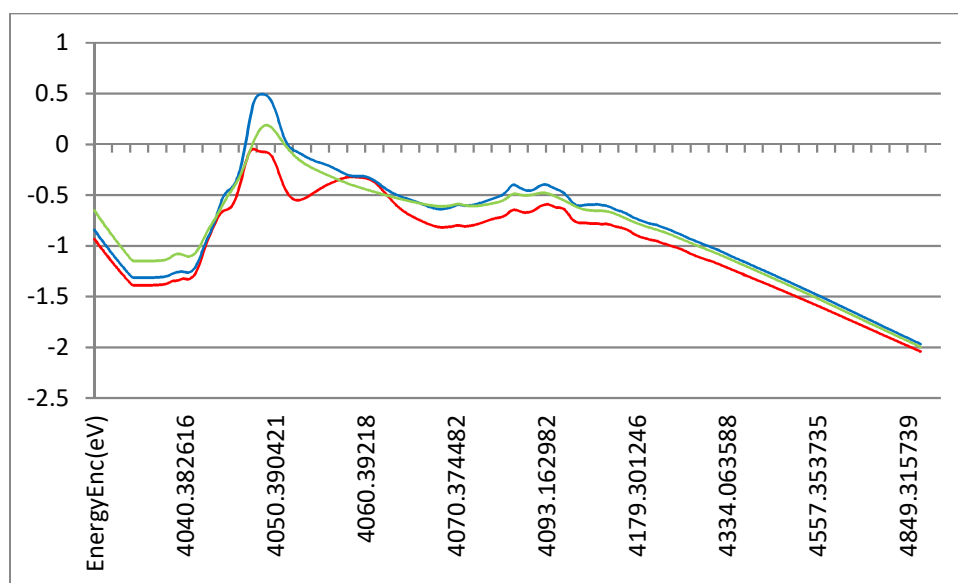


Figure 4.31 - EXAFS of reference samples - calcite (red), aragonite (blue) and monohydrocalcite (green)

4.2.3.3 *Neutron Scattering*

Neutron diffraction experiments were conducted on the SANDALS diffractometer^[108] at the ISIS pulsed neutron source, UK. The samples of Mg-ACC150 were prepared in advance the day before the experiment and loaded into a vanadium flat plate sample holder with 25 micron thick vanadium plate 4mm apart (figure 4.32 and 4.33).



Figure 4.32 - Empty flat plate vanadium sample holder with spacer (top left)



Figure 4.33 - Loaded flat plate vanadium sample holder.

The sample holder was sealed and maintained at a temperature of 5 °C during the experiment. Time-of-flight data (i.e. λ is a function of time) was collected over a wide range of up to Q of 30 \AA^{-1} (where $Q = 4\pi \sin \theta/\lambda$). The raw data was processed using the GUDRUN suite of programs.

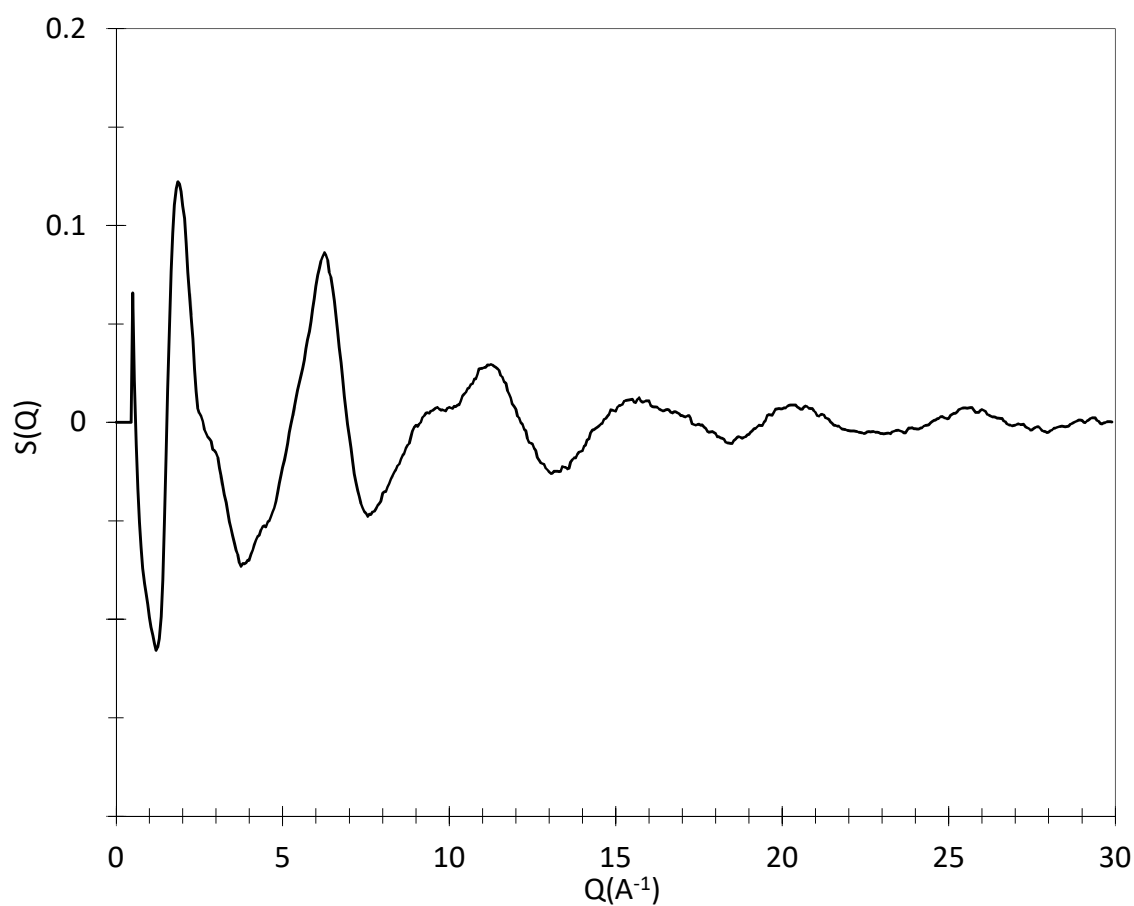


Figure 4.34 – $S(Q)$ profile for Mg-ACC150 from neutron diffraction.

4.2.4 EPSR Modelling

Structurally realistic molecular units were initially constructed using GHEMICAL4.0 software. A cubic box with length $L=39.55 \text{ \AA}$ containing 950 Ca, 50 Mg 1000 CO_3 and 250 D_2O units (total 5250

atoms) was assembled using the EPSR shell. This model corresponds to the measured density for Mg-ACC150 of 2.19 g/cm³.

Following the procedure detailed in section 3.2 yielded the following atomistic structure of Mg-ACC150:

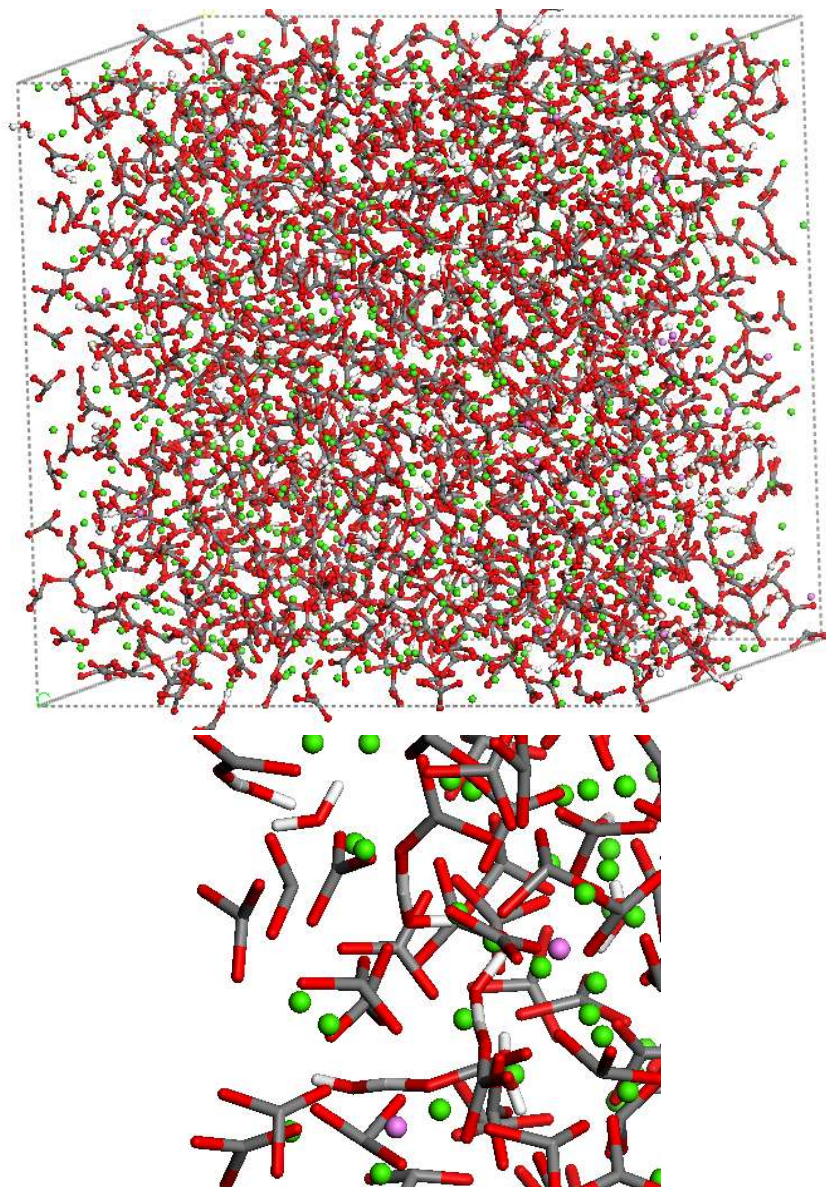


Figure 4.35 - Atomistic Structure of Mg-ACC150, calcium (green), magnesium (pink) oxygen (red), carbon (grey) and hydrogen (white). Below is the short range structure, zoomed in.

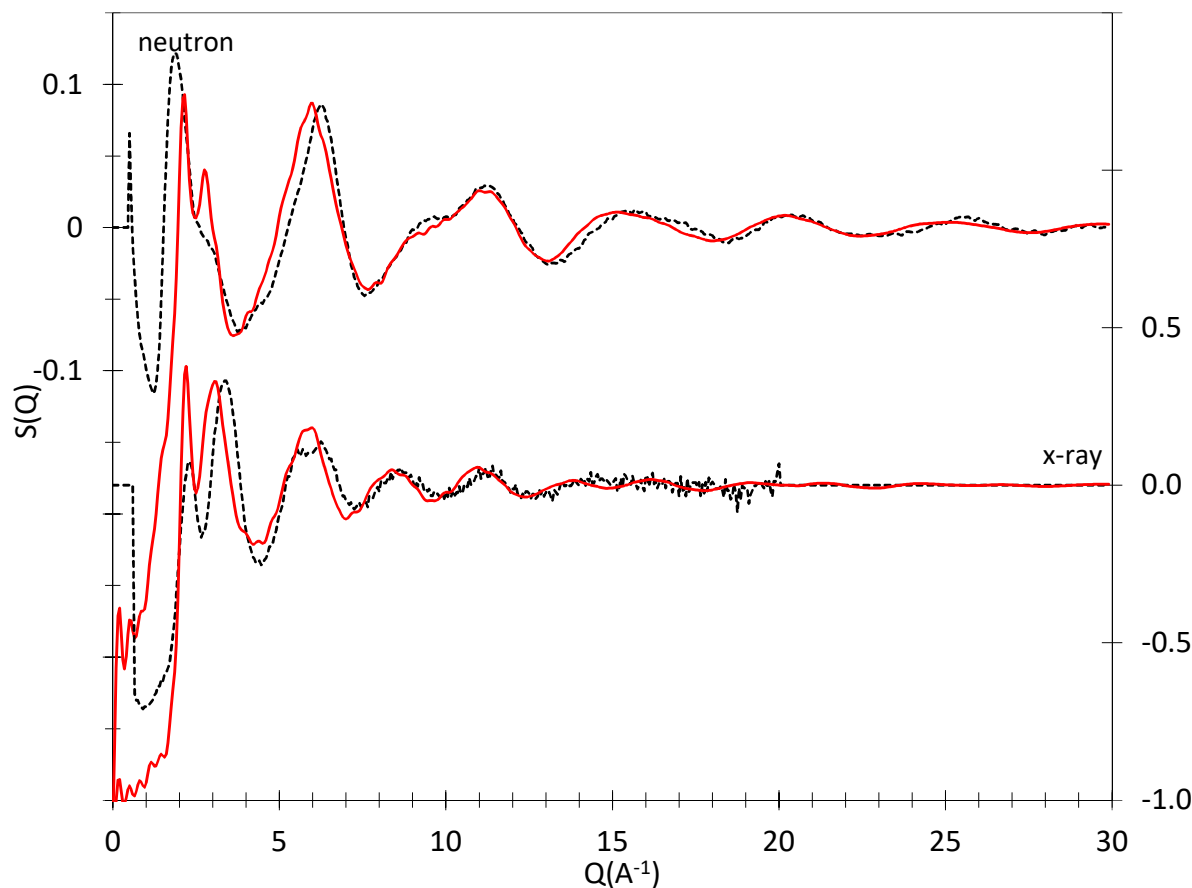


Figure 4.36 - Observed (black) and calculated (red) $S(Q)$ profiles for neutron and x-ray data of Mg-ACC150

At low Q , there is poor agreement with the experimental data and the computational model. The cause of this disparity is that the computational model was too highly constrained with regards to molecular ions. In future work, this issue could be addressed.

The pair distribution functions (PDF) $g_{ij}(r)$ have been calculated from the model using fourier transform. Figure 4.37 shows the PDFs involving CO_3 and H_2O molecular ions respectively. The first four peaks in the PDFs represent the internal structure of the molecules: O-H and H-H distances in H_2O , and C-O and O-O distances in CO_3 . There are inter-molecular (the interactions between different molecules and molecular units) and intra-molecular (the interactions within molecules or molecular units ie. C-O bond in CO_3 unit) correlations. These correlations and their peak distances are summarised in Table 4.5.

Table 4.5: interatomic correlations involving CO_3^- ions and H_2O molecular units. (* denotes correlations involving hydrogen bonding as discussed in the text.)

distance (Å) (approximate)	atoms types i-j	Molecular ion units	Coordination Number
0.93 and (1.2)*	H-O	intra and inter* H_2O	1.0 (1.0)
1.32	C-O	intra CO_3	3.0
1.56 and (1.9)*	H-H	intra and inter* H_2O	1.0 (0.6)
2.22	O-O	intra CO_3	2.0
(2.4)	C-H	inter CO_3 and H_2O	(0.7)
(2.8)	O-O	inter CO_3 (and H_2O)	N/A (large number of O at distances greater than 2.5 Å)
(3.3)	C-O	inter CO_3 (and H_2O)	N/A (large number of O at distances greater than 2.5 Å)
(3.5)	C-C	inter CO_3	5

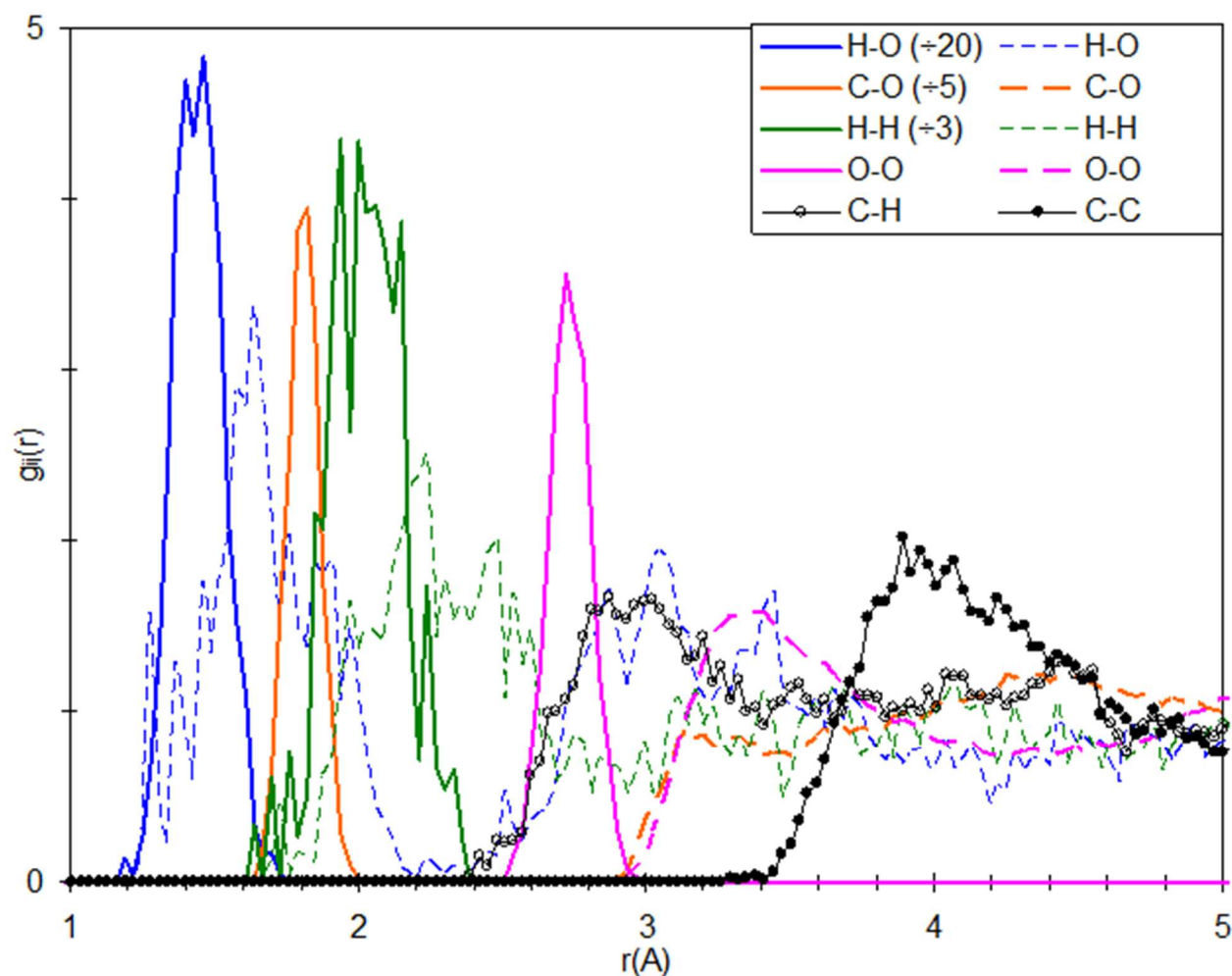


Figure 4.37 - Pair correlation functions $g_{ij}(r)$ involving CO_3^- and H_2O moieties for Mg stabilised ACC from EPSR model. (See Table 4.5 for details of the correlations and peak distances).

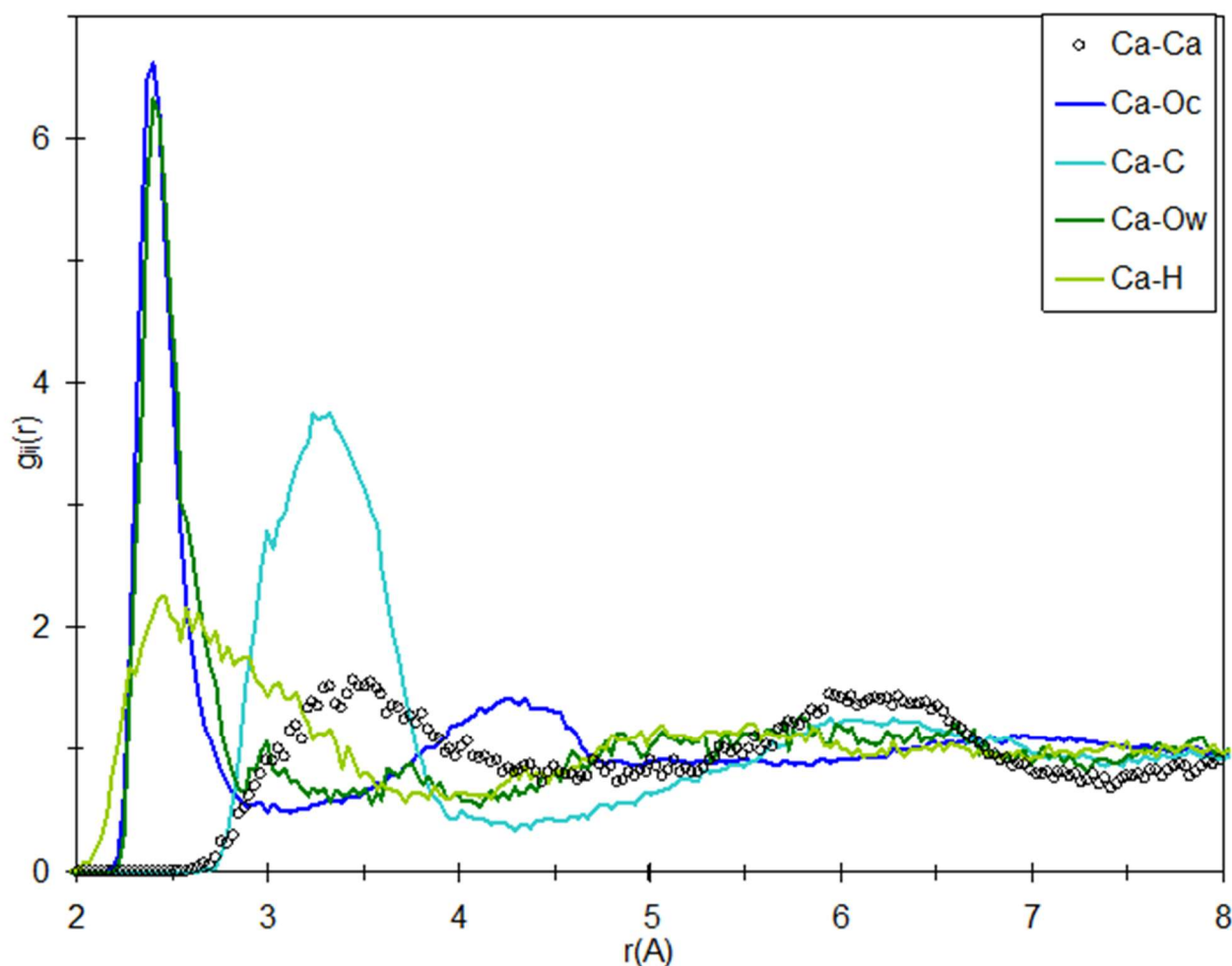


Figure 4.38 - Pair correlation functions $g_{ij}(r)$ involving Ca for Mg stabilised ACC from EPSR model. (Note Oc and Ow refer to oxygens in CO_3 and H_2O molecular ions respectively).

Figure 4.38 shows the PDFs involving Ca. Most prominent are the Ca-O distances due to Ca bonding to the oxygen atoms which are present in CO_3 and H_2O molecules, where the peak distance is 2.40 Å. The average coordination number of Ca is found to be 7.4 which are composed of 6.8 oxygen atoms from CO_3 molecules and 0.6 oxygen atoms from H_2O molecules. These features of the model are in good agreement with the EXAFS results of Michel et al^[17] for ACC prepared by a similar method, which were Ca-O coordination number of 6.7 ± 1.7 and peak distance of 2.41 ± 0.02 Å. Due to the coordination of Ca to oxygen in CO_3 and H_2O molecules, there are consequently noticeable correlations of Ca...C and Ca...H. The PDFs for Mg are similar to those for Ca, but they are not presented in detail because of the poor statistics due to the small number of Mg atoms in the model.

The first peak at 3.3-4.5 Å in the Ca-Ca PDF (see Figure 4.2.4) corresponds to calcium which share bonds with common oxygen, i.e. Ca-O-Ca.

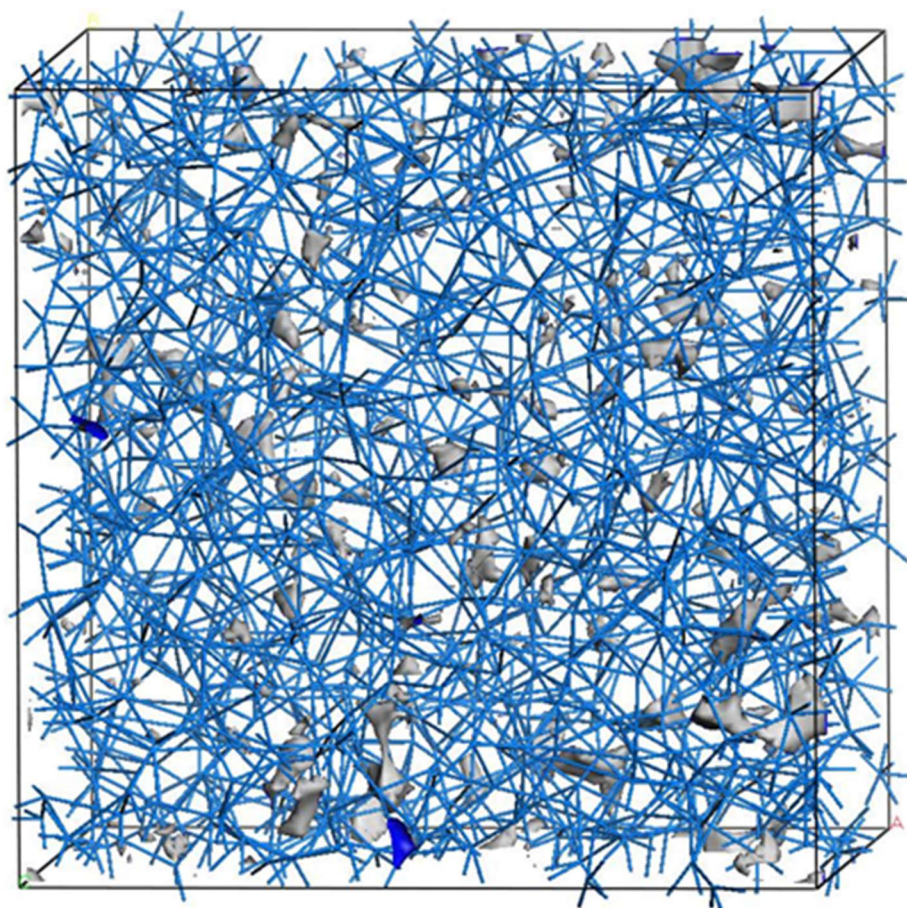


Figure 4.39: EPSR model of Mg-stabilised ACC (figure 4.35) with blue lines showing the Ca-rich network as blue sticks (i.e. Ca-O-Ca linkages). Marginal volumes of Ca-poor channels (based on the criteria of regions more than 3.3 Å distant from Ca) are shown as grey surfaces. (None are present using a criteria of 4 Å.) A similar analysis was reported by Goodwin et al ^[27].

Figure 4.39 (blue lines) shows that the "Ca-rich network" (based on Ca-O-Ca linkages) is homogeneously distributed. In addition there are no Ca-poor channels based on the criteria of regions more than 4 Å distant from Ca. Figure 4.39 (grey surfaces) shows that when using a less stringent definition of Ca-poor channels based on the criteria of regions more than 3.3 Å distant from Ca there are only a few marginal volumes fitting these criteria.

4.3 Amorphous Magnesium Carbonate (AMC)

4.3.1 Synthesis

Based on the method developed to produce ACC and Mg-ACC, samples of amorphous magnesium carbonate (AMC) were produced. Simply by omitting calcium chloride solution and increasing the volume of magnesium carbonate solution. The table below illustrates the stock solutions used

Table 4.6 – Stock solution preparation for AMC synthesis

Concentration of Stock Solution (mM)	Reagent	Mass (g)	Volume of Stock Solution (mL)
100	Magnesium Chloride (MgCl ₂)	9.521	1000
100	Sodium Carbonate (Na ₂ CO ₃)	14.204	1000

To prepare AMC, 10 mL of the 100 mM solutions of MgCl₂ and Na₂CO₃ were transferred to separate polypropylene tubes. The MgCl₂ solution was added and this was then rapidly mixed with the Na₂CO₃ solution. This mixing produced a white precipitate in a Millipore™ glass filtration kit before being rapidly filtered through a Cyclopore® 0.2 µm pore size, track-etched polycarbonate membrane filter (47 mm diameter) and washed with isopropanol and dried in flowing air.

For this chapter of work, both a deuterated and heat-treated sample of AMC were produced using methods detailed in chapters 4.1 and 4.2 respectively. A list of potential samples was devised and is as follows:

- AMC_{unh} - unheated sample
- AMC₁₀₀ - heated to 100°C for 1 hour
- AMC₂₀₀ - heated to 200°C for 1 hour
- AMC₃₀₀ - heated to 300°C for 1 hour

4.3.2 Lab-based characterisation

4.3.2.1 Lab Powder X-ray Diffraction (XRD)

The heat-treated and unheated samples of AMC were analysed by XRD immediately after synthesis to determine which were amorphous.

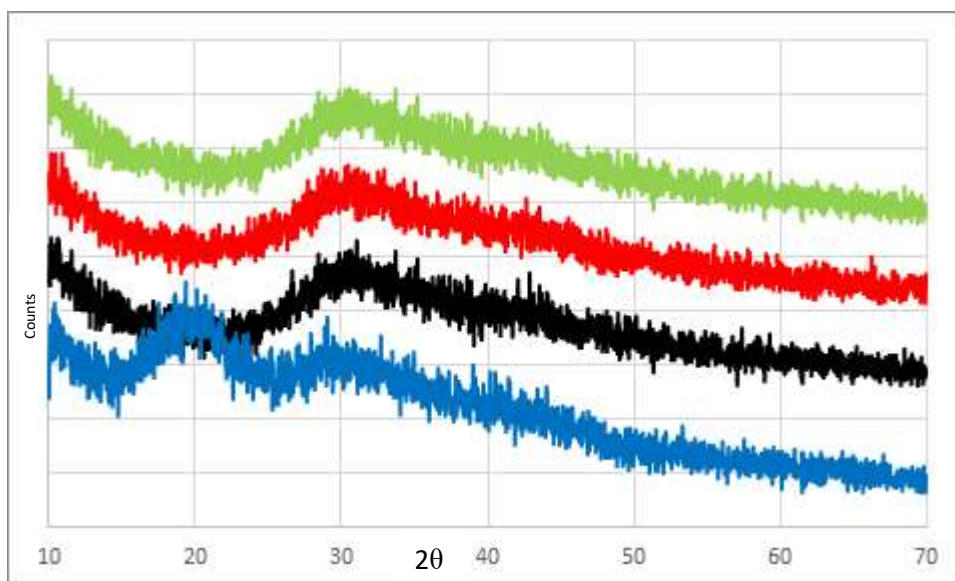


Figure 4.40 - XRD patterns of freshly prepared AMCunh (blue), AMC100 (black), AMC200 (red), AMC300 (green)

With the exception of AMC300, which was crystalline immediately after heat treatment, the above samples were kept sealed in a 5 mL glass bottle secured with lab film and re-measured at varying intervals (1, 3, 7 and 14 days after synthesis). Fig 4.41 shows the results over time for sample AMC200

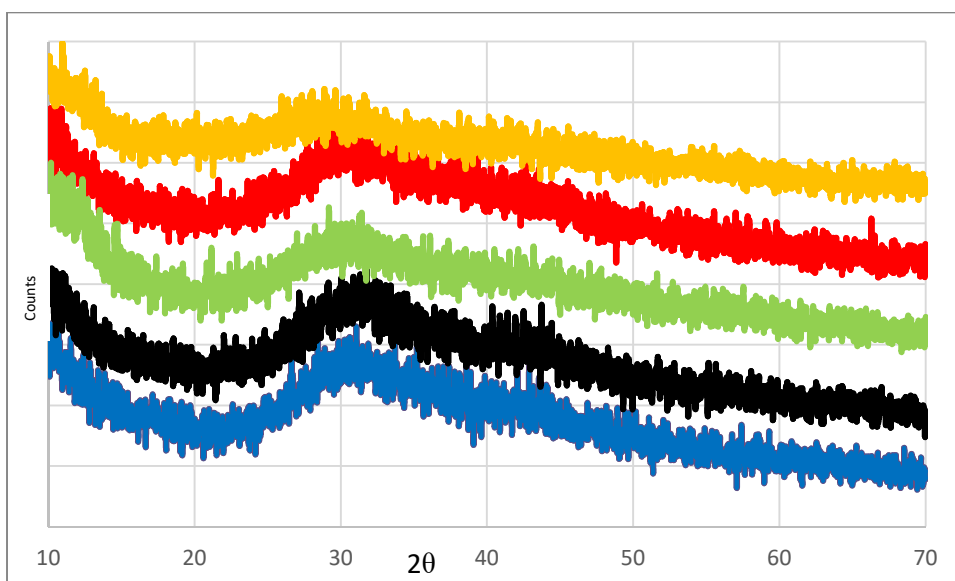


Fig 4.41 – XRD patterns for AMC200 over time from 0 days (blue), 1 day (black), 3 days (red), 7 days (green) and 14 days (orange) after heat treatment

The AMC200 sample was amorphous for longer than two weeks which was ideal for central facility experiments. All further work in this chapter will be based, on AMCunh (in preparation for synthesis of D-AMC) and AMC200.

4.3.2.2 *Thermo-Gravimetric Analysis (TGA)*

A sample of freshly prepared AMCunh was analysed using TGA-DTA and the results are shown in figure 4.42 and 4.43.

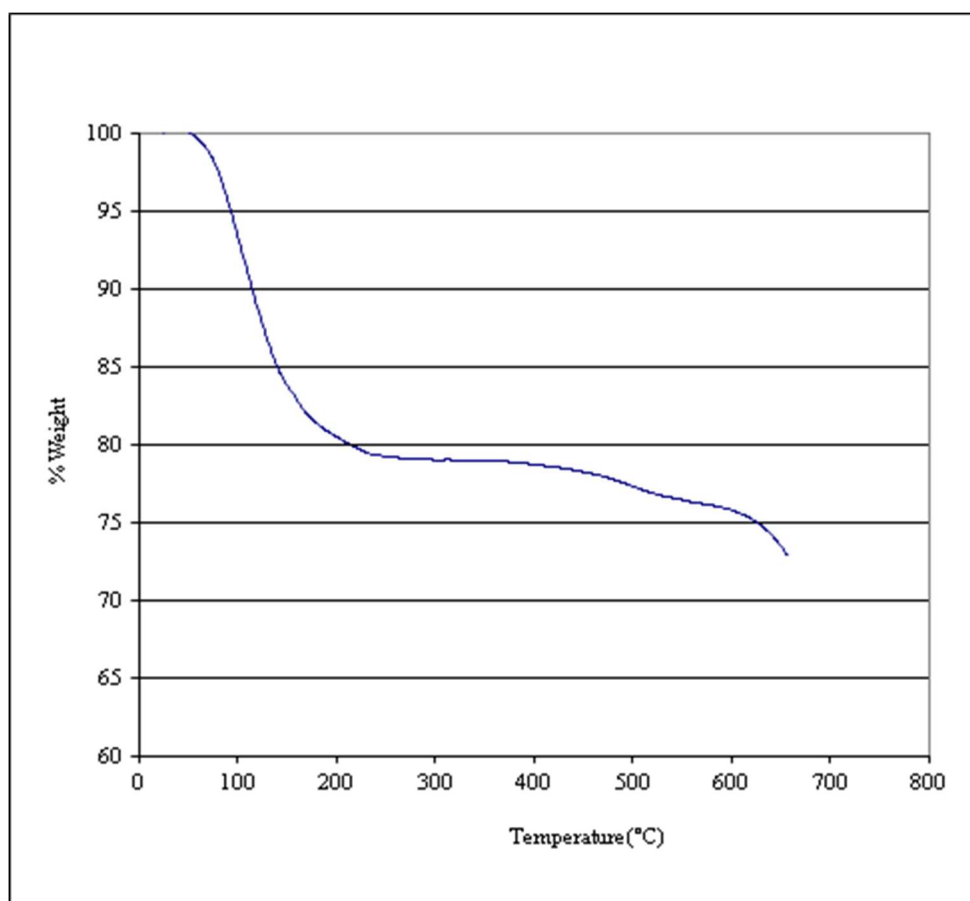


Figure 4.42 – TGA of AMCunh, showing weight loss of 20% up to approximately 200°C and 23% to 400°C at which point AMCunh crystallises (see figure 4.43).

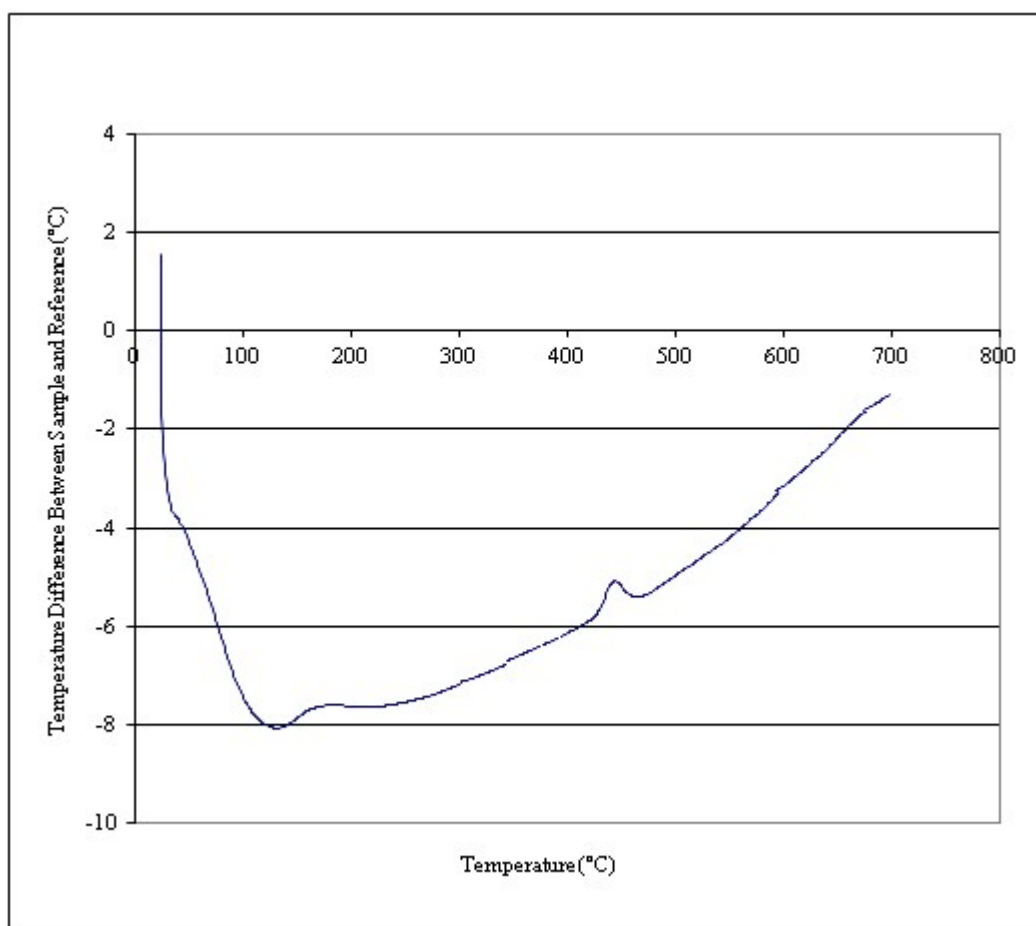


Figure 4.43 – DTA of AMCuNh showing a crystallisation peak at approximately 400°C

The TGA-DTA of Mg-ACCunh1 showed weight losses of 20% and 24% up to temperatures of 200 °C and 400 °C respectively, the latter being when magnesite crystallises. These weight losses are consistent with a water content of $n=1.55$ before and $n=0.2$ after heat treatment at 200 °C. For the EPSR models, D-AMC will have a D₂O content corresponding to $n=1.55$ and AMC200 will have H₂O equal to $n=0.2$.

4.3.2.3 Helium Micropycnometry

Samples of AMCuNh AMC200 was loaded into a small aluminium can which was then placed into the He-pycnometer and this was left to purge with helium for approximately 10 minutes before operation could begin. This operation was performed on-site at the ISIS neutron facility approximately 2 weeks after the completion of the neutron experiments due to the magnesium in the AMC200 sample being radioactive immediately after completion of the experiment. The values of P1 and P2 were recorded in an Excel spreadsheet before correcting using the sample mass and container mass (all within Excel), figure 4.28 shows the P1/P2 ratio for AMCuNh and AMC200.

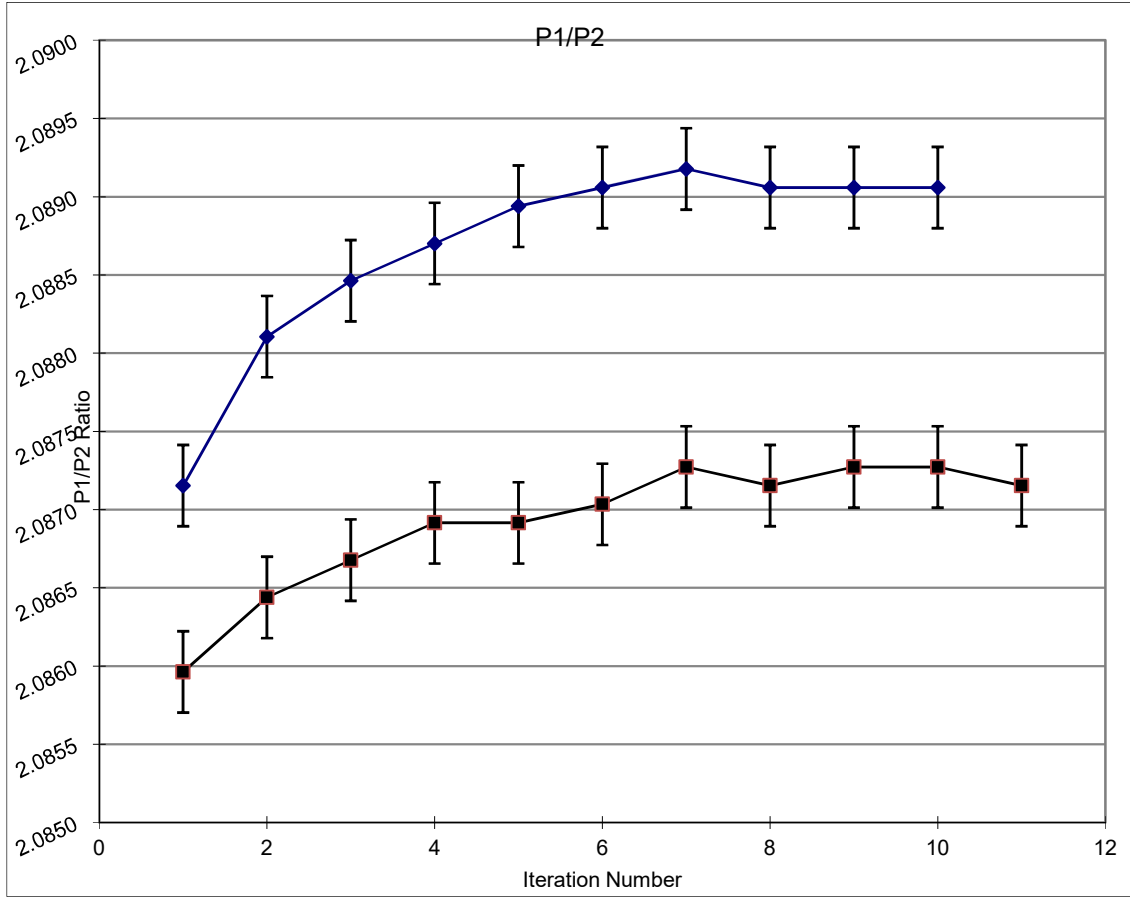


Figure 4.44 - He-pycnometry of AMCUH (blue) and AMC200 (black) samples showing the P1/P2 ratio, the procedure was repeated until the recorded density was within acceptable limits (1 s.d. - black error bar)

The density of AMCUH was calculated as 2.46 g/cm³ and 2.32 g/cm³ for AMC200 using the results for P1/P2 obtained from a He pycnometer. This density will be used in the EPSR model for D-AMC AMC200.

4.3.3 Central Facility Experiments

4.3.3.1 Synchrotron X-ray Powder Diffraction

X-ray diffraction data were collected at the MCX diffractometer^[107] at the ELETTRA synchrotron, Italy, using a wavelength of $\lambda=0.620$ Å. The sample was produced prior to travelling to the synchrotron and sealed until it was loaded into a 10 micron thick 1.5 mm diameter silica capillary. The capillary was rotated during the experiment. X-ray diffraction data was collected up to 2θ of 120° or $Q=20$ Å⁻¹. The processing of the raw data included corrections for the background scattering, polarization, sample thickness, absorption, capillary, Compton scattering, and the sharpening function (equal to the square of the average form factor per atom). The structure factor $S(Q)$ profile from x-ray diffraction is shown in figure 4.45.

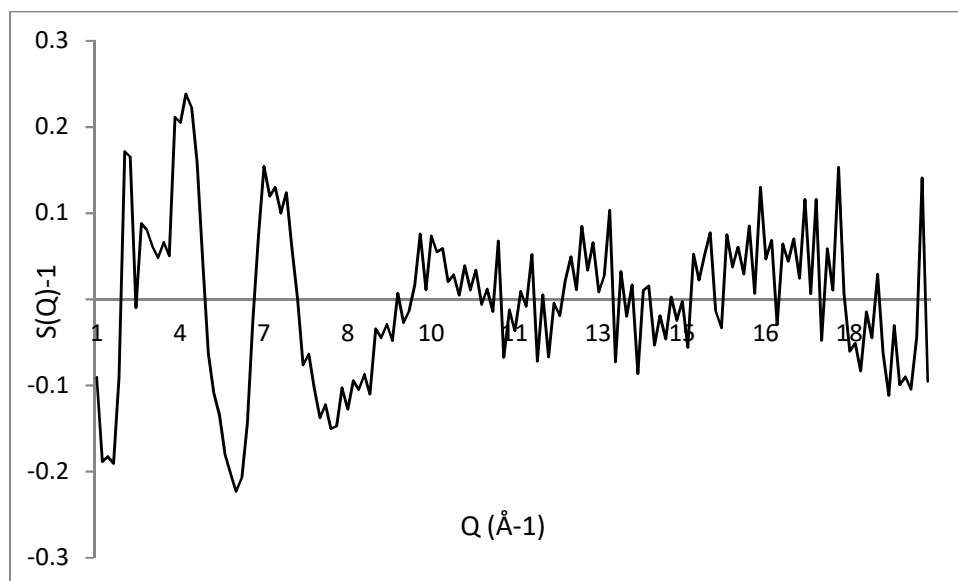


Figure 4.45 Structure factor $S(Q)$ from x-ray diffraction for AMCu₂Nh

Unfortunately due to complications at the Elettra synchrotron with crystallisation and lack of time/reagents/facilities to reproduce a sample of AMC200 it was not possible to gather XRD data on AMC200.

4.3.3.2 Neutron Scattering

Neutron diffraction data were measured using the SANDALS diffractometer^[108] at the ISIS pulsed neutron source, UK. The deuterated samples were produced on the day of the experiment and loaded into a flat plate holder sample holder with 25 micron thick TiZr plate 4mm apart (figure 4.13)

Samples of AMC200 were produced prior to travelling to ISIS and were loaded into into a vanadium flat plate sample holder with 25 micron thick vanadium plate 4mm apart (figure 4.32 and 4.33).

The sample holders were sealed and maintained at a temperature of 5 °C during the experiment. Time-of-flight data (i.e. λ is a function of time) was collected over a wide range of up to Q of 30 Å⁻¹ (where $Q = 4\pi \sin \theta/\lambda$). The raw data were processed using the GUDRUN suite of programs.

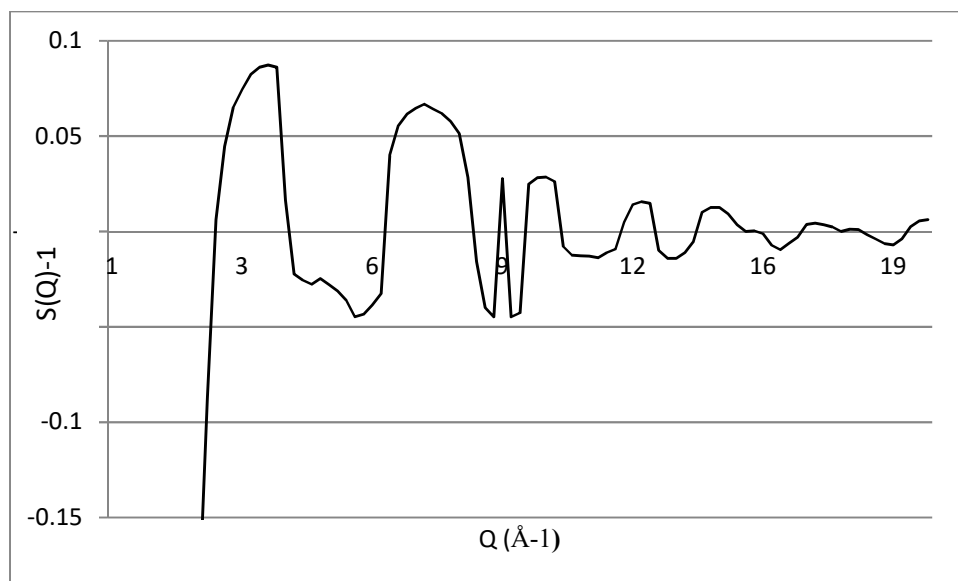


Figure 4.46 - S(Q) profile from neutron diffraction data for D-AMC

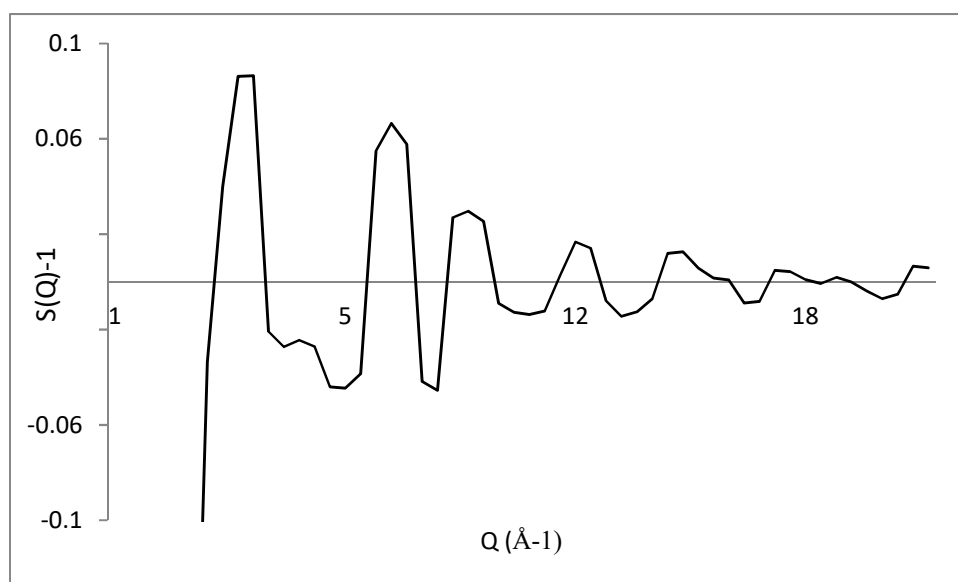


Figure 4.47 - S(Q) profile from neutron diffraction data for AMC200

4.3.4 Empirical Potential Structure Refinement (EPSR) Modelling

Structurally realistic molecular units were initially constructed using GHEMICAL4.0 software. A cubic box with length $L=42.60 \text{ \AA}$ containing 1000 Mg, 1000 CO_3 and 1550 D_2O units (total 8650 atoms) for D-AMC and a box of length $L=38.95 \text{ \AA}$ containing 1000 Mg, 1000 CO_3 and 200 H_2O units (total 4600 atoms) for AMC200 was assembled using the EPSR shell. These models corresponds to the measured density for AMC of 2.46 g/cm^3 and 2.32 g/cm^3 for AMC200.

This procedure yielded the following atomistic structure of D-AMC and AMC200:

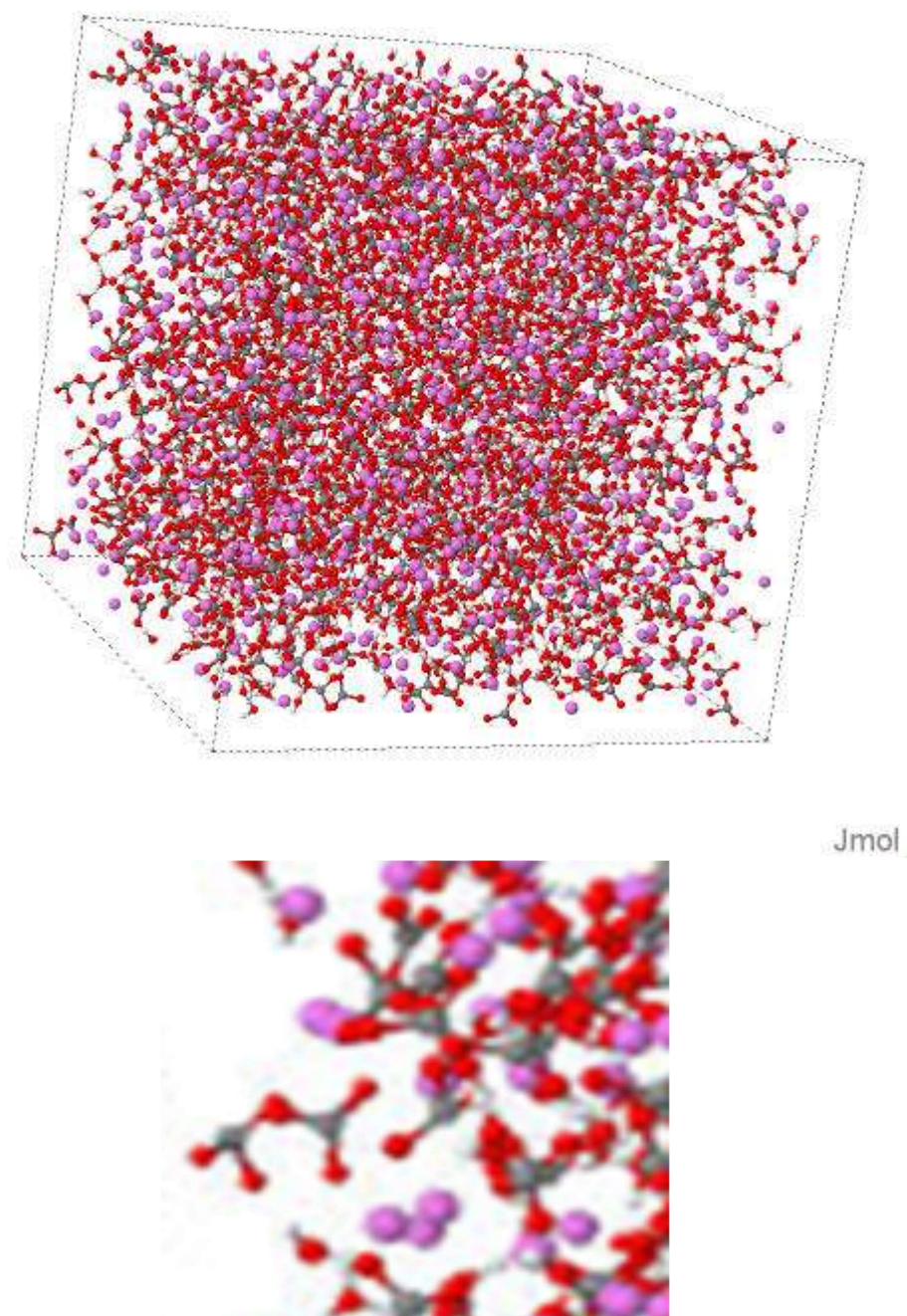


Figure 4.48 - Atomistic Structure of D-AMC, magnesium (pink), oxygen (red), carbon (grey) and deuterium (white). Below is the short range structure zoomed in

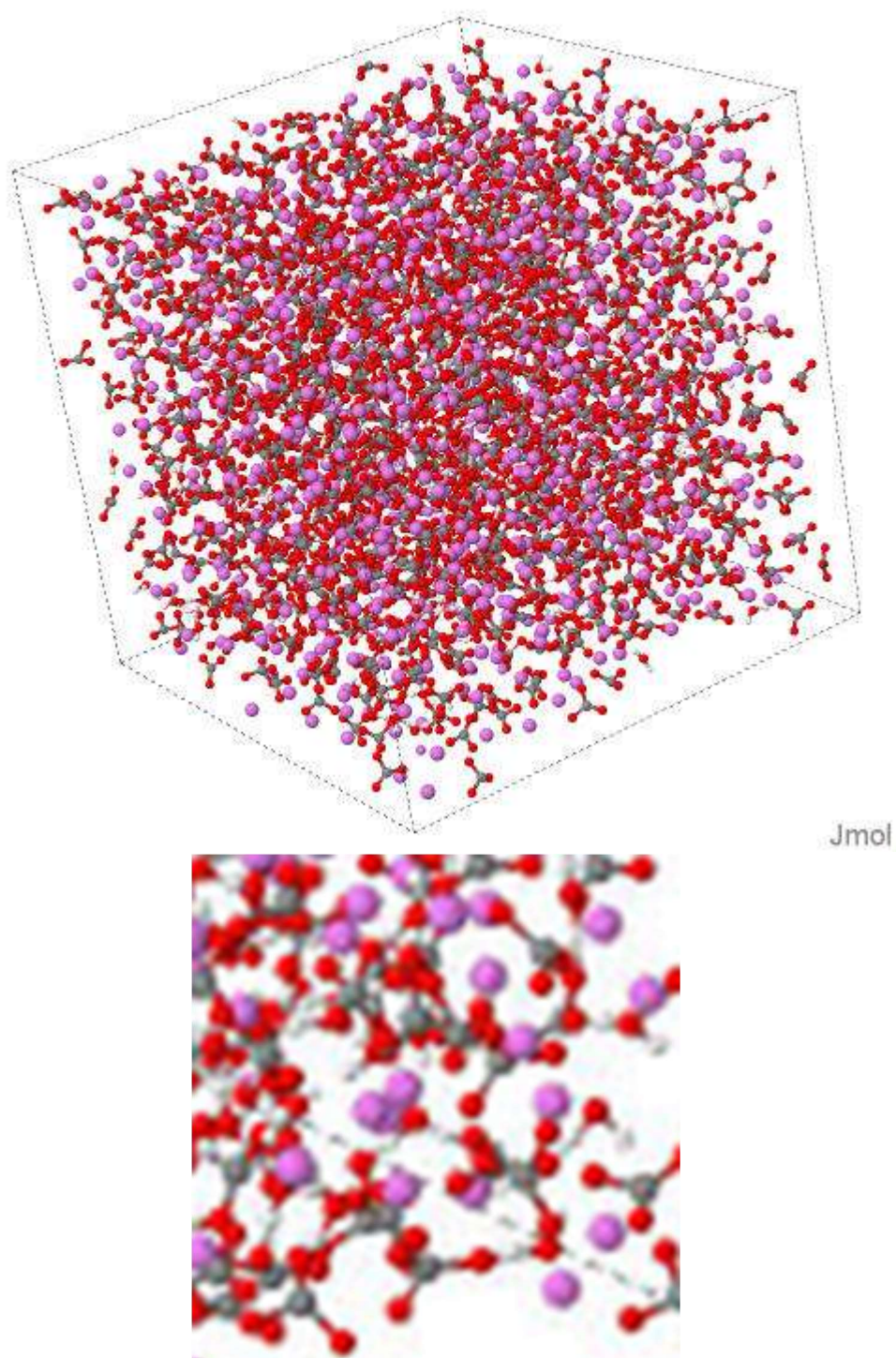


Figure 4.49 - Atomistic Structure of AMC200, magnesium (pink), oxygen (red), carbon (grey) and hydrogen (white). Below is the short range structure zoomed in

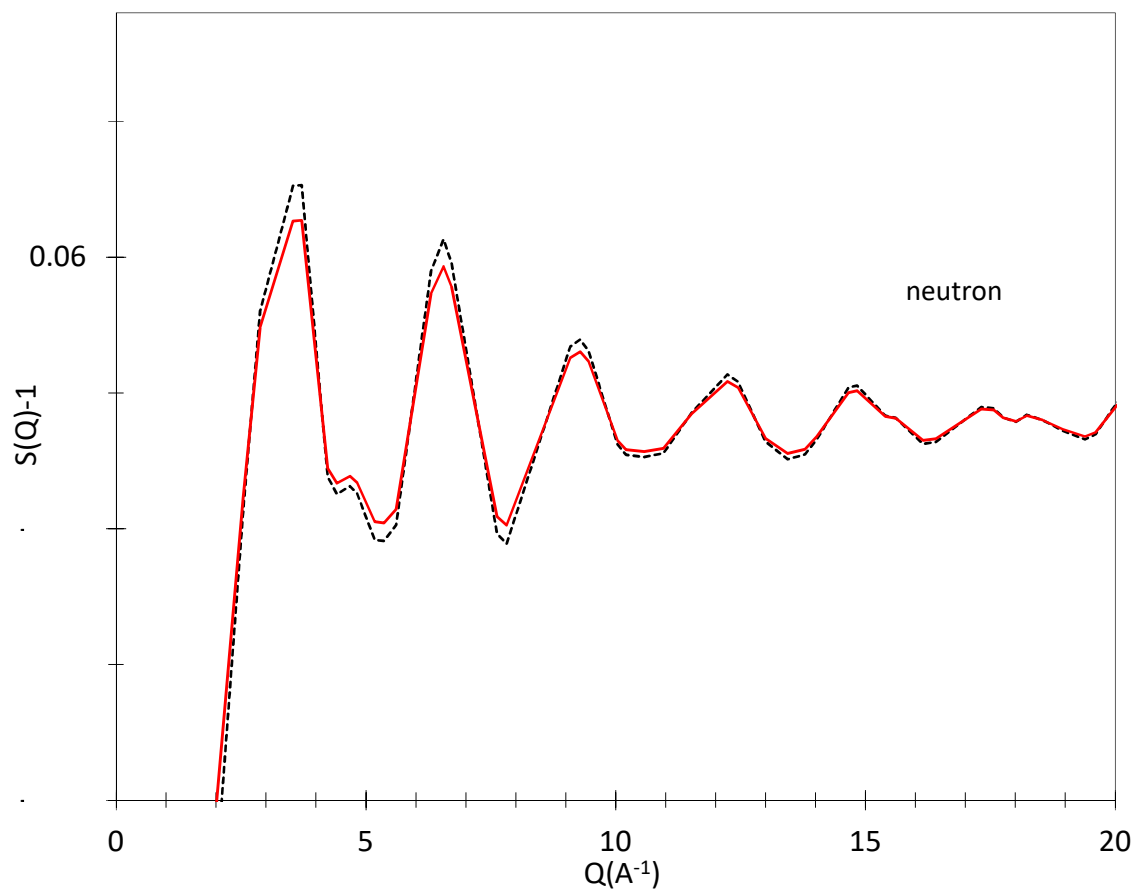


Figure 4.50 - Fitted $S(Q)$ profile from neutron diffraction data for D-AMC, showing observed (black) and calculated (red) profiles.

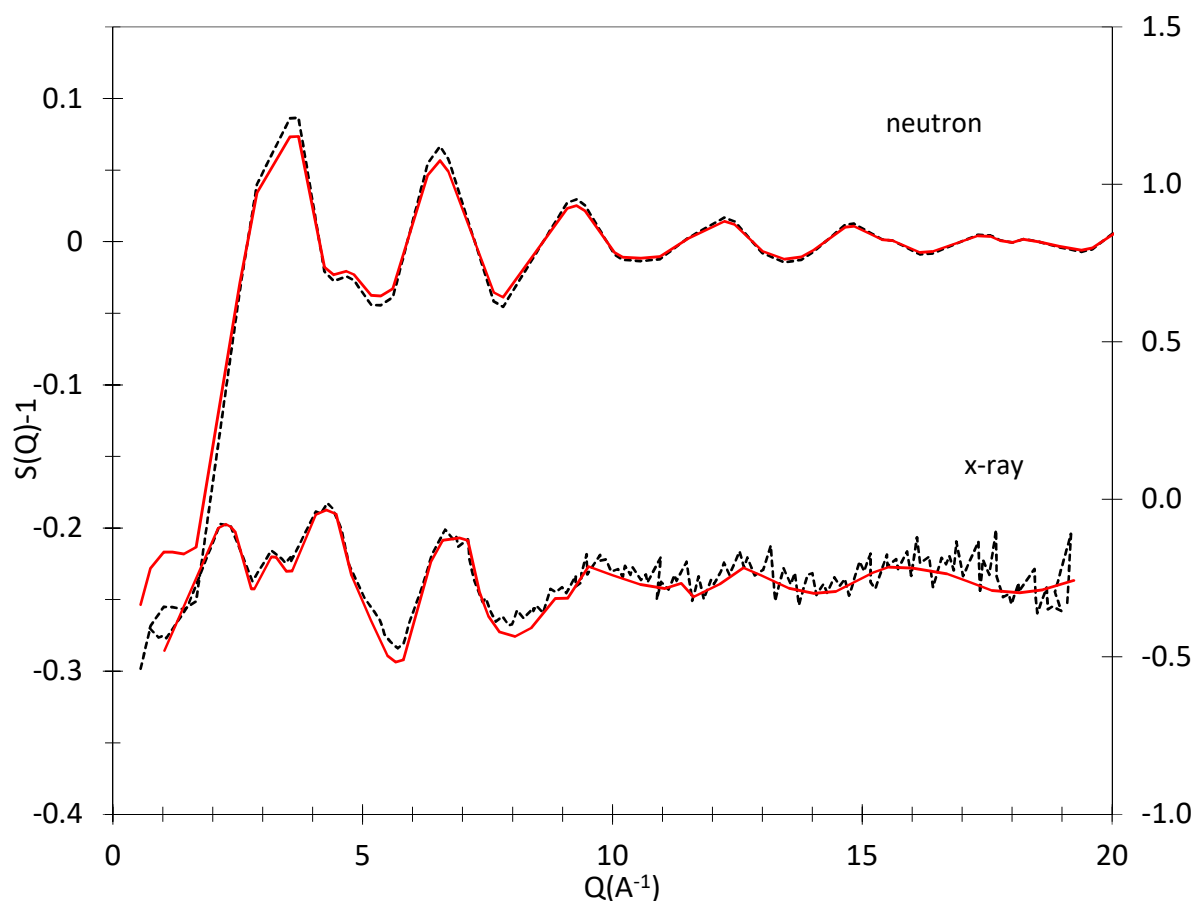


Figure 4.51 - Fitted $S(Q)$ profile from neutron and x-ray diffraction data for AMC200 showing observed (black) and calculated (red) profiles.

Individual pair correlation functions $g_{ij}(r)$ were calculated and those involving CO_3^- ions and H_2O molecules are shown in Figure 4.52. The first four peaks in the PDFs represent the internal structure of the molecules: O-H and H-H distances in H_2O , and C-O and O-O distances in CO_3 . There are inter-molecular (the interactions between different molecules and molecular units) and intra-molecular (the interactions within molecules or molecular units ie. C-O bond in CO_3 unit) correlations. These correlations and their peak distances are summarised in Table 4.7.

Table 4.7 - Interatomic correlations involving CO_3^- ions and H_2O molecular units. (* denotes correlations involving hydrogen bonding)

distance (Å) (approximate)	atoms types i-j	Molecular ion units	Coordination Number
0.92 and (1.3)*	H-O	intra and inter* H_2O	1.0 (1.0)
1.34	C-O	intra CO_3	2.9
1.57 and (1.9)*	H-H	intra and inter* H_2O	1.0 (0.5)
2.21	O-O	intra CO_3	2.0
(2.5)	C-H	inter CO_3 and H_2O	(0.6)
(2.8)	O-O	inter CO_3 (and H_2O)	N/A (large number of O at distances greater than 2.5 Å)
(3.3)	C-O	inter CO_3 (and H_2O)	N/A (large number of O at distances greater than 2.5 Å)
(3.6)	C-C	inter CO_3	5

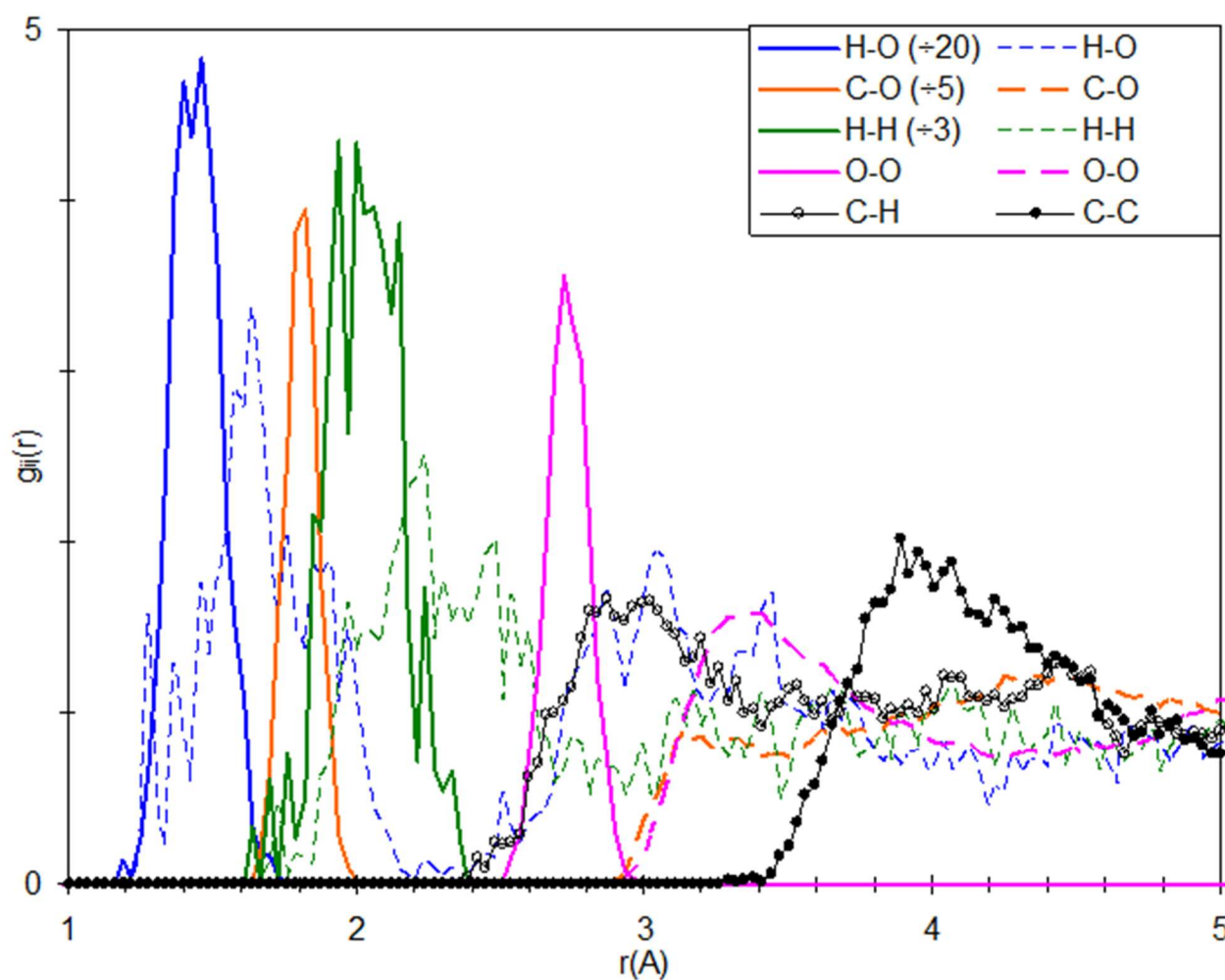


Figure 4.52 - Pair correlation functions $g_{ij}(r)$ involving CO_3^- ions and H_2O moieties for D-AMC from EPSR model. (See Table 4.7 for details of the correlations and peak distances).

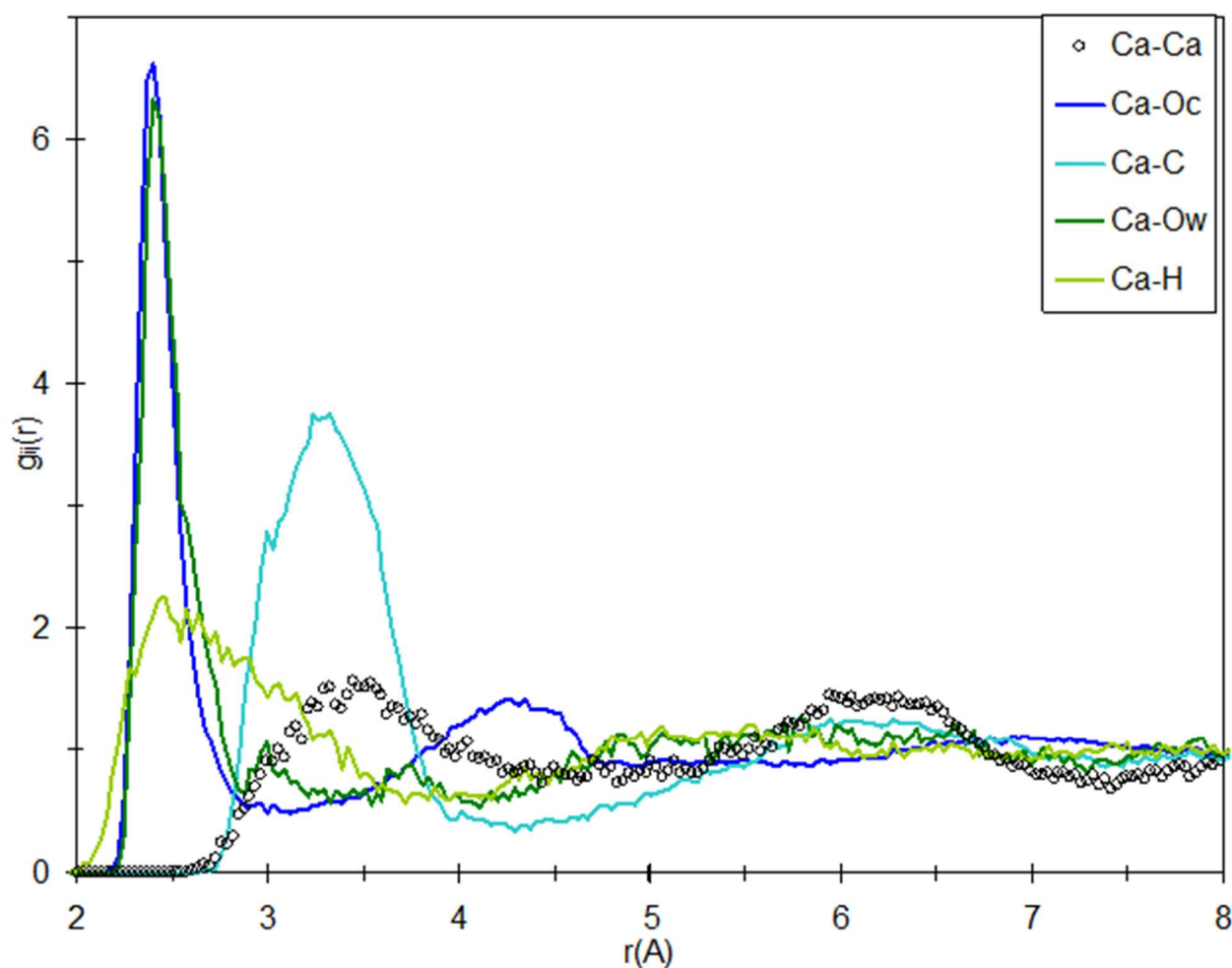


Figure 4.53 - Pair correlation functions $g_{ij}(r)$ involving Ca for D-AMC from EPSR model. (Note Oc and Ow refer to oxygens in CO_3 and H_2O molecules respectively).

Figure 4.53 shows the pair correlations involving magnesium. Most prominent are the Mg-O distances due to Mg bonding to the oxygen atoms which are present in CO_3 and H_2O molecules, where the peak distance is 2.42 Å. The average coordination number of Mg is found to be 7.0 which are composed of 6.4 oxygen atoms from CO_3 molecules and 0.6 oxygen atoms from H_2O molecules. Due to the coordination of Mg to oxygen in CO_3 and H_2O molecules, there are consequently noticeable correlations of Mg...C and Mg...H.

The first peak at 3.3-4.5 Å in the Mg-Mg PDF (see Figure 4.53) corresponds to magnesium which share bonds with common oxygen, i.e. Mg-O-Mg.

4.4 Amorphous Phosphates

4.4.1 Amorphous Calcium Phosphate (ACP)

This area of study builds on a previous project conducted by K. Wetherall^[110] in which heat treated samples of amorphous calcium phosphate (ACP) were studied using x-ray and neutron diffraction. The work in this project was two fold - computational modelling of the existing data and of the new dataset for a deuterated sample of ACP which was produced and data gathered during this work.

4.4.1.1 Synthesis

Heat treated samples of ACP were produced by K. Wetherall^[110] using a similar method to the other materials in this project. The freshly prepared samples were heat treated for approximately one hour with the ideal sample being ACP450, ACP being heated to 450°C, this sample contains very little hydrogen and was stable for a period greater than 2 weeks.

For this project, the author, prepared deuterated samples of ACP where all synthesis work was conducted in an argon gas chamber at the ISIS facility, Didcot. Deuterated ACP (D-ACP), was prepared with 10 mL of the 100 mM D₂O solutions of CaCl₂ and Na₃PO₄ were transferred to separate polypropylene tubes. The CaCl₂ solution was rapidly mixed with the Na₃PO₄ solution. This mixing produced a white precipitate in a Millipore™ glass filtration kit before being rapidly filtered through a Cyclopore® 0.2 µm pore size, track-etched polycarbonate membrane filter (47 mm diameter) and washed with isopropanol-d8 and dried in flowing argon (via use of a small portable electric fan).

4.4.1.2 Lab-based characterisation

4.4.1.2.1 Lab Powder X-ray Diffraction (XRD)

The deuterated sample, D-ACP was measured after the experiments at the ISIS neutron facility and was found to still be amorphous.

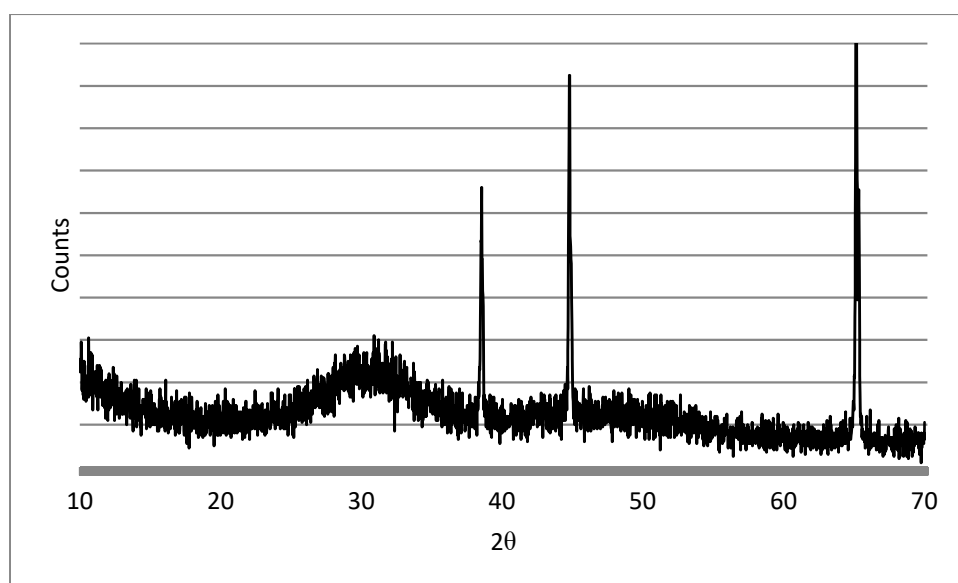


Figure 4.54 - XRD pattern of D-ACP obtained after neutron diffraction experiment.

4.4.1.2.2 Helium Micropycnometry

The density of ACP-450 were measured to be 2.39 g/cm³ using a He pycnometer by K. Wetherall^[110] and the sample of D-ACP was found to have a density of 2.47 g/cm³ by the author. Both of these density measurements will be used to construct EPSR models

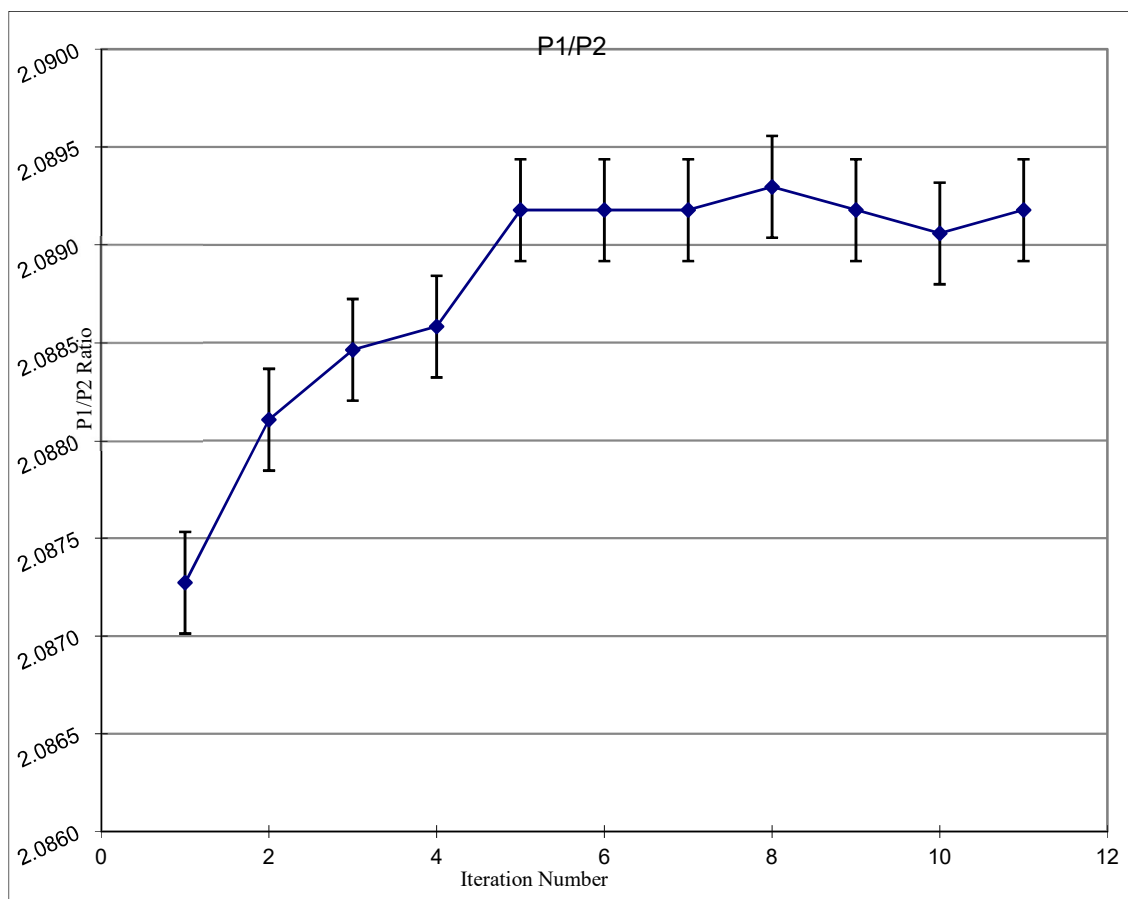


Figure 4.55 - He-pycnometry of D-ACP sample showing the P1/P2 ratio, the procedure was repeated until the recorded density was within acceptable limits (1 s.d. - black error bar)

4.4.1.3 Central Facility Experiments

4.4.1.3.3 Neutron Scattering

Neutron diffraction data were measured using the SANDALS diffractometer^[108] at the ISIS pulsed neutron source, UK. The ACP-450 sample data was collected by K. Wetherall during the previous project. The sample, named D-ACP, was prepared on-site (using the method detailed in section 4.1) immediately before being placed in the beam. This sample was loaded into a flat plate holder sample holder with 25 micron thick TiZr plate 4mm apart (figure 4.13).

The sample holder was sealed and maintained at a temperature of 5 °C during the experiment by the author. Time-of-flight data (i.e. is a function of time) was collected over a wide range of up to Q of 30 \AA^{-1} (where $Q = 4\pi \sin \theta/\lambda$). The raw data was processed using the GUDRUN suite of programs.

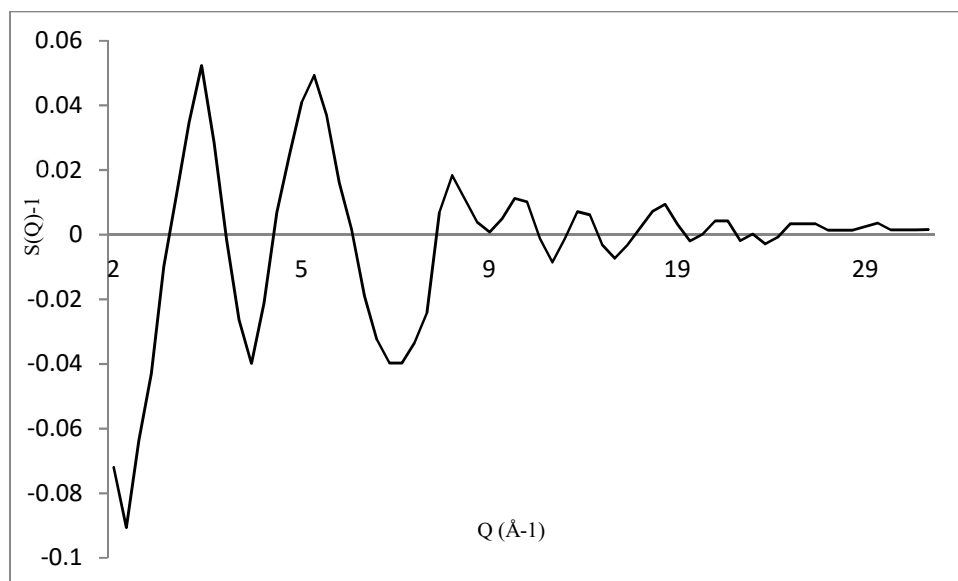


Figure 4.56 - Structure factor $S(Q)$ profile from neutron diffraction of D-ACP

4.4.1.4 Empirical Potential Structure Refinement (EPSR) Modelling

Structurally realistic molecular units were initially constructed using GHEMICAL4.0 software. A cubic box with length $L=40.01 \text{ \AA}$ containing 1000 Ca, 1000 PO_4 and 500 H_2O units was assembled using the EPSR shell. This model corresponds to the measured density for ACP-450 of 2.39 g/cm^3 . In the case of D-ACP, a cubic box with length $L=42.12 \text{ \AA}$ containing 1000 Ca, 1000 PO_4 and 1500 D_2O units was assembled using the EPSR shell with a density of . This model corresponds to the measured density for ACP-450 of 2.47 g/cm^3 .

Following the procedure detailed in section 3.2 yielded the following atomistic structure of ACP-450 and D-ACP:

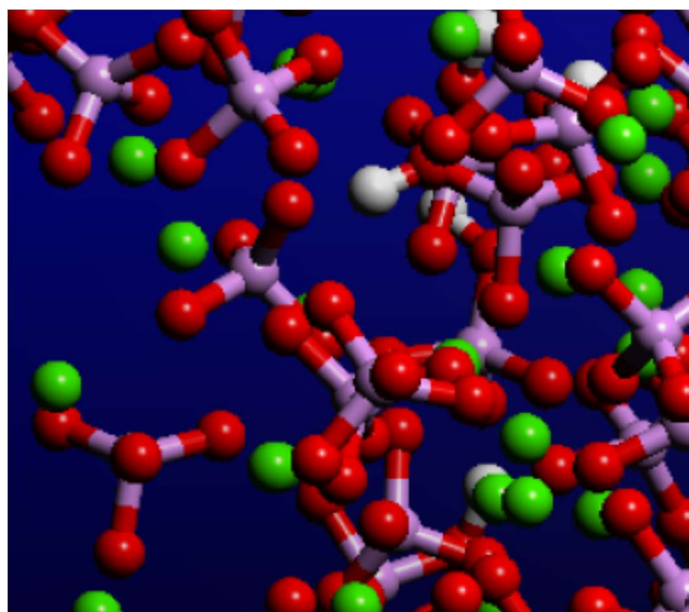
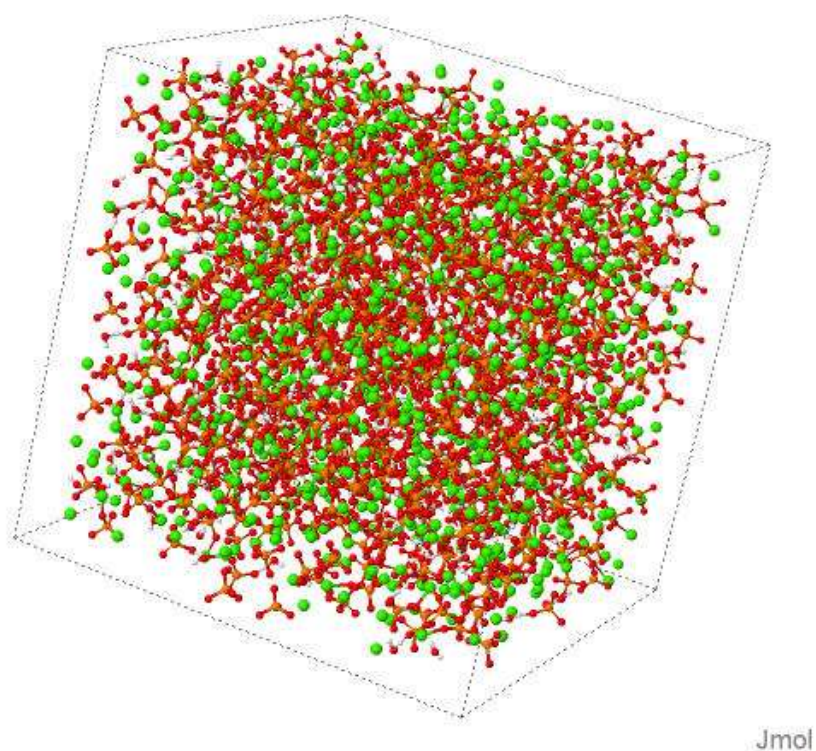


Figure 4.57 - Atomistic Structure of ACP-450, calcium (green), oxygen (red), phosphorous (orange/pink) and hydrogen (white). Below is the short range structure zoomed in.

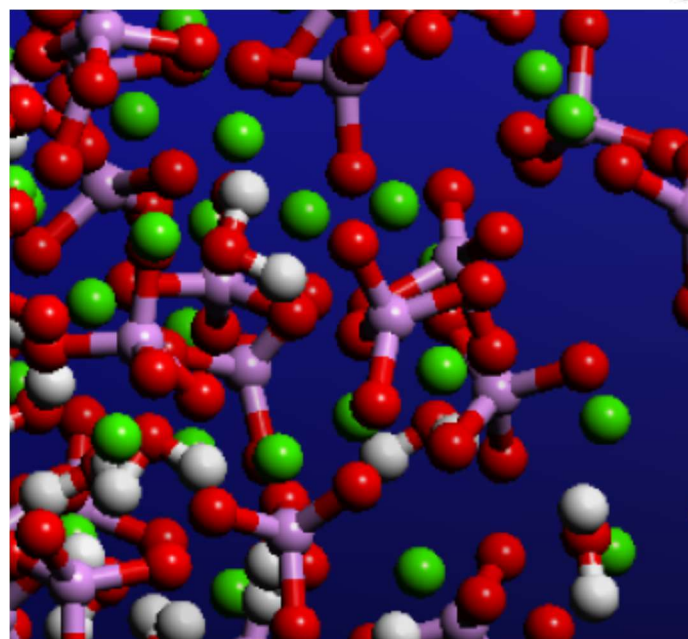
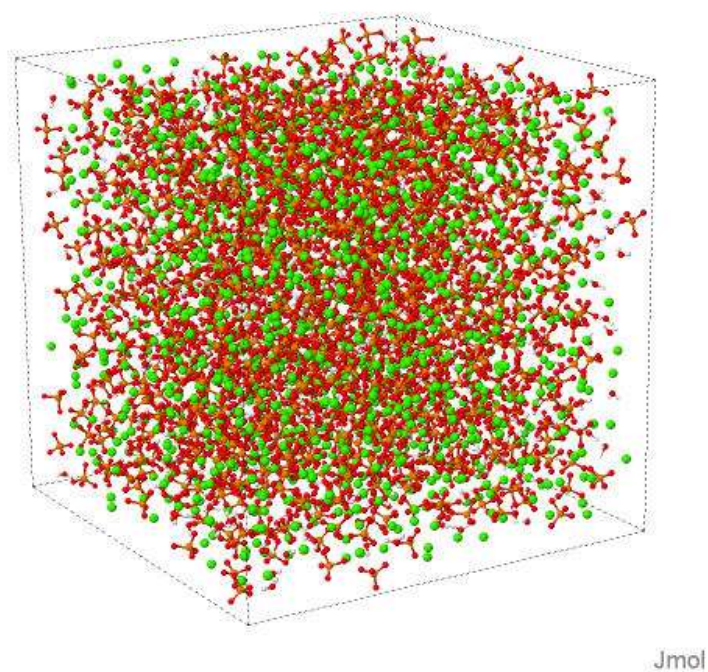


Figure 4.58 - Atomistic Structure of D-ACP, calcium (green), oxygen (red), phosphorous (orange/pink) and deuterium (white). Below is the short range structure zoomed in.

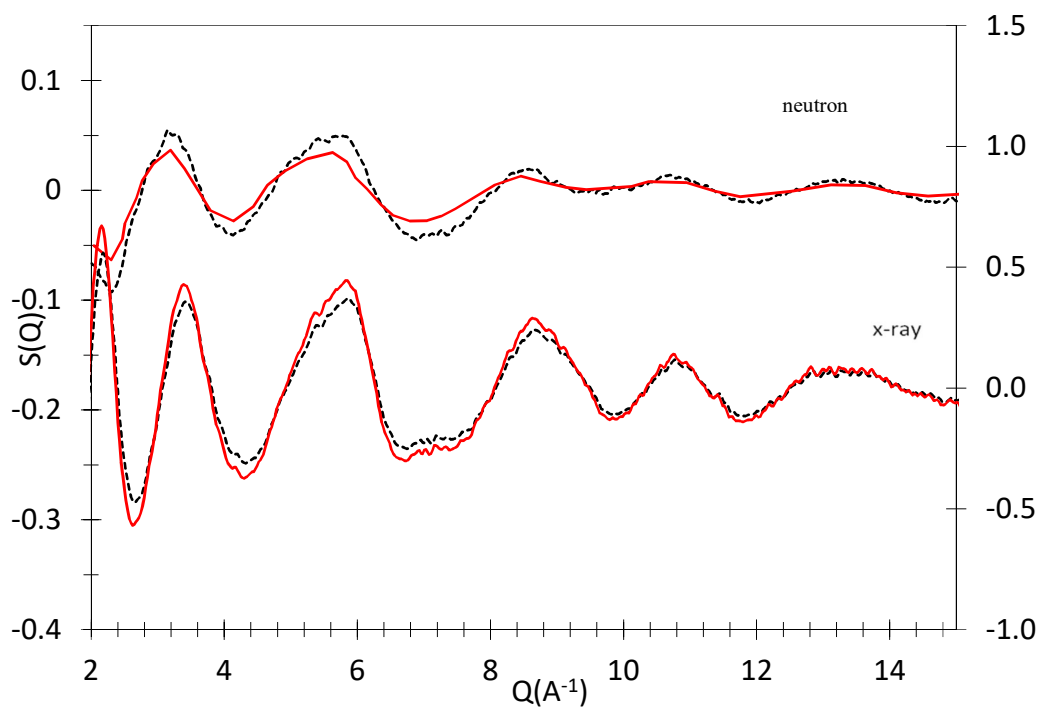


Figure 4.59 - Fitted $S(Q)$ profile from neutron and x-ray diffraction data for ACP450, showing observed (black) and calculated (red) profiles.

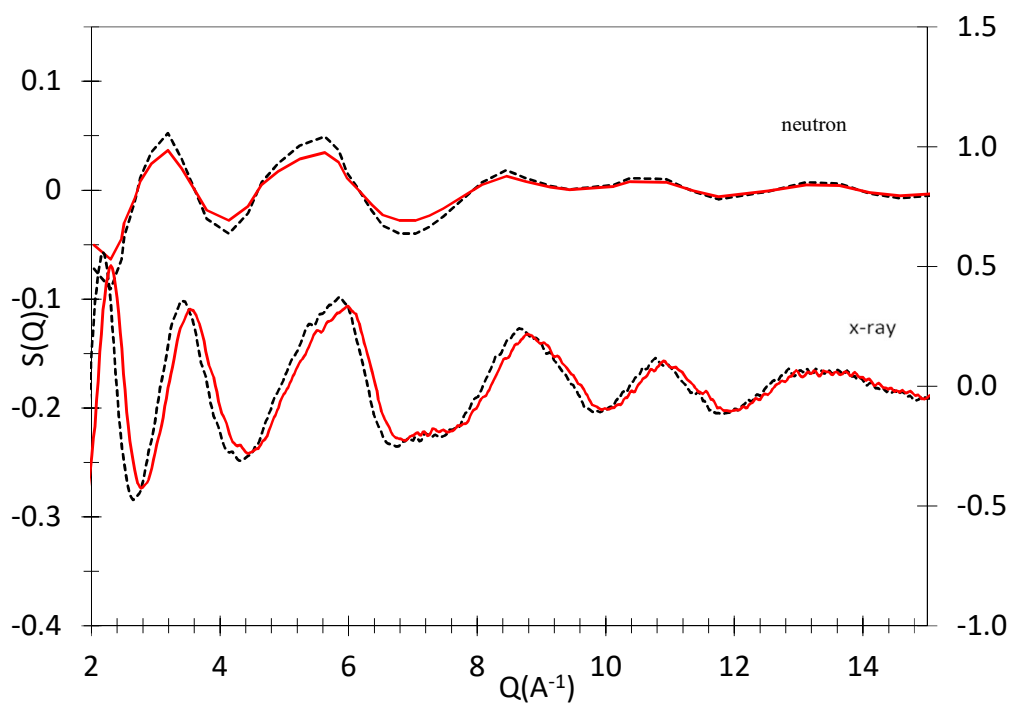


Figure 4.60 - Fitted $S(Q)$ profile from neutron diffraction and x-ray data for D-ACP, showing observed (black) and calculated (red) profiles.

Table 4.8 - Interatomic correlations involving PO₄⁻ ions and H₂O molecular units. (* denotes correlations involving hydrogen bonding)

distance (Å) (approximate)	atoms types i-j	Molecular ion units	Coordination Number
0.92 and (1.3)*	H-O	intra and inter* H ₂ O	1.0 (1.0)
1.6	P-O	intra PO ₄	1.6
1.57 and (1.9)*	H-H	intra and inter* H ₂ O	1.0 (0.5)
2.21	O-O	intra PO ₄	2.2
(2.9)	P-H	inter PO ₄ and H ₂ O	(0.7)
(2.8)	O-O	inter PO ₄ (and H ₂ O)	N/A (large number of O at distances greater than 2.5 Å)
(3.8)	P-O	inter PO ₄ (and H ₂ O)	N/A (large number of O at distances greater than 2.5 Å)
(4.1)	P-P	inter PO ₄	5

Table 4.8 shows the pair correlations involving phosphorus and calcium. Most prominent are the Ca-O distances due to Ca bonding to the oxygen atoms which are present in PO₄ and H₂O molecules, where the peak distance is 2.6 Å. The average coordination number of Ca is found to be 6.7 which are composed of 6.2 oxygen atoms from PO₄ molecules and 0.5 oxygen atoms from H₂O molecules.

These value correspond to previous work conducted on ACP by Kate Weatherall. When compared with the crystalline data[41-47] for calcium phosphate, the closest crystalline structure to that of amorphous calcium phosphate appears to hydroxyapatite[45]. The short-range order of ACP is very similar to that of hydroxyapatite. With previous systems presented in this thesis, ACP does not appear to correspond to short-range order in the amorphous carbonates, this is due to the tetragonal nature of the phosphate molecular ion compared to the trigonal carbonate molecular ion.

4.4.2 Amorphous Iron Phosphate (AFP)

This area of study extends a previous project conducted by B. Al-Hasni^[111] in which heat treated samples of amorphous iron phosphate (AFP) were studied using x-ray and neutron diffraction. To build on the previous work, in this project, the previous experimental data was used in a new computational method. As such, no experimental work was conducted in this area of the project, it was purely computational.

4.4.2.1 Building the EPSR model

The following information is all contained in the previous work by B. Al-Hasni which will be used to build the composition of the model and give it a density

Table 4.9 - Previous Data for AFP samples to build EPSR models

Model	Fe ₂ O ₃ (Fe ³⁺)	P ₂ O ₅	Density (g/cm ³)
30Fe ₂ O ₃	30	70	2.96
40Fe ₂ O ₃	40	60	3.04

Diffraction data were obtained by B. Al-Hasni and this will be used in the modelling process. Figure 4.61 below shows the experimental data and previous molecular dynamics fits to the data.

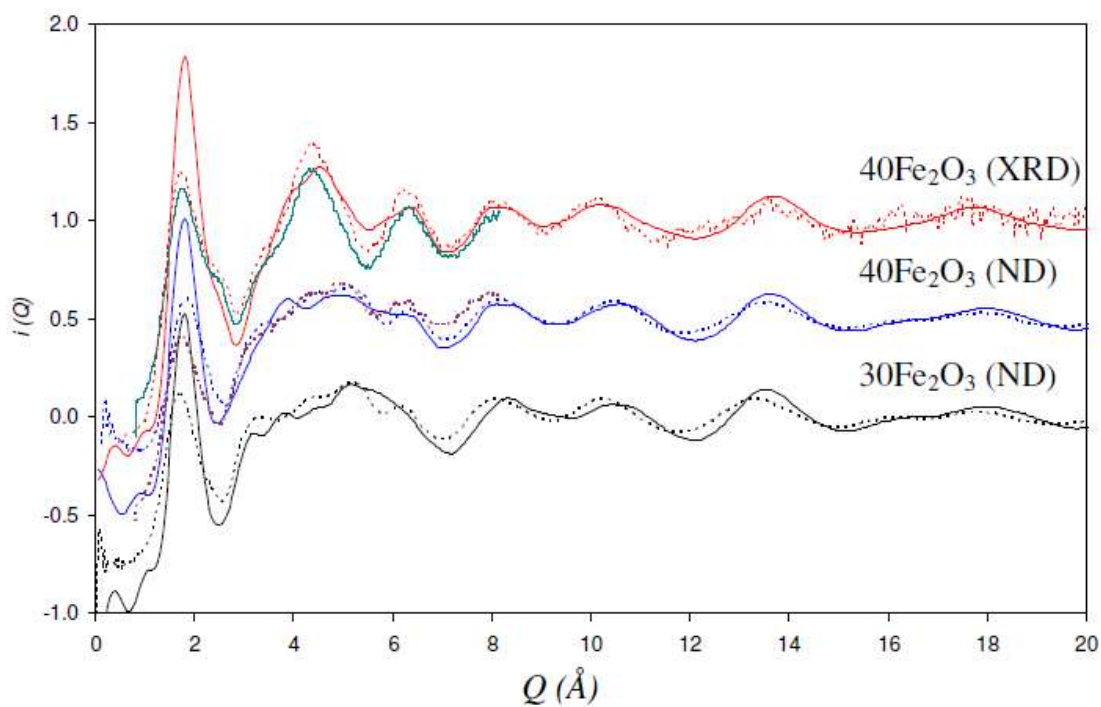


Figure 4.61 - Experimental neutron and x-ray data (dashed lines) and computational (solid lines) of Fe₂O₃ models from previous study by B Al-Hasni^[111]

4.4.2.2 Empirical Potential Structure Refinement (EPSR) Modelling

Structurally realistic molecular units were initially constructed using GHEMICAL4.0 software. For the 30Fe₂O₃ model, a cubic box with length L=37.30 Å containing 300 Fe₂O₃ and 700 P₂O₅ units was assembled using the EPSR shell. This model had a corresponding density for 2.96 g/cm³. In the case of 40Fe₂O₃, a cubic box with length L=37.43 Å containing 400 Fe₂O₃ and 600 P₂O₅ units was assembled using the EPSR shell with a density of 3.04 g/cm³

Following the procedure detailed in section 3.2 yielded the following atomistic structures for $30\text{Fe}_2\text{O}_3$ and $40\text{Fe}_2\text{O}_3$:

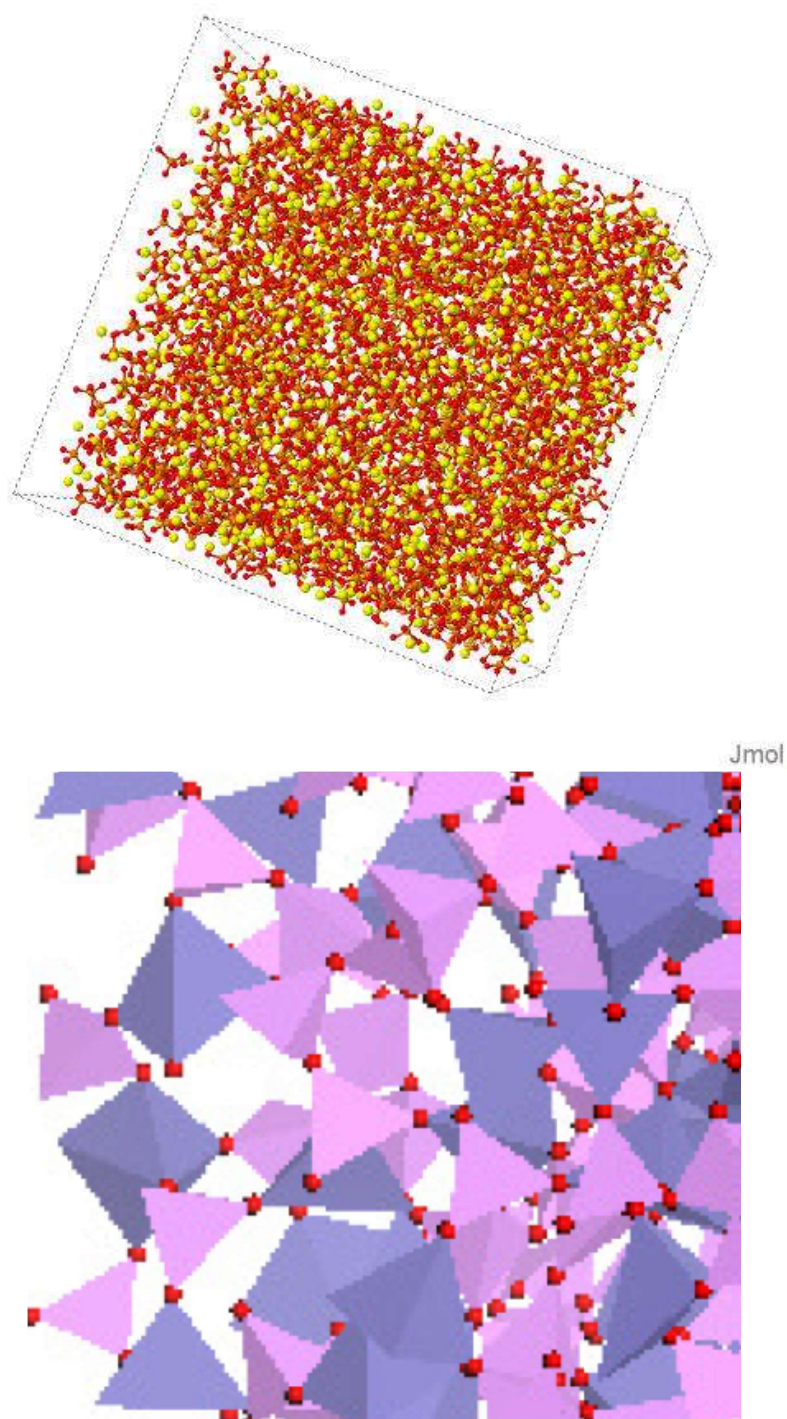


Figure 4.62 - Atomistic Structure of $30\text{Fe}_2\text{O}_3$, iron (yellow), oxygen (red), phosphorous (orange). Below is the close-up of short range structure with oxygen (red), phosphorous tetrahedra (pink), and iron polyhedra (grey).

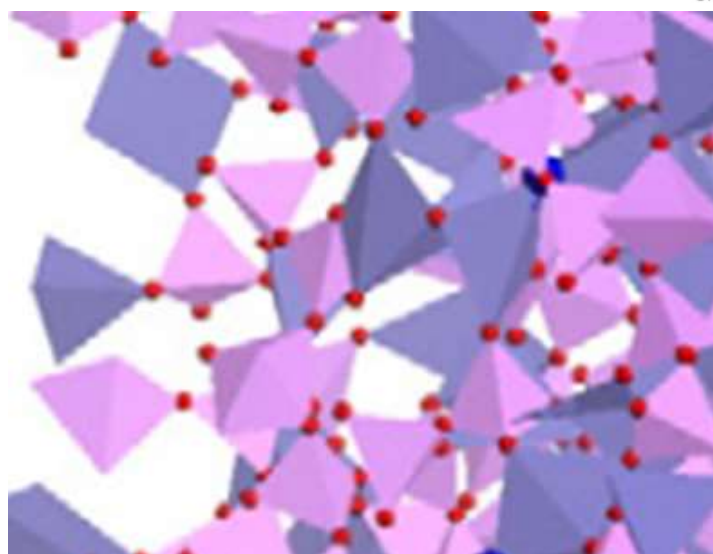
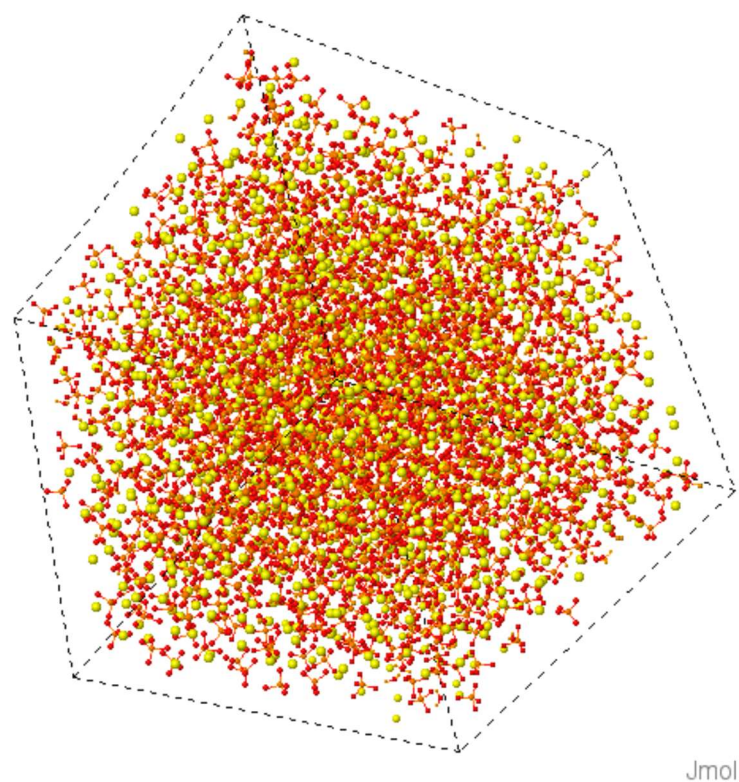


Figure 4.63 - Atomistic Structure of 40Fe₂O₃, iron (yellow), oxygen (red) and phosphorous (orange) . Below is the close-up of short range structure with oxygen (red), phosphorous tetrahedra (pink), and iron polyhedra (grey).

The atomistic models presented above show coordination of iron to be 3.9 oxygens, this agrees with the previous study by B. Al Hasani who stated iron to have a coordination of 4.4.

4.5 Amorphous Sulfates

4.5.1 Amorphous Calcium Sulfate (ACS)

4.5.1.1 Synthesis

In accordance with the pathway detailed in the first paper by Wang et al^[66,73] multiple stock solutions of the reagents of differing concentrations were prepared. Table 4.10 shows the reagents used, mass and volume of stock solution.

Table 4.10 – Stock solution preparation for ACS synthesis

Concentration of Stock Solution (mM)	Reagent	Mass (g)	Volume of Stock Solution (mL)
15	Calcium Chloride hexahydrate (CaCl ₂ .6H ₂ O)	3.286	1000
15	Sodium Sulfate (Na ₂ SO ₄)	2.131	1000
50	Calcium Chloride hexahydrate (CaCl ₂ .6H ₂ O)	10.954	1000
50	Sodium Sulfate (Na ₂ SO ₄)	7.102	1000
100	Calcium Chloride hexahydrate (CaCl ₂ .6H ₂ O)	21.908	1000
100	Sodium Sulfate (Na ₂ SO ₄)	14.204	1000

In a departure from the method stated by Wang et al^[66], initially, instead of using a crystallisation dish, solutions of Ca and SO₄ were mixed in a Millipore™ glass filtration kit before being rapidly filtered through a Cyclopore® 0.2 µm pore size, track-etched polycarbonate membrane filter (47 mm diameter) before being washed with isopropanol to form a clear/white precipitate. The membrane filter was removed and the precipitate dried using flowing air.

Additives, in line with the second paper by Wang et al^[73], were prepared in stock solutions of magnesium (Mg) and phosphate (PO₄). The omission of poly(acrylic acid) and poly(styrene-4-sulfonate) was because if they were incorporated into a sample of ACS, during neutron diffraction high proton content of both of these organic molecules would result in a large degree of inelastic scattering and would reduce the quality of data obtained. Stock solutions of the additives were prepared as in Table 4.11

Table 4.11 – Stock solutions preparation of additives for ACS synthesis

Concentration of Stock Solution (mM)	Reagent	Mass (g)	Volume of Stock Solution (mL)
100	Magnesium Chloride (MgCl ₂)	9.521	1000
100	Sodium Phosphate (Na ₃ PO ₄)	16.394	1000

4.5.1.2 Lab-based characterisation

4.5.1.2.1 Lab Powder X-ray Diffraction (XRD)

Upon analysing samples of ACS, no amorphous patterns were recorded (see figure 4.64) and after multiple attempts and no successful outcomes work was put on hiatus while an alternative method of synthesis or an explanation for the lack of success was found.

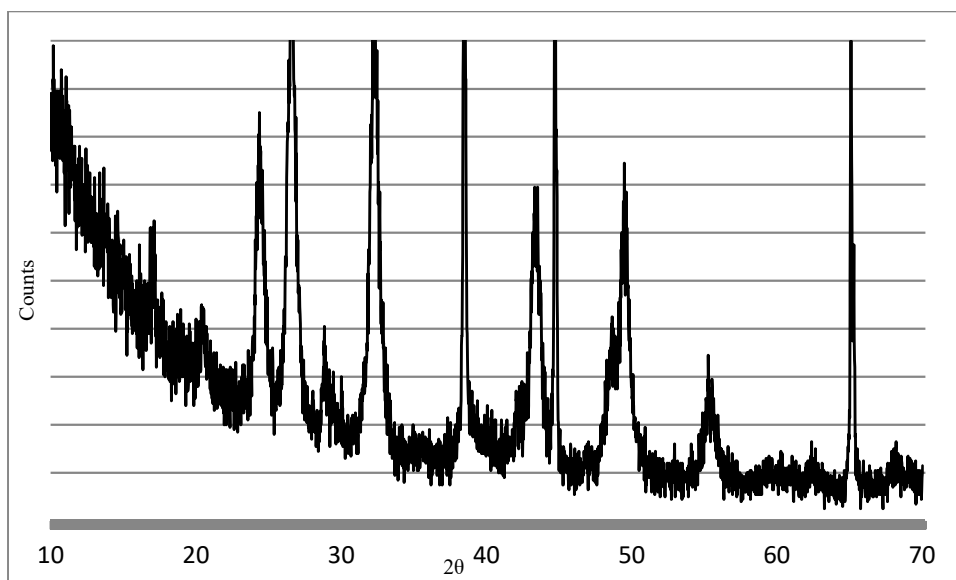


Figure 4.64 - XRD pattern of ACS sample, containing no amorphous elements

After a conversation with a collaborator, it was revealed that work and reaction pathway to produce ACS detailed in the above paper^[66] was misleading. The 'amorphous' element described in the work was most likely a resolution artefact of the instrument being used. As shown in his work Van Driessche et al^[112] showed that calcium sulfate forms through a crystalline intermediary and not an amorphous material.

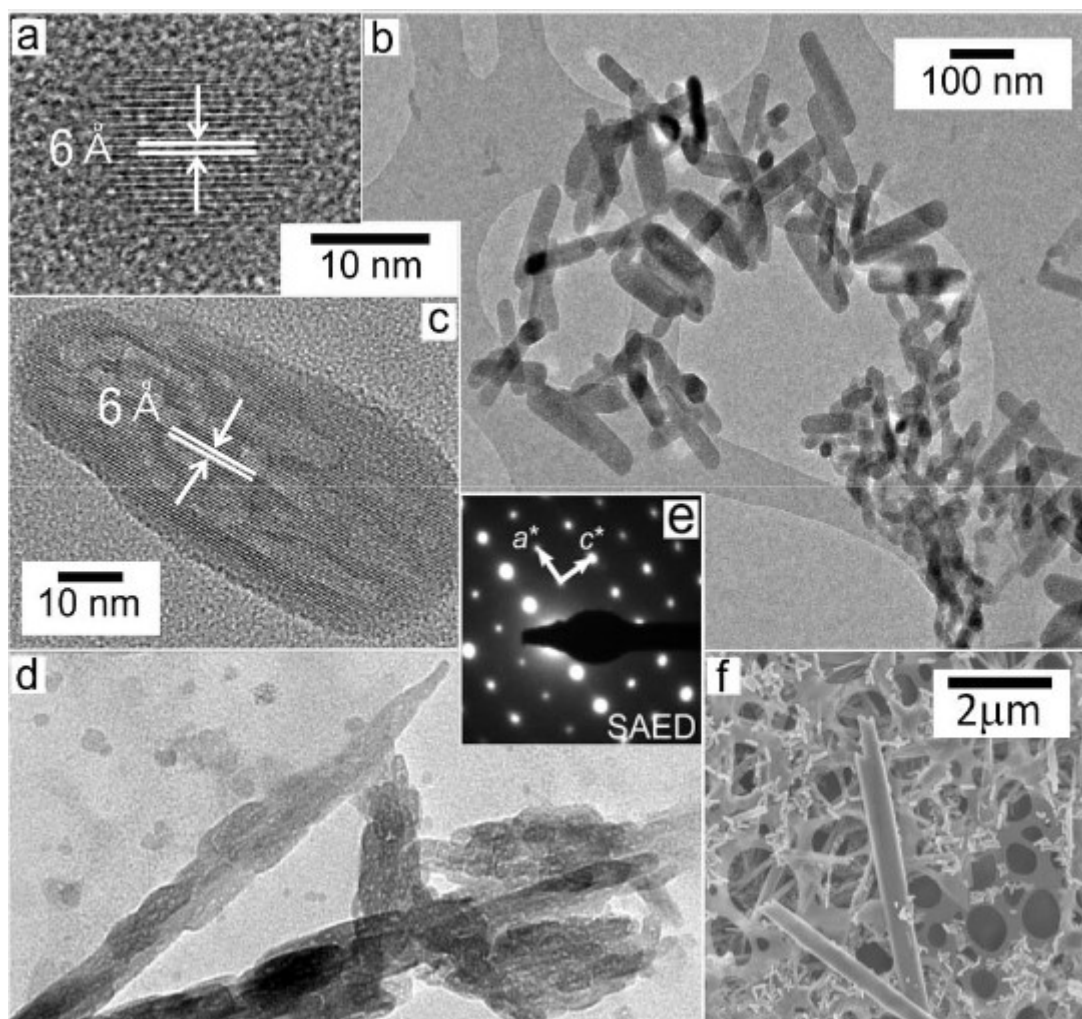


Figure 4.65 - HR-TEM and SEM microphotographs of the crystallisation of gypsum: (a) typical nanocrystalline particle obtained in a 150 mM CaSO_4 , (b) bassanite nanorods obtained from the same solution, (c) larger bassanite nanorod, (d) large aggregates formed by self-assemble of bassanite nanorods, (e) SAED of oriented bassanite aggregate, (f) final gypsum crystals and bassanite nanocrystals.^[112]

After learning this, work on producing ACS was abandoned and other sub-projects were prioritised.

4.5.2 Amorphous Iron Sulfate (AFS)

4.5.2.1 Synthesis

A commercial amorphous sample of iron sulfate pentahydrate ($\text{Fe}_2(\text{SO}_4)_3 \cdot 5\text{H}_2\text{O}$) from Acros Chemicals, referred to as AFS. Due to the five water groups present in AFS, this results in a large amount of protons in the material which are detrimental to neutron diffraction. In an effort to minimise the inelastic scattering from the proton content, water was removed by heating the sample to various temperatures for one hour (temperatures were determined by TGA analysis of the raw material, discussed in section 4.5.2.2.2). These temperatures were in 50 °C increments from 100-300 °C.

A second set of samples involved intentionally crystallising AFS to remove all the water groups. This crystalline sample was then ball-milled to 'amorphise' the sample.

4.5.2.2 Lab-based characterisation

4.5.2.2.1 Lab Powder X-ray Diffraction (XRD)

The heat-treated and unheated samples of AFS were analysed by XRD immediately after synthesis to determine which were amorphous. These same samples were kept sealed in a 5 mL glass bottle secured with lab film and re-measured at varying intervals (1, 3, 7 and 14 days after synthesis). Initially the plan was to prepare a sample of AFS300 to study but heat treating AFS at 300 °C for 1 hour caused the product to burn and thus was not useful, therefore, Figure 4.66 shows the results over time for sample AFS250.

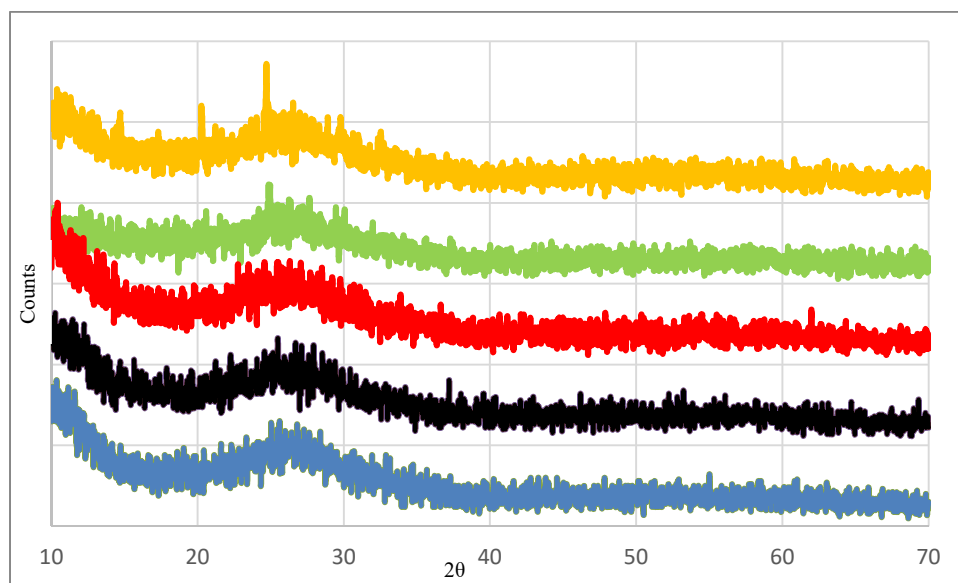


Fig 4.66 – XRD patterns for AFS250 over time from 0 days (blue), 1 day (black), 3 days (red), 7 days (green) and 14 days (orange) after synthesis.

The heat-treated sample, denoted AFS250, was confirmed amorphous by lab-based x-ray diffraction and the longevity of sample was found to be greater than two weeks. This sample was deemed suitable for central facility experiments.

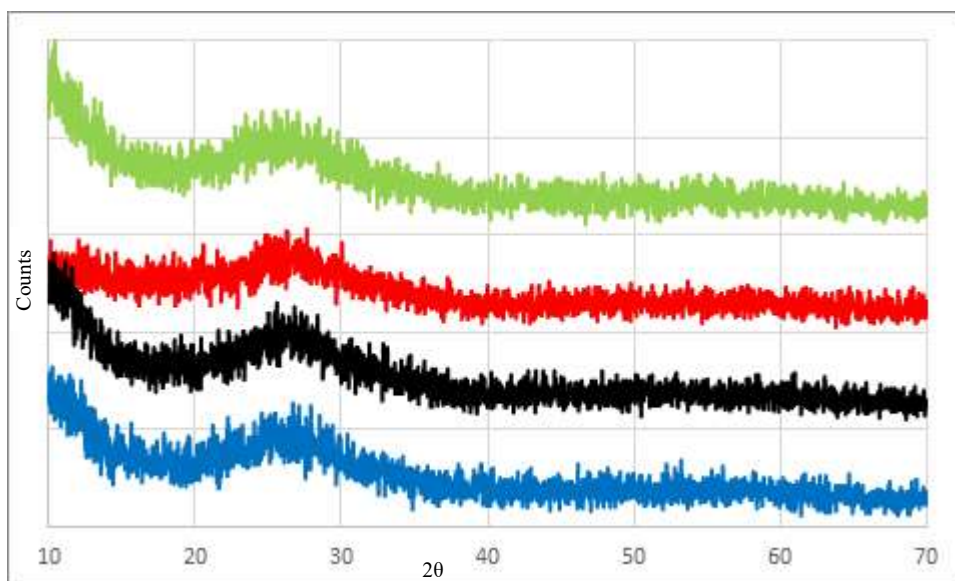


Figure 4.67 - XRD patterns for AFSBM over time from 1 day (black), 3 days (red), 7 days (green) and 14 days (orange) after synthesis.

As with AFS250, AFSBM was determined to have an amorphous longevity of greater than 2 weeks so would be studied and central facilities.

4.5.2.2.2 *Thermo-Gravimetric Analysis (TGA)*

A sample of freshly prepared AMCunh was analysed using TGA-DTA and the results are shown in figure 4.42 and 4.43.

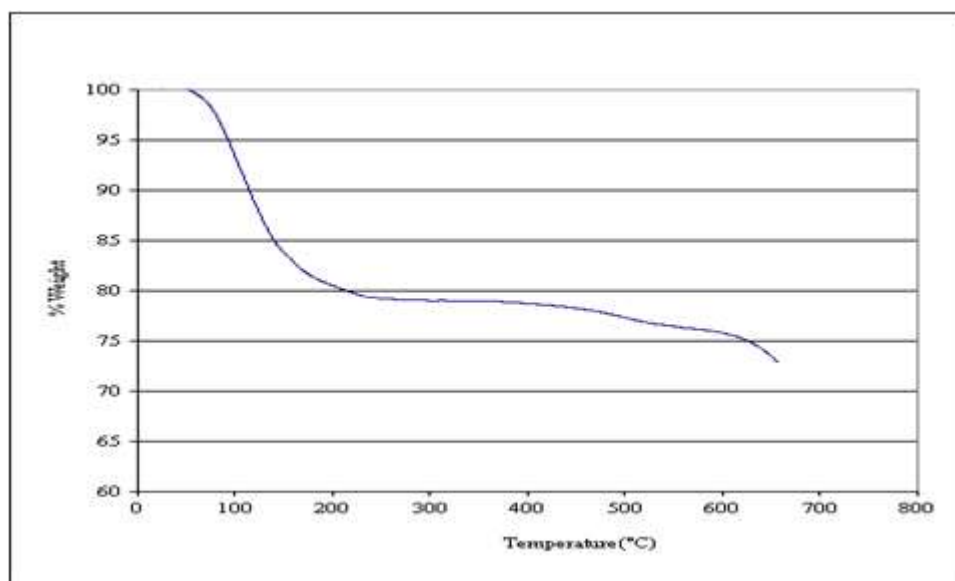


Figure 4.68 – TGA of AFS, showing weight loss of 20% up to approximately 200°C and 28% to 500°C at which point AFS crystallises (see figure 4.43).

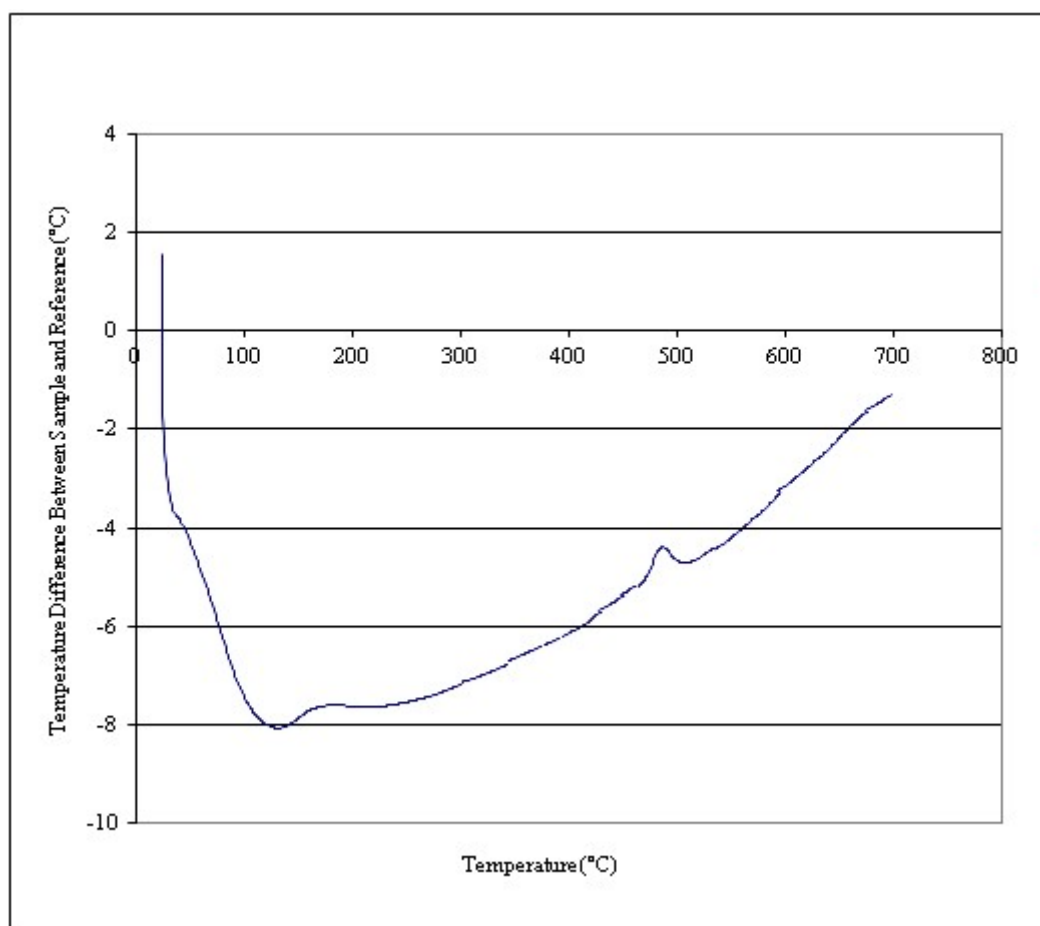


Figure 4.69 – DTA of AFS showing a crystallisation peak at approximately 500°C

The TGA-DTA of AFS showed weight losses of 20% and 28% up to temperatures of 200 °C and 500 °C respectively, the latter being when AFS crystallises. These weight losses are consistent with a water content of $n=5$ before and $n= 0.15$ after heat treatment at 200 °C. The value of $n = 0.15$ will be used for EPSR modelling of AFS250. AFSBM will have $n = 0$ as it will have been intentionally crystallised - ie. driven all the interstitial water off.

4.5.2.2.3 Helium Micropycnometry

The density of AFS-250 was measured to be 2.51 g/cm³ using a He pycnometer and AFSBM was shown to have a density of 2.61 g/cm³

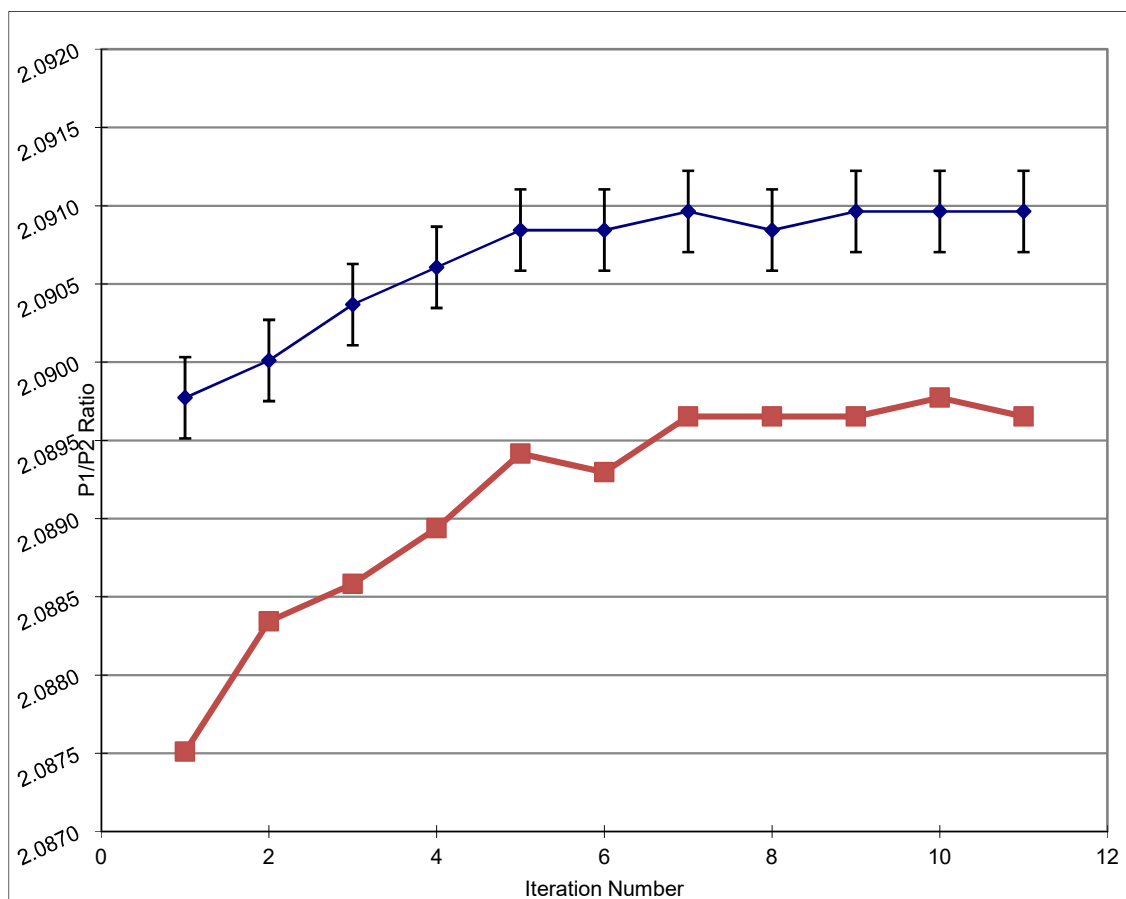


Figure 4.70 - He-pycnometry of AFSBM (blue) and AFS250 (red) samples showing the P1/P2 ratio, the procedure was repeated until the recorded density was within acceptable limits (1 s.d. - black error bar)

The calculated densities were be used in the EPSR modelling procedure.

4.5.2.3 Central Facility Experiments

Whilst conducting central facility experiments at both Elettra and ISIS, both samples of AFS (AFS250 and AFSBM) crystallised so sufficient diffraction data was not able to be obtained.

4.5.2.4 Empirical Potential Structure Refinement (EPSR) Modelling

Unfortunately, due to the lack of diffraction data, an EPSR model was unable to be produced as the absence of experimental data would make the EPSR model ineffective. Suggestions for future work on this material are discussed in section 5.6.

5. Conclusions

5.1 *Amorphous Calcium Carbonate*

Whilst ACC is a particularly difficult and temperamental system to work with, a stable sample was produced. The successful synthesis of stable ACC lead to the production of a deuterated ACC, something not reported before.

Synthesis of ACC and the deuterated counterpart, D-ACC, enabled the first neutron diffraction experiment to be conducted on an ACC system(s), and coupling this with experimental x-ray diffraction data obtained in this project and from previous work by Michel et al^[17] an understanding of this interesting system is beginning to unfold.

The experimental neutron and x-ray data from ACC and D-ACC were incorporated into the EPSR modelling procedure which yielded fair agreement. Some disagreement at low Q was observed, which is likely due to high constraints of molecular ions such as CO₃²⁻. Analysis of the EPSR model lead to the average coordination number of calcium to be 7.2 which are comprise of 6.8 oxygen atoms from CO₃ molecular ions and 0.6 oxygen atoms from H₂O. This is in good agreement with the EXAFS results of Michel et al^[17] for ACC, which were Ca-O coordination number of 6.5±1.6 and peak distance of 2.42±0.02 Å.

Of particular note is the contrast between the model presented in this thesis and the published RMC model by Goodwin et al^[27]. In the Goodwin model, it was presented that ACC contained large channels of calcium rich and calcium poor regions (where calcium was 4Å or greater away from another calcium), but in the present work, these channels are not to be found. This is the same with the crystalline monohydrocalcite, to which ACC has some similarity to in composition and short-range order^[19]

5.2 *Magnesium Stabilised Amorphous Calcium Carbonate*

The addition of magnesium to ACC was of particular benefit during the experimental section of this work. With the production of a stable sample of ACC with only a minor additive (not large quantities of additive nor large organic species) gave a good benchmark whilst new strategies were developed to synthesise a stable ‘pure’ ACC as mentioned above. An additional benefit was the ability to perform heat-treatment (to reduce proton content for neutron experiments) on this species of ACC was possible, due to the high levels of instability of ‘pure’ ACC this was not possible.

Neutron and x-ray diffraction experiments were conducted of Mg-ACC, the first of their kind to be reported.

Mg-ACC diffraction data were fed into the computational model within EPSR of the heat-treated sample. The average coordination number of calcium in the EPSR model was 7.4 which are composed of 6.8 oxygen atoms from CO₃ and 0.6 oxygen atoms from H₂O. These features of the model are in good agreement with the EXAFS results of Michel et al^[17] for ‘pure’ ACC and results of D-ACC from the present work.

Like with the D-ACC model, the EPSR model of calcium distribution in Mg-ACC showed no channels of calcium rich and calcium poor regions, with calcium being 4Å away from a different calcium. There is agreement with both this model and that of ACC showing monohydrocalcite-like short-range order^[19,28]

5.3 *Amorphous Magnesium Carbonate*

Whilst this system is not technically a biomineral, it is still interesting to observe the similarities and differences within its structure compared to both ACC and Mg-ACC and the author felt this was the next logical step after studying the two previous systems.

Using the established method for fabricating ACC and Mg-ACC, samples of AMC were produced. A deuterated sample was also synthesised at ISIS for neutron diffraction experiments. As the samples of AMC could be both heat-treated and deuterated, this was an interesting insight into the two potential methods of reducing proton content – would there be any major difference in the observed atomistic model?

The outcome of the experimental section was collection of neutron data for both D-AMC and AMC200 and x-ray data for AMC200. The lack of x-ray data for ‘pure’ AMC was due to the method of sealing the XRD capillary with wax and then melting the wax. The application of heat to the capillary caused the samples of AMC to crystallise and whilst additional samples were produced on site, they too crystallised.

Despite lack of x-ray data for AMC, EPSR models were produced for each system (AMC only using neutron data) with good agreement to the experimental data and additionally, good agreement to both systems. It stands that both the method of deuteration and heat-treatment produce samples of amorphous materials of similar atomistic structure. The average coordination number of magnesium in the EPSR model was 7.0 which are composed of 6.4 oxygen atoms from CO_3 and 0.6 oxygen atoms from H_2O .

5.4 *Amorphous Phosphates*

This section of the project was designed to validate both the experimental synthesis and the computational method of the amorphous materials using a well-studied biomineral. Also, as with AMC, how does the deuterated version of ACP compare to the heat-treated sample. Further confirmation of the EPSR model could be achieved using the data-only investigation into AFP, as this had already been studied experimentally it appeared to be a good test of how well the EPSR modelling could fit to neutron and x-ray data.

Studying ACP showed a fair agreement with the previous study by K. Wetherall of ACP450. The results show a similarity between ACP presented here and the crystalline form hydroxyapatite.[45]

The results of AFP should fair agreement with the results presented by B. Al Hasani[102] which strengthens the argument for EPSR being a key investigative tool. Al Hasani presented results stating that iron is coordinated to 4.4 oxygen atoms which agrees with the 3.9 oxygen atoms presented in this work.

5.5 *Amorphous Sulfates*

The aim of this section was to further illustrate the effectiveness of both the synthesis/deuteration method and computational modelling of amorphous biominerals but due to a misleading journal article published by Meldrum et al^[66] the synthesis of ACS proved fruitless.

Whilst the fabrication of AFS was more straightforward, using heat-treatment only of a commercially available iron sulfate, it became evident when conducting neutron diffraction experiments that the samples of AFS were nano-crystalline. This was interesting as the lab-based experiments had shown no signs of crystallinity, but it was proposed that crystals were so small in size that they were below the resolution of detection for lab-based XRD and thus any signals were lost in the noise.

5.6 *Future Work*

Development of future work from this project will hopefully build on the knowledge gained and presented here.

For experimental work, the author believes that the extension of the synthesis method and the method of deuteration would greatly assist in the study of not only other biominerals with high proton content but other materials containing much hydrogen. Of interest to the author is a study of the magnesium

content of ACC samples, structural studies on samples of ACC with differing magnesium content to look at the role of magnesium in ACC stability. These materials could be studied using the heat-treatment or deuteration method or both.

Returning to central facilities like Elettra or ISIS to conduct additional studies on the materials produced in this work that crystallised or encountered problems whilst on site. These include x-ray data for AMC, using a less heat-based method of sealing the XRD capillary. If possible a study of the nano-crystalline nature of AFS could be of interest looking at how these crystals form and how they evolve over time, do they stay nano-crystals or do they accumulate and grow to larger crystals?

6. Bibliography

- [1] Image obtained from: <http://www.majordifferences.com/2013/02/difference-between-crystalline-and.html#.WNo0Kme1vIU> - Accessed 23/06/14
- [2] J.L. Kirschvink & J.W. Hagadorn, "10 A Grand Unified theory of Biomineralization.". In B  uerlein, E. The Biomineralisation of Nano- and Micro-Structures, Wiley-VCH, 2000, 139–150
- [3] K. Towe, H. Lowenstam, Journal of Ultrastructure Research. 17, 1, 1967 1–13
- [4] D. Belton, O. Deschaume & C. Perry, FEBS J., 279 (10), 2012, 1710–1720.
- [5] A. Becker, I. S  tje, C. Paulmann, F. Beckmann, T. Donath, R. Boese, O. Prymak, H. Tiemann & M. Epple, Dalton Trans., 2005, 1545-1550
- [6] L. Addadi, S. Raz, S. Weiner, Adv. Mater. 15, 2003, 959.
- [7] C. Combes, C. Rey, Acta Biomater. 6, 2010, 3362.
- [8] D. Graf, American Mineralogist , 46, 1961, 1283-1316
- [9] O. DeFoe & A. Compton, Phys. Rev. 25, 1925, 618
- [10] J. de Villiers, American Mineralogist , 56, 1971, 758-767
- [11] G. Falini, S. Fermani, S. Vanzo, M. Miletic, & G. Zaffino, Eur. J. Inorg. Chem., 2005, 162–167
- [12] S. Kamhi, Acta Crystallographica , 16, 1963, 770-772
- [13] I. Swainson, American Mineralogist , 93, 2008, 1014-1018
- [14] M. Neumann & M. Epple, Eur. J. Inorg. Chem., 2007, 1953–1957.
- [15] K. Hesse, H. Koppers, E. Suess, 163, 1983, 227-231
- [16] S. Rysgaard, F. Wang, R. Galley, R. Grimm, D. Notz, M. Lemes, N.-X. Geilfus, A. Chaulk, A. Hare, O. Crabeck, B. Else, K. Campbell, L. S  rensen, J. Sievers & T. Papakyriakou, The Cryosphere, 8, 2014, 1469–1478
- [17] F.M. Michel, J. MacDonald, J. Feng, B.L. Phillips, L. Ehm, C. Tarabrella, J.B. Parise, R.J. Reeder, Chem. Mater. 20, 2008, 4720.
- [18] A. V. Radha, T.Z. Forbes, C.E. Killian, P.U.P.A. Gilbert, A. Navrotsky Proc. Nat. Acad. Sci. 107, 2010, 16438.
- [19] K. Kojima, A. Kawanobe, T. Yasue, Y. Arai, J. Cer. Soc. Jpn. 101, 1993, 1145.
- [20] N. Koga, Y. Nakagoe, H. Tanaka, Thermochim. Acta 318, 1998, 239.
- [21] P. Raiteri, J.D. Gale, J. Am. Chem. Soc. 132, 2010, 17623.
- [22] J.D. Rodriguez-Blanco, S. Shaw, L.G. Benning, Nanoscale 3, 2011, 265.

- [23] J.D. Rodriguez-Blanco, P. Bots, T. Roncal-Herrero, S. Shaw, L.G. Benning, *J. Alloys Comp.* 536, 2012, S477.
- [24] E. Loste, R.J. Park, J. Warren, F.C. Meldrum, *Adv. Funct. Mater.* 14, 2004, 1211.
- [25] J. Johnson, H.E. Merwin, E.D. Williamson, *Am. J. Sci.*, 111, 1916 33.
- [26] F.A. Andersen, L. Brecevic, *Acta Chem. Scand.* 45, 1991, 1018.
- [27] A.L. Goodwin, F.M. Michel, B.L. Phillips, D.A. Keen, M.T. Dove, R.J. Reeder, *Chem. Mater.* 22, 2010, 3197.
- [28] J.W. Singer, A.Ö. Yazaydin, R.J. Kirkpatrick, G.M. Bowers, *Chem. Mater.* 24, 2012, 1828.
- [29] J. Jiang, M.R. Gau, Y.H. Qiu, S.H. Yu, *Nanoscale* 2, 2010, 2358.
- [30] J. Ihli, Y.Y. Kim, E.H. Noel, F.C. Meldrum, *Adv. Funct. Mater.* 23, 2012, 1575.
- [31] A.V. Radha, A. Fernandez-Martinez, Y. Huc, Y-S. Jun, G.A. Waychunas, A. Navrotsky, *Geoch. Cosmoch. Acta* 90, 2012, 83.
- [32] Y. Politi, D. R. Batchelor, P. Zaslansky, B. F. Chmelka, J. C. Weaver, I. Sagi, S. Weiner & L. Addadi, *Chem. Mater.*, 22, 2010, 161–166
- [33] E. Foran, S. Weiner & M. Fine, *Scientific Reports* 3, Article number: 1700, 2013
- [34] L. Valenzano, Y. Noel, R. Orlando, C. M. Zicovich-Wilson, M. Ferrero & R. Dovesi *Theoretical Chemistry Accounts*, 117, 2007, 991-1000
- [35] R. A. Robie, P. M. Bethke, M. S. Toulmin, & J. L. Edwards, *Geological Society of America Memoirs*, 97, 1966, 27-74
- [36] G.W. Stephan, C.H. MacGillavry, *Acta Crystallographica B*, 28, 1972, 1031-1033
- [37] G. Giester, C. Lengauer, & B. Rieck, *Mineralogy and Petrology*, 70, 2000, 153
- [38] B.N. Liu, X.T. Zhou, X.S. Cui, J.G. Tang, *Science in China B*, 33, 1990, 1350-1356
- [39] R. J. Hill, J.H. Canterford & F.J. Moyle, *Mineralogical Magazine*, 46, 1982, 453-7
- [40] J. Forsgren, S. Frykstrand, K. Grandfield, A. Mihranyan, M. Strømme, *PLoS ONE* 8, 2013, e68486
- [41] G. MacLennan & C. A. Beevers, *Acta Cryst.*, 9, 1956, 187-190
- [42] G. MacLennan & C. A. Beevers, *Acta Cryst.*, 8, 1955, 579-583
- [43] J.-S. Bow, S.-C. Liou, S.-Y. Chen, *Biomaterials*, 25, 2004, 16, 3155–3161
- [44] A. Cuneyt Tas, F. Korkusuz, M. Timucin, N. Akkas, *Journal of Materials Science: Materials in Medicine*, 8, 1997, 2, 91–96

- [45] H. Monma, S. Ueno & T. Kanazawa, *J. Chem. Technol. Biotechnol.*, 31, 1981, 15–24.
- [46] B. He, S. Huang, J. Jing, Y. Hao, *Archives of Oral Biology*, 55, 2010, 2, 134–141
- [47] J.M. Hughes, M. Cameron, K.D. Crowley, *American Mineralogist*, 74, 1989, 870-876
- [48] W. L. Jaffe and D. F. Scott, *Journal of Bone and Joint Surgery A*, 78, 1996, 12, 1918–1934
- [49] A. M. Moursi, A. V. Winnard, P. L. Winnard, J. J. Lannutti, and R. R. Seghi, *Biomaterials*, 23, 2002, 1, 133–144
- [50] K M Wetherall, D M Pickup, R J Newport & G Mountjoy, *J. Phys.: Condens. Matter*, 21, 2009, 035109
- [51] A. Masingu, G. Piccaluga, G. Pinna, *J. NonCryst. Solids*, 122, 1990, 52
- [52] G.N. Greaves, S.J. Gurman, L.F. Gladden, C.A. Spence, P. Cox, B.C. Sales, L.A. Boatner, R.N. Jenkins, *Philos. Mag. B*, 58, 1988, 217.
- [53] B.C. Sales, L.A. Boatner, *J. NonCryst. Solids*, 45, 1984, 266.
- [54] B.C. Sales, L.A. Boatner, *Science*, 79, 1986, 83.
- [55] M. Karabulut, G.K. Marasinghe, C.S. Ray, D.E. Day, G.D. Waddill, C.H. Booth, P.G. Allen, J.J. Bucher, D.L. Caulder, D.K. Shuh, *J. NonCryst. Solids*, 306, 2002, 182
- [56] Y. Song, P.Y. Zavalij, M. Suzuki, M.S. Whittingham, *Inorganic Chemistry.*, 41 2002, 22, 5778–5786
- [57] T. Roncal-Herrero, J.D. Rodriguez-Blanco, L.G. Benning, E.H. Oelkers, *Crystal Growth & Design*, 9, 2009, 5197-5205.
- [58] S.-Y. Chung, J.T. Bloking & Y.-M. Chiang, *Nature Materials* 1, 2002, 123-128
- [59] A. Ritchie, W. Howard, *Journal of Power Sources*, 162, 2006, 2, 809–812
- [60] J. Hassoun, F. Bonaccorso, M. Agostini, M. Angelucci, M. Grazia Betti, R. Cingolani, M. Gemmi, C. Mariani, S. Panero, V. Pellegrini, & B. Scrosati, *Nano Letters*, 14, 2014, 8, 4901-4906
- [61] J.-M. Tarascon & M. Armand, *Nature*, 414, 2001, 359-367
- [62] H. Xie & Z. Zhou, *Electrochimica Acta*, 51, 2006, 10, 2063–2067
- [63] B. Al-Hasani, G. Mountjoy, *J. Non-Cryst. Solids*, 357, 2011, 2775–2779
- [64] U. Hoppe, M. Karabulut, E. Metwalli, R.K. Brow, P. Jovari, *J. Phys. Condens. Matter*, 15, 2003, 6143–6153.
- [65] A.C. Wright, R.N. Sinclair, J.L. Shaw, R. Haworth, G.K. Marasinghe, D.E. Day, *Phys. Chem. Glasses Eur. J. Glass Sci. Technol. B*, 49, 2008, 1–7.
- [66] Y.-W. Wang, Y.-Y. Kim, H.K. Christenson & F.C. Meldrum, *Chem. Commun.*, 48, 2012, 504-506

- [67] G. Orsini, J. Ricci, A. Scarano, G. Pecora, G. Petrone, G. Iezzi, A. Piattelli, J. Biomed Mater Res B Appl Biomater., 68, 2004, 2, 199-208.
- [68] F.C. Hawthorne, R.B. Ferguson, The Canadian Mineralogist, 13, 1975, 289-292
- [69] M.V. Thomas & D.A. Puleo, J. Biomed. Mater. Res., 88, 2009, 597-610.
- [70] P.F. Schofield, K.S. Knight, I.C. Stretton, American Mineralogist, 81, 1996, 847-851
- [71] J.-P. Boisvert, M. Domenech, A. Foissy, J. Persello, J.-C. Mutin, Journal of Crystal Growth, 220, 2000, 4, 579-591
- [72] P. Ballirano, A. Maras, S. Meloni, R. Caminiti, European Journal of Mineralogy, 13, 2001, 985-993
- [73] Y.-W. Wang, & F.C. Meldrum, J. Mater. Chem., 22, 2012, 22055-22062
- [74] J.P. Grotzinger, Science, 341, 2013, 6153, 1475
- [75] J. Majzlan, C. Botez, P.W. Stephens, American Mineralogist, 90, 2005, 411-416
- [76] C. A. Cravotta III, Environmental Geochemistry of Sulfide Oxidation., 1993, 345-364
- [77] J.H. Fang, P.D. Robinson, American Mineralogist, 55, 1970, 1534-1540
- [78] E. Sklute, H.B. Jensen, D. Rogers, R.J. Reeder, American Geophysical Union, Fall Meeting 2014, abstract #P34A-02
- [r1] Kittel, C. (2015). *Introduction to Solid State Physics* (Eighth ed.). John Wiley & Sons, Inc.
- [r2] Lefmann, K. (2007, August 25). *Neutron Scattering: Theory, Instrumentation, and Simulation*. Technical University of Denmark.
- [r3] Barnes, P., Csoka, T., & Jacques, S. (n.d.). *Bragg's Law*. Retrieved March 9, 2016 from Advanced Certificate in Powder Diffraction on the Web: <http://pd.chem.ucl.ac.uk/pdnn/powintro/braggs.htm>
- [r4] Fitter, J., Gutberlet T., & Katsaras, J. (2006). *Neutron Scattering in Biology Techniques and Applications*. Germany: Springer-Verlag Berlin Heidelberg.
- [r5] Krivoglaz, M. A. (1996). *X-Ray and Neutron Diffraction in Nonideal Crystals*. Springer-Verlag Berlin Heidelberg.
- [r6] Sivia, D. S. (2011). *Elementary Scattering Theory*. United States: Oxford University Press Inc., New York.
- [r7] Simmons, C. J., & El-Bayoumi, O. H. (1993). *Experimental techniques of glass science*.
- [r8] B.M. Al-Hasni (2011). Advanced Structural Characterisation of Glasses and Amorphous Oxides, PhD Thesis, University of Kent.
- [r9] Mountjoy, G. (1995). Diffraction and Microscopy Studies of the Structure of Amorphous Solids, PhD Thesis, University of Cambridge.

- [r10] Barnes, P., Jacques, S., & Vickers, M. (n.d.). *Properties of Synchrotron Radiation*. Retrieved March 9, 2016 from Advanced Certificate in Powder Diffraction on the Web: <http://pd.chem.ucl.ac.uk/pdnn/inst2/prop.htm>
- [r11] Stachurski, Z. H. (2011, September 15). On Structure and Properties of Amorphous Materials. *Open Access Materials Science Journal* .
- [r12] West, A. R. (2014). *Solid State Chemistry and its Applications* (Second, student ed.). Chichester: John Wiley & Sons, Ltd.
- [r13] Frenkel, D; Smit, B, 1996, Understanding Molecular simulation, Academic Press, London, pages: 63-71, 84-87.
- [r14] A. K. Soper, PHYSICAL REVIEW B 72, 104204 (2005)
- [79] Y.T. Feng, K.N. Han, D.R.J. Owen, Materials Science and Engineering A, 375-377, 2004, 1, 815-819
- [80] R.L. Eisenberg, Radiology – An Illustrated History. Mosby. St. Louis., 1991.
- [81] A.L. Young, American Pharmaceutical Review, 15, 2012, 1
- [82] A.W. Coats, J.P. Redfern, Analyst., 88, 1963, 1053, 906–924
- [83] © Solid Forms Solutions Ltd - retrieved 06/03/16
- [84] R. Boyle, New experiments physico-mechanicall, touching the spring of the air and its effects, 1660
- [85] I.N. Levine, Physical Chemistry. University of Brooklyn. McGraw-Hill, 1978
- [86] S. Tamari, Meas. Sci. Technol., 15, 2004, 549–558
- [87] Image obtained from: <https://260h.pbworks.com/w/page/48383789/Intoxilyzer%20and%20IR%20Spectroscopy> - Accessed 23/06/14
- [88] C. Würth, M. Grabolle, J. Pauli, M. Spieles & U. Resch-Genger, Nature Protocols, 8, 2013, 1535–1550
- [89] Image obtained from: <https://weakinteractions.wordpress.com/primers/energy-levels/> - Accessed 23/04/16
- [91] Image obtained from: <https://principlequantumnumber.wordpress.com/> - Accessed 23/04/16
- [92] Image obtained from: <http://www.swxrflab.net/xrfinstrument.htm> - Accessed 23/04/16
- [93] Image obtained from: http://mag.ebmpapst.com/en/products/fans/fan-upgrade-diamond-light-source_8651/ - Accessed 24/04/16
- [94] © Michael Schmid

- [95] Image obtained from:
http://www.slri.or.th/th/index.php?option=com_content&view=article&id=1792&Itemid=332 -
 Accessed 25/05/16
- [96-97] © ISIS Neutron Source Facility
- [98] B.E. Warren, X-ray Diffraction. Addison Wesley., 1969
- [99] J.M. Cowley, Electron Diffraction Techniques Vol. 1. Oxford Science. 1992
- [100] T. Egami, S.J.L Billinge, Underneath the Bragg Peaks: Structural Analysis of Complex Material (2nd ed.). Elsevier. 2012
- [101] A. K. Soper, Gudrun and GudrunX, Programs for correcting raw neutron and x-ray diffraction data to differential scattering cross section, 2010
- [102] G. Placzek, Phys. Rev, 86, 1952, 377.
- [103] Image obtained from: <http://www.isis.stfc.ac.uk/instruments/gem/data-analysis/disordered-materials-data-analysis/setting-up-a-gudrun-file9489.html> - Accessed 12/12/16
- [104] A.K. Soper, Chem. Phys. 202, 1996, 295.
- [105] A.K. Soper, J. Mol. Liquids 78, 1998, 179.
- [106] J.D. Rodriguez-Blanco, S. Shaw, L.G. Benning, Mineralogical Magazine, 72, 2008, 1, 283–286
- [107] A. Lausi, E. Busetto, M. Leoni, P. Scardi, Synchrotron Radiation in Natural Science, 5, 2006, 100.
- [108] ICANS-XI International Collaboration on Advanced Neutron Sources, in: A.K. Soper, M. Misawa, et al., (Eds.), National Laboratory for High Energy Physics, KEK: KEK, Tsukuba, Japan, 1990, 809.
- [109] P. Zetterström, U. Dahlborg, R.G. Delaplane, W.S. Howells, Physica Scripta, 44, 1991, 56-62
- [110] K.M. Wetherall, PhD Thesis, University of Kent, 2009
- [111] B.M. Hasni, PhD Thesis, University of Kent, 2011
- [112] A.E. Van Driessche, L.G. Benning, J.D. Rodriguez-Blanco, M. Ossorio, P. Bots, J.M. García-Ruiz, Science, 336, 2012, 6077, 69-72.

